A single-point modeling approach for the intercomparison and evaluation of ozone dry deposition across chemical transport models (Activity 2 of AQMEII4)

Olivia E. Clifton[1], Donna Schwede[2], Christian Hogrefe[2], Jesse O. Bash[2], Sam Bland[3], Philip Cheung[4], Mhairi Coyle[5], Lisa Emberson[6], Johannes Flemming[7], Erick Fredj[8], Stefano Galmarini[9], Laurens Ganzeveld[10], Orestis Gazetas[9,11], Ignacio Goded[9], Christopher D. Holmes[12], László Horváth[13], Vincent Huijnen[14], Qian Li[15], Paul A. Makar[4], Ivan Mammarella[16], Giovanni Manca[9], J. William Munger[17], Juan L. Pérez-Camanyo[18], Jonathan Pleim[19], Limei Ran[20], Roberto San Jose[18], Sam J. Silva[21], Ralf Staebler[4], Shihan Sun[22], Amos P. K. Tai[22,23], Eran Tas[15], Timo Vesala[16,24], Tamás Weidinger[25], Zhiyong Wu[26], Leiming Zhang[4]

[1]NASA Goddard Institute for Space Studies, New York, NY, 10025 USA, and the Center for Climate Systems Research, Columbia Climate School, Columbia University in the City of New York, New York, NY 10025 USA
[2]United States Environmental Protection Agency, Office of Research and Development, Research Triangle Park, NC, 27711 USA
[3]Stockholm Environment Institute, Environment and Geography Department, University of York, York, YO10 5DD UK
[4]Air Quality Research Division, Atmospheric Science and Technology Directorate, Environment and Climate Change Canada, Toronto, M3H 5T4, Canada
[5]United Kingdom Centre for Ecology and Hydrology, Bush Estate, Penicuik, Midlothian, EH26 0QB UK, and The James Hutton Institute, Craigiebuckler, Aberdeen, AB15 8QH UK
[6]Environment and Geography Department, University of York, York, YO10 5DD UK
[7]European Centre for Medium-Range Weather Forecasts, Reading, RG2 9AX UK
[8]Department of Computer Science, The Jerusalem College of Technology, Jerusalem, Israel
[9] European Commission, Joint Research Centre (JRC), Ispra, Italy
[10]Wageningen University, Meteorology and Air Quality Section, Wageningen, the Netherlands
[11]Now at: Scottish Universities Environmental Research Centre (SUERC), East Kilbride G75 0QF, UK
[12]Earth, Ocean and Atmospheric Science, Florida State University, Tallahassee, FL, 32306 USA
[13]Department of Optics and Quantum Electronics, ELKH-SZTE Photoacoustic Research Group, University of Szeged, Szeged, Hungary
[14]Royal Netherlands Meteorological Institute, De Bilt, Netherlands
[15]The Institute of Environmental Sciences, The Robert H. Smith Faculty of Agriculture, Food and Environment, The Hebrew University of Jerusalem, Rehovot 76100, Israel
[16]Institute for Atmospheric and Earth System Research/Physics, University of Helsinki, Helsinki, Finland
[17]School of Engineering and Applied Sciences and Department of Earth and Planetary Sciences, Harvard University, Cambridge, MA, USA
[18]Computer Science School, Technical University of Madrid (UPM), Madrid, Spain
[19]Center for Environmental Measurement & Modeling, U.S. Environmental Protection Agency, Research Triangle Park, NC, USA
[20]Natural Resources Conservation Service, US Department of Agriculture, Greensboro, NC, USA
[21]Department of Earth Sciences, University of Southern California, Los Angeles, CA
[22]Earth and Environmental Sciences Programme, Faculty of Science, The Chinese University of Hong Kong, Hong Kong, China
[23]State Key Laboratory of Agrobiotechnology and Institute of Environment, Energy and Sustainability, The Chinese University of Hong Kong, Hong Kong, China
[24]Institute for Atmospheric and Earth System Research/Forest Sciences, University of Helsinki, Helsinki, Finland
[25]Department of Meteorology, Institute of Geography and Earth Sciences, Eötvös Loránd University, Pázmány Péter sétány 1/A, Budapest 1117, Hungary
[26]ORISE Fellow at Center for Environmental Measurement and Modeling, US Environmental Protection Agency, Research Triangle Park, NC, 27711 USA

Correspondence to: Olivia E. Clifton (olivia.e.clifton@nasa.gov)

Abstract. A primary sink of air pollutants and their precursors is dry deposition. Dry deposition estimates differ across chemical transport models, yet an understanding of the model spread is incomplete. Here we introduce Activity 2 of the Air Quality Model Evaluation International Initiative Phase 4 (AQMEII4). We examine eighteen dry deposition schemes from regional and global chemical transport models as well as standalone models used for impacts assessments or process understanding. We configure the schemes as single-point models at eight northern hemisphere locations with observed ozone fluxes. Single-point models are driven by a common set of site-specific meteorological and environmental conditions. Five of eight sites have at least three years and up to twelve years of ozone fluxes. The interquartile range across models in multiyear mean ozone deposition velocities ranges from a factor of 1.2 to 1.9 annually across sites and tends to be highest during winter compared to summer. No model is within 50% of observed multiyear averages across all sites and seasons, but some models perform well for some sites and seasons. For the first time, we demonstrate how contributions from depositional pathways vary across models. Models can disagree in relative contributions from the pathways, even when they predict similar deposition velocities, or agree in the relative contributions but predict different deposition velocities. Both stomatal and nonstomatal uptake contribute to the large model spread across sites. Our findings are the beginning of results from AQMEII4 Activity 2, which brings scientists who model air quality and dry deposition together with scientists who measure ozone fluxes to evaluate and improve dry deposition schemes in the chemical transport models used for research, planning, and regulatory purposes.

Short summary. A primary sink of air pollutants is dry deposition. Dry deposition estimates differ across models used to simulate atmospheric chemistry. Here we introduce an effort to examine dry deposition schemes from atmospheric chemistry models. We provide our approach's rationale, document the schemes, and describe datasets used to drive and evaluate the schemes. We also launch the analysis of results by evaluating the models against observations and identifying the processes leading to model-model differences.

1 Introduction

Dry deposition is a sink of many air pollutants and their precursors, removing compounds from the atmosphere after turbulence transports them to the surface and the compounds stick to or react with surfaces. Dry deposition may be a key influence on air pollution levels, including during high pollution episodes (Vautard et al., 2005; Solberg et al., 2008; Emberson et al., 2013; Huang et al., 2016; Anav et al., 2018; Baublitz et al., 2020; Clifton et al., 2020b; Lin et al., 2020; Gong et al., 2021). Dry deposition can also harm plants when gases diffuse through stomata (Krupa, 2003; Ainsworth et al., 2012; Lombardozzi et al., 2013; Grulke and Heath, 2019; Emberson, 2020). In particular, stomatal uptake of ozone adversely impacts crop yields (Mauzerall and Wang, 2001; McGrath et al., 2015; Guarin et al., 2019; Hong et al., 2020; U.S. EPA 2020a,b; Tai et al., 2021) and alters terrestrial carbon and water cycles (Ren et al., 2007; Sitch et al., 2007; Lombardozzi et al., 2015; Oliver et al., 2018).

Chemical transport models are key tools for research, planning, and regulatory purposes, including quantifying the influence of meteorology and emissions on air pollution. Accurate estimates of sinks like dry deposition are needed for source attribution, and simulated tropospheric and near surface abundances of air pollutants are highly sensitive to dry deposition (Wild, 2007; Tang et

al., 2011; Walker, 2014; Bela et al., 2015; Beddows et al., 2017; Hogrefe et al., 2018; Baublitz et al., 2020; Sharma et al., 2020; Ryan and Wild, 2021; Liu et al., 2022). However, chemical transport models do not always reproduce observed variability in dry deposition or in the near-surface abundances of air pollutants expected to be influenced strongly by dry deposition (Hardacre et al., 2015; Clifton et al., 2017; Kavassalis and Murphy, 2017; Silva and Heald, 2018; Travis and Jacob, 2019; Visser et al., 2021; Wong et al., 2022; Ye et al., 2022; Lam et al., 2022).

Previous work shows that dry deposition rates differ across chemical transport models (Dentener et al., 2006; Flechard et al., 2011; Hardacre et al., 2015; Li et al., 2016; Vivanco et al., 2018). Differences can stem from dry deposition scheme (Le Morvan-Quéméner et al., 2018; Wu et al., 2018; Wong et al., 2019; Otu-Larbi et al., 2021; Sun et al., 2022) as well as near-surface concentrations of the air pollutant and model-specific forcing related to meteorology and land use/land cover (LULC) (Hardacre et al., 2015; Tan et al., 2018, Zhao et al., 2018; Huang et al., 2022). Even with the same forcing, deposition velocities, or the strength of the dry deposition independent from near-surface concentrations, can vary by 2- to 3-fold across models (Flechard et al., 2011; Schwede et al., 2011; Wu et al., 2018; Wong et al., 2019; Cao et al., 2022; Sun et al., 2022), highlighting roles for process representation and parameter choice. Minimizing uncertainties in dry deposition schemes is not only important for the chemical transport models used for forecasting and regulatory applications, but also for improved understanding of long-term trends and variability in air pollution and impacts on humans, ecosystems, and resources, and building the related predictive ability in global Earth system and chemistry-climate models (Archibald et al., 2020; Clifton et al., 2020a).

In addition to occurring after diffusion through stomata, dry deposition occurs via nonstomatal pathways, including soil and leaf cuticles, as well as snow and water (Wesely and Hicks, 2000; Helmig et al., 2007; Fowler et al., 2009; Hardacre et al., 2015; Clifton et al., 2020a). For ozone, a recent review estimates that nonstomatal uptake is 45% on average of dry deposition over physiologically active vegetation (Clifton et al., 2020a). For highly soluble gases, nonstomatal uptake may dominate dry deposition (e.g., Karl et al., 2010; Nguyen et al., 2015; Clifton et al., 2022). Observations show strong unexpected spatiotemporal variations in nonstomatal uptake (Lenschow et al., 1981; Godowitch, 1990; Fuentes et al., 1992; Rondón et al., 1993; Coe et al., 1995; Mahrt et al., 1995; Fowler et al., 2001; Coyle et al., 2009; Helmig et al., 2009; Stella et al., 2011; Rannik et al., 2012; Potier et al., 2015; Wolfe et al., 2015; Fumagalli et al., 2016; Clifton et al., 2017; Clifton et al., 2019; Stella et al., 2019). In general, a dearth of common process-oriented diagnostics has prevented a clear picture of the stomatal versus nonstomatal deposition pathways driving differences in past model intercomparisons.

Measured turbulent fluxes are the best existing observational constraints on dry deposition but are limited in informing the relative roles of individual deposition pathways (Fares et al., 2018; Clifton et al., 2020a; He et al., 2021). While we can build mechanistic understanding of individual processes with laboratory and field chamber measurements (Fuentes and Gillespie, 1992; Cape et al., 2009; Fares et al., 2014; Fumagalli et al., 2016; Sun et al., 2016a,b; Potier et al., 2017; Finco et al., 2018), the dry deposition models that are used to scale processes to the ecosystem level, often the same models used in dry deposition schemes in chemical transport models, are highly empirical and poorly constrained. For example, a recent synthesis finds that while we have basic

Deleted: Dry

Deleted: process, parametric, and structural

Deleted: using

Deleted: dry deposition

Deleted: A

Deleted: ozone

Deleted: A

Deleted: 2017

Deleted: scale

knowledge of processes controlling ozone dry deposition, the relative importance of various processes remains uncertain and we lack ability to predict spatiotemporal changes well (Clifton et al., 2020a).

Launched in 2009, the Air Quality Model Evaluation International Initiative (AQMEII) has organized several activities (Rao et al., 2011). The fourth phase of AQMEII emphasizes process-oriented investigation of deposition in a common framework (Galmarini et al., 2021). AQMEII4 has two main activities. Activity 1 evaluates both wet and dry deposition across regional air quality models (Galmarini et al., 2021). Here we introduce Activity 2, which examines dry deposition schemes as standalone single-point models at eight sites with ozone flux observations. Importantly, single-point models are forced with the same, site-specific observational datasets of meteorology and ecosystem characteristics, and thus the intercomparison and evaluation can focus on deposition processes and parameters, as recommended by a recent review (Clifton et al., 2020a).

The four aims of Activity 2 are:
1. To quantify the performance of a variety of dry deposition schemes under identical conditions,
2. To understand how different deposition pathways contribute to the intermodel spread,
3. To probe the sensitivity of schemes to environmental factors, and variability in the sensitivities across schemes, and
4. To understand differences in dry deposition simulated in regional models in Activity 1.

Our effort builds on recent work using observation-driven single-point modeling of dry deposition schemes at Borden Forest (Wu et al., 2018), Ispra and Hyytiälä (Visser et al., 2021), and two sites in China (Cao et al., 2022), but is designed to test more sites and schemes as well as gain better understanding of intermodel differences. For example, sites examined represent a range of ecosystems in North America, Europe, and Israel, and single-point models are required to archive process-level diagnostics to facilitate understanding of simulated variations. Although our fourth aim is to contextualize differences among regional air quality models in Activity 1, we also include additional schemes in Activity 2 (e.g., from global chemical transport models and schemes that are used always as standalone models) to allow for a more comprehensive range of intermodel variation.

Below we describe the single-point modeling approach (Sect. 2) and fully document the individual single-point models using consistent language, units, and variable names (when appropriate) (Sect. 3). We also describe the northern hemisphere locations and site-specific meteorological and environmental datasets used to drive and evaluate the single-point models and the post-processing of observed and simulated values (Sect. 4). Our focus on ozone dry deposition reflects availability of long-term ozone flux measurements. In the results (Sect. 5), we present how models differ in capturing observed seasonality in ozone deposition velocities, including the contribution of different deposition pathways and how some environmental factors drive changes. We focus on multiyear averages and thus climatological evaluation but examine some aspects of interannual variability for sites with ozone flux records with three or more years. We then present a summary of our findings (Sect. 6). To our knowledge, this is the first model intercomparison demonstrating how the contribution of different pathways varies across dry deposition schemes and contributes to the model spread in ozone deposition velocities.

2 Single-point modeling approach

The single-point models used here are standalone dry deposition schemes driven by a consistent set of meteorological and environmental inputs from observations at sites with ozone fluxes. The single-point models were extracted from regional models used in AQMEII4 Activity 1 as well as other chemical transport models or have always been configured as single-point models. In general, dry deposition schemes vary in structure and level of detail in terms of the processes represented. Because there is limited documentation in the peer-reviewed literature of dry deposition schemes (especially as the schemes are configured in chemical transport models), and complete and consistent model descriptions aid our effort here, we fully describe the participating single-point models using consistent language, units, and variable names (when appropriate). Due to our focus on ozone, we limit our description to dry deposition of ozone. For brevity, we also limit our description to the implementation of the schemes in the single-point models at the eight sites examined, as opposed to how the schemes work as embedded within the chemical transport models (hereinafter, 'host models').

We note that surface- and soil-dependent variable choices (e.g., volumetric soil water content at wilting point) in the host model implementation of the schemes have likely been optimized for generalized LULC and soil classification schemes as well as environmental conditions and meteorology generated or used by the host model. Thus, our prescription of common site-specific variables across the single-point models in this study may create potential inconsistencies with the performance of the schemes inside host models. However, this separation and unification of variables that describe the surface and soil states is key for realistic estimates of the model spread due to structural uncertainty with respect to the processes and parameters directly related to dry deposition.

Table 1 gives measured and inferred variables used to force single-point models as well as other common variables used in the models. The meaning and units of variables listed in Table 1 are consistent throughout the manuscript. If a variable is not listed in Table 1 then that variable's meaning and units cannot be assumed to be consistent across models or the manuscript. The first time that we mention variables included in Table 1, we refer to Table 1.

The forcing variables provide inputs to drive models with detailed dependencies on biophysics, such as coupled photosynthesis-stomatal conductance models, as well as models that depend mainly on atmospheric conditions. Not every model uses every forcing variable. In general, input variables used by each single-point model should reflect the operation of the dry deposition scheme. For example, if the scheme in the host model ingests precipitation to calculate canopy wetness, rather than ingesting canopy wetness, then the single-point model should ingest precipitation to calculate canopy wetness.

We note that dry deposition schemes in many chemical transport models use methods derived from classic schemes like Wesely (1989). Implementations of classic schemes may deviate from original parameterization description papers in ways that can affect simulated rates (e.g., Hardacre et al., 2015) but may not be well documented. For example, there may be changes to LULC-specific parameters or the use of different LULC categories. In addition, implementations may tie processes to variables like leaf area index

Deleted: models

Deleted: Single

Deleted: ,

Deleted: are

Deleted: Dry

Deleted: schemes here.

Deleted: at larger scales

Deleted: parameter choices

Deleted: drivers

Deleted: drivers

Deleted: parameter choice and process representation

Deleted: or parameters

233   to capture seasonal changes rather than relying on season-specific parameters. To foster understanding of how adaptations from

234   original schemes influence simulated dry deposition rates, we encouraged participation in Activity 2 from models using schemes

235   based on classic parameterizations, in addition to models with different approaches.

236   **Table 1: Variables related to forcing datasets for single-point models.**

Variables in forcing data	Other common model variables
B parameter related to soil moisture [unitless]	D_{O_3} diffusivity of ozone in air [m^2 s^{-1}]
$[CO_2]$ ambient carbon dioxide mixing ratio [ppmv]	D_w diffusivity in air of water vapor [m^2 s^{-1}]
d displacement height [m]	D_{CO_2} diffusivity in air of carbon dioxide [m^2 s^{-1}]
f_{wet} fraction of the canopy that is wet [fractional]	e_{sat} saturation vapor pressure [Pa]
G incoming shortwave radiation [W m^{-2}]	f_0 reactivity factor for ozone [unitless]
h canopy height [m]	H Henry's Law constant [M atm^{-1}]
LAI leaf area index [m^2 m^{-2}]	κ thermal diffusivity of air [m^2 s^{-1}]
$[O_3]$ ambient ozone mixing ratio [ppbv]	L Obukhov length [m]
P precipitation rate [mm hr^{-1}]	M_{air} molar mass of air [g mol^{-1}]
p_a air pressure [Pa]	Pr Prandtl number [unitless]
PAR photosynthetically active radiation [μmol m^{-2} s^{-1}]	ρ air density [kg m^{-3}]
RH relative humidity [fractional]	Sc Schmidt number [unitless]
SD snow depth [cm]	v_d ozone deposition velocity [m s^{-1}]
SH sensible heat flux [W m^{-2}]	VPD vapor pressure deficit [kPa]
T_a air temperature [ºC]	ψ_{leaf} leaf water potential [MPa]
T_g ground temperature near surface [ºC]	ψ_{soil} soil matric potential [kPa]
u wind speed [m s^{-1}]	
u^* friction velocity [m s^{-1}]	
w_g volumetric soil water content near surface [m^3 m^{-3}]	
w_2 volumetric soil water content at root zone [m^3 m^{-3}]	
w_{fc} volumetric soil water content at field capacity [m^3 m^{-3}]	
w_{sat} volumetric soil water content at saturation [m^3 m^{-3}]	
w_{wlt} volumetric soil water content at wilting point [m^3 m^{-3}]	
z_0 roughness length [m]	
z_r reference height [m]	
θ solar zenith angle [º]	

237

238   Like many model intercomparisons, our effort is an 'ensemble of opportunity' (e.g., Galmarini et al., 2004; Tebaldi and Knutti,

239   2007; Potempski and Galmarini, 2009; Solazzo and Galmarini, 2014; Young et al., 2018) and may underestimate structural

240   uncertainty due to process and parameter differences across models. Nonetheless, the design of our effort, with emphasis on

241   processes, parameters, and sensitivities, is designed to explore uncertainty more systematically than past attempts.

242

243   The first set of Activity 2 simulations is driven by inputs from observations, and those simulations are examined here. Future work

244   will examine sensitivity tests in which dry deposition is calculated with perturbed values of input variables (e.g., air temperature,

245   leaf area index). We will also design tests that isolate the influence of input parameters (e.g., initial resistance to stomatal uptake,

246   field capacity of soil).

247

Formatted: Justified

Deleted: r_0 roughness length [m]¶

Formatted: Justified

Deleted: Potempsky

Deleted: , structural,

Deleted: parametric

Diagnostic outputs required from single-point models follow the requirements of Activity 1 (see Table 4 in Galmarini et al. (2021)). Among required outputs are effective conductances (Paulot et al., 2018; Clifton et al., 2020b) for dry deposition to plant stomata, leaf cuticles, the lower canopy, and soil. (Note that not all single-point models simulate deposition to the lower canopy). As explained and defined in Galmarini et al. (2021), an effective conductance [m s^{-1}] represents the portion of v_d that occurs via a single pathway. An effective conductance is distinct from an absolute conductance, which represents an individual process. (Note that a conductance is the inverse of a resistance). The sum of the effective conductances across all pathways represented is v_d. In contrast, calculating v_d with absolute conductances requires considering the resistance framework. Archiving effective conductances facilitates comparison of the contribution of each pathway across dry deposition schemes with varying resistance frameworks and differing resistances to transport. Previous model comparisons examine absolute conductances and suggest that differences in pathways or processes lead to differences in v_d (Wu et al., 2018; Huang et al., 2022). Our approach with effective conductances offers a more apples-to-apples comparison across models, allowing us to definitively say whether a given pathway leads to intermodel differences in v_d.

3 Documentation of single-point models

The classic big-leaf resistance network for ozone deposition velocity (v_d) [m s^{-1}] (Table 1) is based on three resistances, which are added in series, following:

$$v_d = (r_a + r_b + r_c)^{-1} \quad (1)$$

The variable r_a is aerodynamic resistance; r_b is quasi-laminar boundary layer resistance around the bulk surface; r_c is surface resistance. Throughout the manuscript, all resistances (denoted by r) are in units of s m^{-1}. The single-point models examined here employ Eq. (1), with two exceptions. The exceptions are MLC-CHEM, which is a multilayer canopy model that simulates the ozone concentration gradient within the canopy, and CMAQ STAGE, which uses surface-specific quasi-laminar resistances. In this section, we describe methods for r_a and r_b across models (Tables S1, S2, S3), and ozone-specific dry deposition parameters (Table S4). Equations for r_c (and the v_d equation for CMAQ STAGE, which deviates from Eq. (1)) are in the individual model subsections below. In the model subsection for MLC-CHEM, we describe how the model diagnoses v_d from the canopy-top ozone flux and the resistances associated with dry deposition.

With one exception (CMAQ STAGE), the single-point models use r_a equations based on Monin-Obukhov Similarity Theory (Table S1). However, the exact forms of the Monin-Obukhov Similarity Theory equations vary across the models.

Obukhov length (L) [m] (Table 1) is often used in r_a equations but is not observed. Most model L equations are similar, apart from whether models use virtual or ambient temperature and whether they include bounds on L (and what the bounds are) (Table S2).

Models are configured to accept inputs and return predicted values at the specified ozone flux measurement height at the given site (i.e., reference height z_r [m] (Table 1)). Roughness length (z_0) [m] (Table 1) and displacement height (d) [m] (Table 1) are also

often used in r_a equations yet are not observed and are especially important in estimating fluxes at z_r rather than the lowest atmospheric level of the host model. We supply estimates of z_0 and d for the models that employ them. Estimates follow Meyers et al. (1998):

$$z_0 = h\left(0.23 - \frac{LAI^{0.25}}{10} - \frac{a-1}{10}\right) \quad (2)$$

$$d = h\left(0.05 + \frac{LAI^{0.2}}{2} + \frac{a-1}{20}\right) \quad (3)$$

The variable h [m] is canopy height (Table 1); LAI [m^2 m^{-2}] is leaf area index (Table 1); a [unitless] is a parameter based on LULC. Meyers et al. (1998) suggest a correction for z_0 if LAI is less than 1 but we do not employ this correction given that it creates discontinuities in the time series.

Table S3 provides the quasi-laminar boundary layer resistance equations. Most models treat this resistance for the bulk surface (i.e., r_b in Eq. (1)), and most use r_b from Wesely and Hicks (1977). A key part of r_b parameterizations is the ratio scaling the quasi-laminar boundary layer resistance for heat to ozone ($R_{diff,b}$) (Table S4). Fundamentally, $R_{diff,b} = Sc/Pr$, where Sc [unitless] is the Schmidt number (Table 1) and Pr [unitless] is the Prandtl number (Table 1). All but one employ $R_{diff,b} = Sc/Pr = \kappa/D_{O_3}$ where κ [m^2 s^{-1}] is thermal diffusivity of air (Table 1), and D_{O_3} [m^2 s^{-1}] is ozone diffusivity in air (Table 1); however, values of κ and D_{O_3} vary across models (Table S4).

Table S4 presents model prescriptions for ozone-specific dry deposition parameters: the ratio that scales stomatal resistance from water vapor to ozone ($R_{diff,st}$), reactivity factor for ozone (f_0) [unitless] (Table 1), and Henry's Law constant for ozone (H) [M atm^{-1}] (Table 1). Where used, values of f_0 and H are very similar across models. Some models employ temperature dependencies on H. Notably, values of $R_{diff,st}$ vary from 1.2 to 1.7 across models. (The current estimate of this ratio is 1.51 (Massman, 1998)). GEM-MACH Zhang and models based on GEOS-Chem are the models that prescribe lower $R_{diff,st}$ values.

3.1 WRF-Chem Wesely

WRF-Chem uses a scheme based on Wesely (1989). Parameters in Table S5 are site- and season-specific. WRF-Chem has two seasons: midsummer with lush vegetation [day of year between 90 and 270] and autumn with unharvested croplands [day of year less than 90 or greater than 270].

3.1.1 Surface resistance

Surface resistance (r_c) follows:

$$r_c = \left(\frac{1}{r_{st} + r_m} + \frac{1}{r_{cut}} + \frac{1}{r_{dc} + r_{cl} + r_T} + \frac{1}{r_{ac} + r_g + r_T}\right)^{-1} \quad (4)$$

To consider effects of T_a, resistance r_T (Walmsley and Wesely, 1996) follows:

$$r_T = 1000\, e^{-T_a - 4} \quad (5)$$

In addition to the use of r_T in Eq. (4), r_T is used in the equation for cuticular resistance below.

3.1.2 Stomatal and mesophyll resistances

Stomatal resistance (r_{st}) follows:

$$r_{st} = R_{diff,st}\,\frac{r_i}{f(T_a)\,f(G)} \quad (6)$$

$r_{st} = R_{diff,st}\,\frac{r_i}{f(T_a)\,f(G)}$ The parameter r_i is initial resistance for stomatal uptake (Table S5).

Effects of air temperature (T_a) [°C] (Table 1) follow:

$$f(T_a) = T_a\,\frac{(40 - T_a)}{400} \quad (7)$$

Effects of incoming shortwave radiation (G) [W m⁻²] (Table 1) follow:

$$f(G) = \left(1 + \left(\frac{200}{G + 0.1}\right)^2\right)^{-1} \quad (8)$$

Mesophyll resistance (r_m) follows:

$$r_m = \left(\frac{H}{3000} + 100\,f_0\right)^{-1} \quad (9)$$

3.1.3 Cuticular resistance

Cuticular resistance (r_{cut}) follows:

$$r_{cut} = \begin{cases} \dfrac{r_{lu} + r_T}{\frac{H}{10^5} + f_0}, & RH \le 0.95 \text{ and } P = 0 \\[2ex] \left(\dfrac{1}{W} + \dfrac{3}{r_{lu} + r_T}\right)^{-1}, & RH > 0.95 \text{ or } P > 0 \end{cases} \quad (10)$$

The parameter r_{lu} is initial resistance for cuticular uptake (Table S5); RH is relative humidity [fractional] (Table 1); P is precipitation rate [mm hr⁻¹] (Table 1). The parameter W is used to account for leaf wetness, and follows:

$$W = \begin{cases} 3000, P = 0 \\ 1000, P > 0 \end{cases} \quad (11)$$

3.1.4 Resistances to the lower canopy and ground (and associated resistances to transport)

The resistance associated with within-canopy convection (r_{dc}) follows:

$$r_{dc} = 100 \left(1 + \frac{1000}{G}\right) \quad (12)$$

Resistances to the lower canopy (r_{cl}), in-canopy turbulence (r_{ac}), and the ground (r_g) are prescribed (Table S5). $r_T = 1000\,e^{-T_a - 4}$

3.2 GEOS-Chem Wesely

GEOS-Chem is based on Wesely (1989). Wang et al. (1998) describe the initial implementation. We examine the scheme from GEOS-Chem v13.3. Parameters in Table S6 are site-specific. If there is snow, then surface resistance (r_c) is calculated with the snow parameters in Table S6.

3.2.1 Surface resistance

Surface resistance (r_c) follows:

$$r_c = \left(\frac{1}{r_{st} + r_m} + \frac{1}{r_{cut}} + \frac{1}{r_{dc} + r_{cl}} + \frac{1}{r_{ac} + r_g}\right)^{-1} \quad (13)$$

440 To consider effects of T_a, resistance r_T follows:

441 $$r_T = 1000\, e^{-T_a-4} \quad (14)$$

442 The variable r_T is used in the below equations for the resistances to cuticular, lower canopy, and the ground.

443 ### 3.2.2 Stomatal and mesophyll resistances

444 Stomatal resistance (r_{st}) follows:

445 $$r_{st} = R_{diff,st}\, \frac{r_i}{LAI_{eff}\, f(T_a)} \quad (15)$$

446 The parameter r_i is initial resistance to stomatal uptake (Table S6); LAI_{eff} [m^2 m^{-2}] is effective LAI, which is the surface area of

447 actively transpiring leaves per ground surface area. The variable LAI_{eff} is calculated using function of LAI, solar zenith angle (θ)

448 [°] (Table 1), and cloud fraction using a parameterization developed by Wang et al. (1998). In GEOS-Chem, if G is zero then

449 LAI_{eff} equals 0.01. For the single-point model, we set G to be zero when θ is greater than 95° so that nighttime r_{st} values in the

450 single-point model are more similar to GEOS-Chem. GEOS-Chem almost never has non-zero G at night but measured values are

451 frequently small and non-zero. Here cloud fraction is assumed to be zero.

452 Effects of T_a follows:

453 $$f(T_a) = \begin{cases} 0.01, & T_a \leq 0 \\ T_a \frac{(40-T_a)}{400}, & 0 < T_a < 40 \\ 0.01, & 40 \leq T_a \end{cases} \quad (16)$$

454 Mesophyll resistance (r_m) follows:

455 $$r_m = \left(\frac{H}{3000} + 100\, f_0 \right)^{-1} \quad (17)$$

456 ### 3.2.3 Cuticular resistance

457 Cuticular resistance (r_{cut}) follows:

458 $$r_{cut} = \begin{cases} \frac{r_{lu} + \min\{r_T, r_{lu}\}}{LAI} \left(\frac{H}{10^5} + f_0 \right)^{-1}, & \frac{r_{lu} + \min\{r_T, r_{lu}\}}{LAI} < 9999 \\ 10^{12}, & \frac{r_{lu} + \min\{r_T, r_{lu}\}}{LAI} \geq 9999 \end{cases} \quad (18)$$

459 The parameter r_{lu} is initial resistance for cuticular uptake (Table S6).

460 ### 3.2.4 Resistances to the lower canopy and ground (and associated resistances to transport)

461 $r_T = 1000\, e^{-T_a-4}$ The resistance associated with in-canopy convection (r_{dc}) follows:

462 $$r_{dc} = 100 \left(1 + \frac{1000}{G + 10} \right) \quad (19)$$

463 The resistance to surfaces in the lower canopy (r_{cl}) follows:

464 $$r_{cl} = \left(\frac{H}{10^5 \left(r_{cl,S} + \min\{r_T, r_{cl,S}\} \right)} + \frac{f_0}{r_{cl,O} + \min\{r_T, r_{cl,O}\}} \right)^{-1} \quad (20)$$

465 Parameters $r_{cl,S}$ and $r_{cl,O}$ are initial resistances to the lower canopy (Table S6).

466 The resistance to turbulent transport to the ground (r_{ac}) is constant (Table S6).

476 Resistance to the ground (r_g) follows:

477 $$r_g = \left(\frac{H}{10^5 \left(r_{g,S} + \min\{r_T, r_{g,S}\} \right)} + \frac{f_0}{r_{g,o} + \min\{r_T, r_{g,O}\}} \right)^{-1} \quad (21)$$

478 Parameters $r_{g,S}$ and $r_{g,o}$ are initial resistances to uptake on the ground (Table S6).

3.3 IFS

480 ECMWF IFS uses two schemes based on Wesely (1989): Meteo-France's SUMO (Michou et al., 2004) ("IFS SUMO Wesely")

481 and GEOS-Chem 12.7.2 ("IFS GEOS-Chem Wesely"). Unless stated otherwise, the components are the same between schemes.

482 IFS SUMO Wesely parameters in Table S7 are site- and season-specific. Seasons are defined as: 'transitional spring' [March,

483 April, May], 'mid-summer' [June, July, August], 'autumn' [September, October, November] and 'late autumn' [December,

484 January, February]. Otherwise, if there is snow then the model employs the 'winter, snow' parameter values. IFS GEOS-Chem

485 Wesely parameters in Table S8 are site-specific. If there is snow, then the model employs the snow type. For snow type, only the

486 resistance to surfaces in the lower canopy (r_{cl}) is defined [1000 s m^{-1}].

3.3.1 Surface resistance

488 Surface resistance (r_c) follows:

489 $$r_c = \left(\frac{1}{r_{st} + r_m} + \frac{1}{r_{cut}} + \frac{1}{r_{dc} + r_{cl}} + \frac{1}{r_{ac} + r_g + r_T} \right)^{-1} \quad (22)$$

490 $$r_m = \left(\frac{H}{3000} + 100 f_0 \right)^{-1} \quad r_{dc} = 100 \left(1 + \frac{1000}{G} \right)$$ To consider effects of T_a, resistance r_T follows:

491 $$r_T = 1000 \, e^{-T_a - 4} \quad (23)$$

492 In addition to the use of r_T in Eq. (22), r_T is included in cuticular resistance equations below.

3.3.2 Stomatal and mesophyll resistances

494 For IFS SUMO Wesely, stomatal resistance (r_{st}) follows:

495 $$r_{st} = R_{diff,st} \frac{r_i}{LAI \, f(G) \, f(VPD) \, f(w_2)} \quad (24)$$

496 The parameter r_i is initial resistance to stomatal uptake (Table S7).

497 Effects of G follow:

498 $$f(G) = \min \left\{ \frac{0.004 \, G + 0.5}{0.81 \, (0.004 \, G + 1)}, 1 \right\} \quad (25)$$

499 Effects of vapor pressure deficit (VPD) [kPa] (Table 1) follow:

500 $$f(VPD) = \begin{cases} e^{0.3 \, VPD}, \, forests \\ 1, \, otherwise \end{cases} \quad (26)$$

501 Effects of root-zone soil water content (w_2) [m^3 m^{-3}] (Table 1) follow:

502 $$f(w_2) = \begin{cases} 0, \, w_2 < w_{wlt} \\ \frac{w_2 - w_{wlt}}{w_{fc} - w_{wlt}}, \, w_{wlt} < w_2 < w_{fc} \\ 1, \, w_2 > w_{fc} \end{cases} \quad (27)$$

534    $(r_{lu} + r_T)\left(\dfrac{H}{10^5} + f_0\right)^{-1}$ The parameter w_{wlt} is the soil water content at wilting point [m³ m⁻³] (Table 1); w_{fc} is the soil water

535   content at field capacity [m³ m⁻³] (Table 1).

537 For IFS GEOS-Chem Wesely, stomatal resistance (r_{st}) follows:

538 $$r_{st} = R_{diff,st}\, \frac{r_i}{LAI_{eff}\, f(T_a)} \quad (28)$$

539 The parameter r_i is initial resistance to stomatal uptake (Table S8); LAI_{eff} [m² m⁻²] is effective LAI, which is the surface area of

540 actively transpiring leaves per ground surface area of actively transpiring leaves. The variable LAI_{eff} is calculated as a function of

541 LAI, θ, and cloud fraction using a parameterization developed by Wang et al. (1998). In GEOS-Chem, if G is zero then LAI_{eff} is

542 equal to 0.01. For the single-point model, we set G to be zero when θ is greater than 95°. GEOS-Chem almost never has non-zero

543 G at night but measured values are frequently small and non-zero. This change makes nighttime r_{st} values in the single-point model

544 more similar GEOS-Chem. Here cloud fraction is assumed to be zero.

545 Effects of T_a follow:

546 $$f(T_a) = T_a\, \frac{40 - T_a}{400} \quad (29)$$

548 For both configurations, mesophyll resistance (r_m) follows:

549 $$r_m = \left(\frac{H}{3000} + 100\, f_0\right)^{-1} \quad (30)$$

550 **3.3.3 Cuticular resistance**

551 For IFS SUMO Wesely,

552 $$r_{cut} = (r_{lu} + r_T)\left(\frac{H}{10^5} + f_0\right)^{-1} \quad (31)$$

553 The parameter r_{lu} is initial resistance for cuticular uptake (Table S7).

555 For IFS GEOS-Chem Wesely,

556 $$r_{cut} = \frac{(r_{lu} + r_T)}{LAI}\left(\frac{H}{10^5} + f_0\right)^{-1} \quad (32)$$

557 The parameter r_{lu} is initial resistance to cuticular uptake (Table S8).

558 **3.3.4 Resistances to the lower canopy and ground (and associated resistances to transport)**

559 The resistance associated with in-canopy convection (r_{dc}) follows:

560 $$r_{dc} = 100\left(1 + \frac{1000}{G}\right) \quad (33)$$

561 Resistances to surfaces in the lower canopy (r_{cl}), in-canopy turbulence (r_{ac}), and ground (r_g) are prescribed (Tables S7 and S8).

3.4 GEM-MACH Wesely

Operationally, GEM-MACH uses a dry deposition scheme based on Wesely (1989) (Makar et al., 2018). Parameters defined in Table S9 are site- and sometimes season-specific. Table S10 describes how seasons are distributed as a function of month and latitude.

3.4.1 Surface resistance

Surface resistance (r_c) follows:

$$r_c = \left(\frac{1-W}{r_{st}+r_m} + \frac{1}{r_{cut}} + \frac{1}{r_{dc}+r_{cl}} + \frac{1}{r_{ac}+r_g} \right)^{-1} \quad (34)$$

The parameter W [fractional] is used to account for leaf wetness, following:

$$W = \begin{cases} 0.5, P > 1 \; mm \; hr^{-1} \; or \; RH > 0.95 \\ 0, otherwise \end{cases} \quad (35)$$

3.4.2 Stomatal resistance and mesophyll resistance

Stomatal resistance (r_{st}) is based on Jarvis (1976), Zhang et al. (2002a, 2003) and Baldocchi et al. (1987):

$$r_{st} = R_{diff,st} \frac{r_i}{LAI \max\{f(G) \, f(VPD) \, f(T_a) \, f(c_a), \; 0.0001\}} \quad (36)$$

The parameter r_i is initial resistance to stomatal uptake (Table S9).

Curve-fitting of data from Jarvis (1976) and Ellsworth and Reich (1993) was used to infer the following:

$$f(G) = \max\{0.206 \ln(G) - 0.605, 0\} \quad (37)$$

Effects of VPD follow:

$$f(VPD) = \max\left\{0.0, \max\left\{1.0, \left(1.0 - 0.03 \left(1 - RH\right) 10^{\frac{0.7859 + 0.03477 \, T_a}{1 + 0.00412 \, T_a}}\right)\right\}\right\} \quad (38)$$

Effects of T_a follow:

$$f(T_a) = \left(\frac{(T_a - T_{min})(T_{max} - T_a)}{(T_{opt} - T_{min})(T_{max} - T_{opt})} \right)^{0.62} \quad (39)$$

Parameters T_{min}, T_{max}, and T_{opt} [ºC] are minimum, maximum, and optimum temperature, respectively (Table S9).

Effects of ambient carbon dioxide mixing ratio ($[CO_2]$) [ppmv] (Table 1) follow:

$$f(c_a) = \begin{cases} 1, \; [CO_2] \leq 100 \\ 1 - \left(7.35 \; x \; 10^{-4} \; \ln(\ln(G)) - 8.75 \; x \; 10^{-4}\right) [CO_2], \; 100 < [CO_2] < 1000 \\ 0, \; [CO_2] \geq 1000 \end{cases} \quad (40)$$

Mesophyll resistance (r_m) follows:

$$r_m = \left(LAI \left(\frac{H}{3000} + 100 \, f_0 \right) \right)^{-1} \quad (41)$$

3.4.3 Cuticular resistance

Cuticular resistance (r_{cut}) follows:

$$r_{cut} = \frac{r_{lu}}{LAI} \left(\frac{H}{10^5} + f_0 \right)^{-1} \quad (42)$$

616   The parameter r_{lu} is initial resistance to cuticular uptake (Table S9).

3.4.4 Resistances to the lower canopy and ground (and associated resistances to transport)

618   The resistance associated with in-canopy convection (r_{dc}) follows:

619    $$r_{dc} = 100 + \left(1 + \frac{1000}{G + 10}\right) \quad (43)$$

620   The resistance posed by uptake to the lower canopy (r_{cl}) follows:

621    $$r_{cl} = \left(\frac{H}{10^5 \, r_{cl,S}} + \frac{f_0}{r_{cl,O}}\right)^{-1} \quad (44)$$

622   Parameters $r_{cl,S}$ and $r_{cl,O}$ are initial resistances to uptake by surfaces in the lower canopy (Table S9).

623   The parameter r_{ac} is resistance to in-canopy turbulence and r_g is resistance to the ground; both are prescribed (Table S9).

3.5 GEM-MACH Zhang

625   GEM-MACH also has an implementation of Zhang et al. (2002b). Parameters in Table S11 are site-specific.

3.5.1 Surface resistance

627   Surface resistance (r_c) follows:

628    $$r_c = \min\left\{10, \left(\frac{1 - W}{r_{st}} + \frac{1}{r_{cut}} + \frac{1}{r_{ac} + r_g}\right)^{-1}\right\} \quad (45)$$

629   The variable W [fractional] is used to account for leaf wetness, following:

630    $$W = \begin{cases} \min\left\{0.5, \frac{G - 200}{800}\right\}, & \text{precipitation or dew}, \; T_a > 1, \; G > 200 \\ 0, & \text{otherwise} \end{cases} \quad (46)$$

631   Precipitation is assumed to occur if P is greater than 0.20 mm hr^{-1}. Dew is assumed to occur if P is less than 0.20 mm hr^{-1} and

632    $$u^* < c_{dew} \frac{1.5}{\max\left\{1 \times 10^{-4}, \frac{0.622 \, e_{sat} \, (1 - RH)}{p_a}\right\}} \quad (47)$$

633   The variable e_{sat} [Pa] is saturation vapor pressure (Table 1); p_a [Pa] is air pressure (Table 1); c_{dew} is the dew coefficient [0.3].

3.5.2 Stomatal resistance

635   Stomatal resistance (r_{st}) follows:

636    $$r_{st} = R_{diff,st} \frac{r_i(LAI, PAR)}{f(T_a) f(VPD) f(\psi_{leaf})} \quad (48)$$

637   The variable $r_i(LAI, PAR)$ is initial resistance to stomatal uptake that varies with LAI and PAR, based on Norman (1982) and

638   Zhang et al. (2001):

639    $$r_i(LAI, PAR) = \left(\frac{LAI_{sun}}{r_i\left(1 + \frac{b_{rs}}{PAR_{sun}}\right)} + \frac{LAI_{shd}}{r_i\left(1 + \frac{b_{rs}}{PAR_{shd}}\right)}\right)^{-1} \quad (49)$$

640   The parameter r_i is initial resistance to stomatal uptake (Table S11); b_{rs} [W m^{-2}] is empirical (Table S11); LAI_{sun} and LAI_{shd} [m^2

641   m^{-2}] are sunlit and shaded LAI:

660    $LAI_{sun} = \frac{1-e^{-K_b\,LAI}}{K_b}$ (50)

661    $LAI_{shd} = LAI - LAI_{sun}$ (51)

662   The variable K_b is canopy light extinction coefficient [unitless]:

663    $K_b = \frac{0.5}{\cos\left(\frac{\pi}{180}\theta\right)}$ (52)

664   Variables PAR_{sun} and PAR_{shd} [W m^{-2}] are photosynthetically active radiation reaching sunlit and shaded leaves:

665    $PAR_{shd} = PAR_{diff}\, e^{-0.5\,LAI^a} + 0.07\, PAR_{dir}\,(1 - 0.1\,LAI)e^{-\cos\left(\frac{\pi}{180}\theta\right)}$ (53)

666    $PAR_{sun} = PAR_{shd} + \frac{0.5\,PAR_{dir}^b}{\cos\left(\frac{\pi}{180}\theta\right)}$ (54)

667   If LAI is greater than 2.5 m^2 m^{-2} and G is less than 200 W m^{-2}, then empirical parameters a equals 0.8 and b equals 0.8. Otherwise,

668   a equals 0.07 and b equals 1. Calculation of direct and diffuse components of PAR (PAR_{dir} and PAR_{diff}) has been updated from

669   Zhang et al. (2001) to follow Iqbal (1983):

670    $PAR_{dir} = G\,FRAD_V\,FD_V$ (55)

671    $PAR_{diff} = G\,FRAD_V\,(1 - FD_V)$ (56)

672   The variable $FRAD_v$ follows:

673    $FRAD_V = \frac{R_V}{R_V + R_N}$ (57)

674   Variables R_v and R_N follow:

675    $R_N = RD_M + RD_N$ (58)

676    $R_V = RD_U + RD_V$ (59)

677   The variable RD_U follows:

678    $RD_U = 600 \cos\left(\frac{\pi}{180}\theta\right) e^{\frac{-0.185\,p_a}{p_{std}\cos\left(\frac{\pi}{180}\theta\right)}}$ (60)

679   The variable p_{std} is standard air pressure [1.0132 x 10^5 Pa].

680   The variable RD_V follows:

681    $RD_V = 0.42\,(600 - RD_U)\cos\left(\frac{\pi}{180}\theta\right)$ (61)

682   The variable RD_M follows:

683    $RD_M = \cos\left(\frac{\pi}{180}\theta\right)\left(720\, e^{\left(-\frac{0.06\,p_a}{p_{std}\cos\left(\frac{\pi}{180}\theta\right)}\right)} - \left(1320 * 0.077\left(\frac{2\,p_a}{p_{std}\cos\left(\frac{\pi}{180}\theta\right)}\right)^{0.3}\right)\right)$ (62)

684   The variable RD_N follows:

685    $RD_N = 0.65 \cos\left(\frac{\pi}{180}\theta\right)\left(720 - RD_M - \left(1320 * 0.077\left(\frac{2\,p_a}{p_{std}\cos\left(\frac{\pi}{180}\theta\right)}\right)^{0.3}\right)\right)$ (63)

686   The variable FD_v follows:

701
$$FD_V = \begin{cases} 0.941124\,RD_U/R_V, & \frac{G}{R_V+R_N} \geq 0.89 \\ \left(1 - \left(\frac{\left(0.9 - \frac{G}{R_V+R_N}\right)}{0.7}\right)^{\frac{2}{3}}\right)RD_U/R_V, & 0.21 \geq \frac{G}{R_V+R_N} < 0.89 \\ 0.00955\,RD_U/R_V, & \frac{G}{R_V+R_N} < 0.21 \end{cases} \quad (64)$$

702 Effects of T_a follow:

703
$$f(T_a) = \left(\frac{T_a - T_{min}}{T_{opt} - T_{min}}\right)\left(\frac{T_{max} - T_a}{T_{max} - T_{opt}}\right)^{\frac{T_{max} - T_{opt}}{T_{max} - T_{min}}} \quad (65)$$

704 Parameters T_{min}, T_{max}, and T_{opt} [ºC] are minimum, maximum, and optimum temperature, respectively (Table S11).

705 Effects of VPD follow:

706
$$f(VPD) = \min\{\max\{1 - b_{vpd}\,VPD, 0\}, 1\} \quad (66)$$

707 The parameter b_{vpd} [kPa^{-1}] is empirical (Table S11).

708 Effects of leaf water potential (ψ_{leaf}) [MPa] (Table 1) follow:

709
$$f(\psi_{leaf}) = \min\left\{\max\left\{\frac{\psi_{leaf} - \psi_{leaf,2}}{\psi_{leaf,1} - \psi_{leaf,2}}, 0\right\}, 1\right\} \quad (67)$$

710 The variable ψ_{leaf} is approximated as:

711
$$\psi_{leaf} = -0.72 - 0.0013\,G \quad (68)$$

712 Parameters $\psi_{leaf,1}$ and $\psi_{leaf,1}$ [MPa] are empirical (Table S11).

713 **3.5.3 Cuticular resistance**

714 Cuticular resistance (r_{cut}) follows:

715
$$r_{cut} = \begin{cases} \max\left\{100, \frac{c_{cut,dry}}{u^*\,LAI^{0.25}\,e^{3\,RH}}\right\}, & T_a \geq -1, \text{neither precipitation nor dew} \\ \frac{c_{cut,wet}}{u^*\sqrt{LAI}}, & T_a \geq -1, \text{precipitation or dew occurring} \\ \max\left\{100, \frac{c_{cut,dry}}{u^*\,LAI^{0.25}\,e^{3\,RH}}\,\min\{2, e^{0.2\,(-1-T_a)}\}\right\}, & T_a < -1 \end{cases} \quad (69)$$

716 The variable u^* [m s^{-1}] is friction velocity (Table 1); $c_{cut,dry}$ [unitless] is a coefficient related to dry cuticular uptake (Table S11).

717 If the fraction of snow coverage (f_{snow}) is greater than 10^{-4} then a correction is applied:

718
$$r_{cut} = \left(\frac{1 - f_{snow}}{r_{cut}} + \frac{f_{snow}}{2000}\right)^{-1} \quad (70)$$

719 If LAI is less than 2 x 10^{-6} m^2 m^{-2} then r_{cut} is very large.

720

721 The fraction of snow coverage (f_{snow}) follows:

722
$$f_{snow} = \min\left\{1, \frac{SD}{SD_{max}}\right\} \quad (71)$$

723 The variable SD [cm] is snow depth (Table 1); SD_{max} [cm] is maximum snow depth (Table S11).

3.5.4 Resistance to the ground (and associated resistance to transport)

The resistance to in-canopy turbulence (r_{ac}) follows:

$$r_{ac} = r_{ac0} \frac{LAI^{0.25}}{(u^*)^2} \quad (72)$$

The variable r_{ac0} follows:

$$r_{ac0} = r_{ac0,min} + \frac{LAI - LAI_{min}}{LAI_{max} - LAI_{min}} (r_{ac0,max} - r_{ac0,min}) \quad (73)$$

$r_{ac} = r_{ac0} \frac{LAI^{0.25}}{(u^*)^2} r_{ac0} = r_{ac0,min} + \frac{LAI - LAI_{min}}{LAI_{max} - LAI_{min}} (r_{ac0,max} - r_{ac0,min})$ Parameters LAI_{min} and LAI_{max} [m^2 m^{-2}] are minimum and maximum LAI across the site's observational record; $r_{ac0,min}$ and $r_{ac0,max}$ are initial resistances (Table S11).

Ground resistance (r_g) is prescribed but modified under certain conditions. If T_s is less than -1ºC then:

$$r_g = r_g \min\{2, e^{-0.2\,(T_s+1)}\} \quad (74)$$

The near-surface air temperature (T_s) is approximated from a linear interpolation between T_a and T_g to a height of 1.5 m.

If f_{snow} (see Eq. (71)) is greater than or equal to 10^{-4} then:

$$r_g = \left(\frac{1 - \min\{1,\ 2f_{snow}\}}{r_g} + \frac{\min\{1,\ 2f_{snow}\}}{2000}\right)^{-1} (f_{snow} = \min\left\{1, \frac{SD}{SD_{max}}\right\} \quad 75)$$

3.6 CMAQ M3Dry

M3Dry (Pleim and Ran, 2011) is designed to couple with the Pleim-Xiu land surface model (PX LSM; Pleim and Xiu, 1995) in the Weather Research and Forecasting (WRF) model and is used operationally in CMAQ. There is also M3Dry-psn, which follows M3Dry but uses a coupled photosynthesis-stomatal conductance model. M3Dry-psn was developed and evaluated with the intention to supplement PX LSM and M3Dry in CMAQ (Ran et al., 2017). To date, however, M3Dry-psn has not been implemented in CMAQ. Parameters in Table S12 are site-specific.

3.6.1 Surface resistance

Surface resistance (r_c) follows:

$$r_c = \left(f_{veg}\left(\frac{1}{r_{st}+r_m} + \frac{(1-f_{wet})\,LAI}{r_{cut,dry}} + \frac{f_{wet}\,LAI}{r_{cut,wet}} + \frac{1}{r_{ac}+r_g}\right) + \frac{1-f_{veg}}{r_g}\right)^{-1} \quad (76)$$

The parameter f_{veg} is the fraction of the site covered by the vegetation canopy (Table S12); f_{wet} is the fraction of canopy that is wet (Table 1).

3.6.2 $r_m = \frac{0.01}{LAI}$ Stomatal and mesophyll resistances

For M3Dry, stomatal resistance (r_{st}) follows Xiu and Pleim (2001):

$$r_{st} = R_{diff,st} \frac{r_i}{LAI\,f(PAR)\,f(w_2)\,f(RH_l)\,f(T_a)} \quad (77)$$

The parameter r_i is initial resistance to stomatal uptake (Table S12).

Effects of photosynthetically active radiation (PAR) [μmol m^{-2} s^{-1}] (Table 1) follow Echer and Rosolem (2015):

805   $f(PAR) = (1 - a\,LAI)(1 - e^{-0.0017\,PAR})$ (78)

806   The parameter a [unitless] is empirical (Table S12).

807   Effects of w_2 follow Xiu and Pleim (2001):

808   $f(w_2) = \left(1 + e^{-5\left(\frac{w_2 - w_{wlt}}{w_{fc} - w_{wlt}} - \left(\frac{w_{fc} - w_{wlt}}{3} + w_{wlt}\right)\right)}\right)^{-1}$ (79)

809   Effects of leaf-level RH (RH_l) [fractional] follow:

810   $f(RH_l) = RH_l = \frac{q_a\,(r_a + r_{b,v})^{-1} + q_s\,r_{st,v}^{-1}}{(r_{st,v}^{-1} + (r_a + r_{b,v})^{-1})\,q_s}$ (80)

811   The variable q_a is ambient air humidity mixing ratio, q_s is saturation mixing ratio at leaf temperature (T_{leaf}), $r_{b,v}$ is quasi-laminar

812   boundary layer resistance for water vapor and $r_{st,v}$ is stomatal resistance for water vapor. M3Dry assumes that when sensible heat

813   flux (SH) [W m^{-2}] (Table 1) is greater than 0, then T_{leaf} equals $T_a - \frac{SH}{(r_a + r_{b,h})\,\rho\,c_p}$ where $r_{b,h}$ is quasi-laminar boundary layer

814   resistance for heat. Otherwise, T_{leaf} equals T_a. Eq. (80) is computed using an implicit quadratic solution as described by Xiu and

815   Pleim (2001).

816   Effects of T_a follow:

817   $f(T_a) = \begin{cases} (1 + e^{-0.41(T_a - 8.9)})^{-1}, & T_a \leq 29 \\ (1 + e^{0.5(T_a - 40.85)})^{-1}, & T_a > 29 \end{cases}$ (81)

818   $r_{cut,wet} = \begin{cases} 1250, & T_g > 0 \\ 6667, & T_g < 0 \end{cases}$ $r_{cut,dry} = r_{cut,dry,0}(1 - f(RH)) + r_{cut,wet}\,f(RH)\,f(RH) = r_{ac} = 14\frac{h\,LAI}{u_*}$ $r_{g,wet} =$

819   $\begin{cases} 500, & T_g > 0 \\ 6667, & T_g < 0 \end{cases}$ $r_{g,dry} = 200 + (r_{g,wet} - 200)\frac{w_g}{w_{fc}}$ $X_m = \begin{cases} \max\{0.02(T_a + 1)^2,\ 0.5\}, & T_a > -1 \\ 0, & T_a < -1 \end{cases}$

820   For M3Dry-psn, r_{st} is simulated at leaf level using the Ball-Woodrow-Berry approach (Ball et al., 1987) as described by Collatz

821   et al. (1991, 1992) and Bonan et al. (2011):

822   $r_{st} = \left(g_0 + g_1\frac{A_n}{\frac{p_{CO_2,l}}{p_a}}\,RH_l\right)^{-1}\frac{D_{CO_2}}{D_{O_3}}\frac{1000.0\,\rho}{M_{air}}$ (82)

823   The parameter g_0 equals 0.01 mol CO_2 m^{-2} s^{-1} for C$_3$ plants; g_1 equals 9 [unitless]; A_n is leaf-level net photosynthesis [mol CO_2

824   m^{-2} s^{-1}]; $p_{CO_2,l}$ is carbon dioxide partial pressure at the leaf surface [Pa]; RH_l is leaf-level RH [fractional], which follows Eq. (80)

825   as described for M3Dry; D_{CO_2} [m^2 s^{-1}] is carbon dioxide diffusivity in air (Table 1); ρ [kg m^{-3}] is air density (Table 1); M_{air} [g mol^{-}

826   ^{1}] is molar mass of air (Table 1). Leaf-level A_n is estimated based on Farquhar et al. (1980) as described by Ran et al. (2017),

827   based on co-limitation among three potential assimilation rates, limited by Rubisco, light, and transport of photosynthetic products.

828   The maximum rate of carboxylation of Rubisco (V_{cmax}) [µmol m^2 s^{-1}] is key for A_n and thus we include values at 25°C in Table

829   S12.

830   Leaf-level A_n and r_{st} are calculated separately for sunlit versus shaded leaves in M3Dry-psn. Sunlit and shaded portions of LAI

831   (LAI_{sun} and LAI_{shd}, respectively) follow Campbell and Norman (1998) and Song et al. (2009). Canopy scale r_{st} follows:

$$r_{st} = \left(\left(\frac{LAI_{sun}}{r_{st,sun}} + \frac{LAI_{shd}}{r_{st,shd}} \right) f(w_2) \right)^{-1} \quad (83)$$

Variables $r_{st,sun}$ and $r_{st,shd}$ are leaf-level stomatal resistances for sunlit and shaded leaves, respectively, calculated via Eq. (82).

The function $f(w_2)$ follows Eq. (79).

For both M3Dry and M3Dry-psn, mesophyll resistance (r_m) follows:

$$r_m = \frac{0.01}{LAI} \quad (84)$$

3.6.3 Cuticular resistances

The variable $r_{cut,wet}$ is the resistance to wet cuticles:

$$r_{cut,wet} = \begin{cases} 1250, T_g > 0 \\ 6667, T_g < 0 \end{cases} \quad (85)$$

The variable T_g [ºC] is ground temperature near surface (Table 1).

The variable $r_{cut,dry}$ is resistance to dry cuticles:

$$r_{cut,dry} = r_{cut,dry,0}(1 - f(RH)) + r_{cut,wet} f(RH) \quad (86)$$

The parameter $r_{cut,dry,0}$ equals 2000 s m^{-1}.

Effects of RH follow:

$$f(RH) = \max \left(100 \frac{RH - 0.7}{0.3}, 0 \right) \quad (87)$$

3.6.4 Resistance to the ground (and associated resistance to transport)

The resistance to in-canopy turbulence (r_{ac}) follows Erisman et al. (1994):

$$r_{ac} = 14 \frac{h \, LAI}{u_*} \quad (88)$$

Ground resistance (r_g) follows:

$$r_g = \begin{cases} \left(\frac{1 - f_{wet}}{r_{g,dry}} + \frac{f_{wet}}{r_{g,wet}} \right)^{-1}, \text{ no snow} \\ \left(\frac{1 - X_m}{r_{snow}} + \frac{X_m}{r_{sndiff} + r_{g,wet}} \right)^{-1}, \text{ snow} \end{cases} \quad (89)$$

$$r_{g,wet} = \begin{cases} 500, T_g > 0 \\ 6667, T_g < 0 \end{cases} \quad (90)$$

The variable $r_{g,dry}$ follows (Massman, 2004; Mészáros et al., 2009):

$$r_{g,dry} = 200 + \left(r_{g,wet} - 200 \right) \frac{w_g}{w_{fc}} \quad (91)$$

If near-surface soil water content (w_g) [m^3 m^{-3}] (Table 1) is greater than w_{fc} then soil is wet (i.e., $r_{g,dry}$ equals $r_{g,wet}$). The parameter r_{snow} is resistance to snow or ice [6667 s m^{-1}]; r_{sndiff} is resistance to diffusion through snowpack [10 s m^{-1}]. Parallel

pathways to frozen snow/ice and diffusion through snowpack to liquid water follow Bales et al. (1987). Snow liquid water mass (X_m) follows:

$$X_m = \begin{cases} \max\{0.02(T_a + 1)^2, \ 0.5\}, \ T_a > -1 \\ 0, T_a < -1 \end{cases} \quad (92)$$

3.7 CMAQ STAGE

The Surface Tiled Aerosol and Gaseous Exchange (STAGE) parameterization is an option in CMAQ. Parameters in Table S13 are site-specific.

3.7.1 Deposition velocity

$$v_d = f_{veg}\left(r_a + \frac{1}{\frac{1}{r_{b,v} + \frac{1}{\frac{1}{r_{st} + r_m} + \frac{1}{r_{cut}}}} + \frac{1}{r_{ac} + r_{b,g} + r_g}}\right)^{-1} + (1 - f_{veg})(r_a + r_{b,g} + r_g)^{-1} \quad (93)$$

CMAQ STAGE considers separate quasi-laminar boundary layer resistances around vegetation versus the ground ($r_{b,v}$ and $r_{b,g}$, respectively) (Table S3). The parameter f_{veg} is the vegetated fraction of the site; the M3Dry value is used (Table S12).

3.7.2 Stomatal and mesophyll resistances

Stomatal resistance (r_{st}) follows Pleim and Ran (2011):

$$r_{st} = R_{diff,st} \frac{r_i}{LAI\, f(PAR)\, f(w_2)\, f(RH_l)\, f(T_a)} \quad (94)$$

The parameter r_i is initial resistance to stomatal uptake (Table S13). The functions follow M3Dry (Eq. (78)-(81)).

Mesophyll resistance (r_m) follows Wesely (1989):

$$r_m = \left(\frac{H}{3000} + 100\, f_0\right)^{-1} \quad (95)$$

3.7.3 Cuticular resistance

Cuticular resistance (r_{cut}) follows:

$$r_{cut} = \left(LAI\left(\frac{f_{wet}}{1250} + \frac{1 - f_{wet}}{2000}\right)\right)^{-1} \quad (96)$$

3.7.4 Resistance to the ground (and associated resistance to transport)

The resistance to in-canopy turbulence (r_{ac}) is similar to Shuttleworth and Wallace (1985):

$$r_{ac} = \int_0^h \frac{dz}{K_t} \quad (97)$$

The variable K_t is in-canopy eddy diffusivity [$m^2\ s^{-1}$]. By applying the drag coeffiecient ($C_d = \frac{u_*^2}{u^2}$), assuming a uniform vertical distribution of leaves, and using an in-canopy attenuation coefficient of momentum following Yi (2008) [$\frac{LAI}{2}$]:

$$r_{ac} = Pr\, \frac{u}{u_*^2}\left(e^{\frac{LAI}{2}} - 1\right) = r_a\left(e^{\frac{LAI}{2}} - 1\right) \quad (98)$$

949 The variable u [m s^{-1}] is wind speed (Table 1).

950 The resistance to the ground (r_g) changes whether the ground is snow covered, dry or wet (wet is w_g greater than or equal to w_{sat}

951 where w_{sat} [m^3 m^{-3}] is soil water content at saturation (Table 1)). For dry ground, r_g follows Fares et al. (2014) and Fumagalli et

952 al. (2016). An asymptotic function bounds the resistance, following observations reported in Fumagalli et al. (2016):

953
$$r_g = \begin{cases} 250 + 2000 \, \text{atan}\left(\dfrac{\left(\dfrac{w_g - w_{wlt}}{w_{fc}}\right)^B}{\pi}\right), w < w_{sat} \\ \dfrac{62500}{H\,R\,(T_g + 273.15)}, \ w \geq w_{sat} \\ \dfrac{1 - X_m}{r_{snow}} + \dfrac{X_m}{r_{sndiff} + \dfrac{62500}{H\,R\,(T_g + 273.15)}}, \ \text{snow} \end{cases} \tag{99}$$

954 The parameter R [L atm K^{-1} mol^{-1}] is the universal gas constant; B [unitless] is an empirical parameter related to soil moisture

955 (Table 1); r_{snow} is resistance to snow or ice [6667 s m^{-1}]; r_{sndiff} is resistance to diffusion through snowpack [10 s m^{-1}]. The liquid

956 fraction of the quasi-liquid layer in snow (X_m) is modeled as a system dominated by van der Waals forces using the temperature

957 parameterization following Huthwelker et al. (2006), and assuming a maximum of 20% to match gas-liquid partitioning findings

958 in Conklin et al. (1993):

959
$$X_m = \begin{cases} \dfrac{0.025}{(273.15 - T_g)^{1/3}}, & 0.002 < 273.15 - T_g < 10 \\ 0.2, & 273.15 - T_g < 0.002 \end{cases} \tag{100}$$

960 **3.8 TEMIR**

961 The Terrestrial Ecosystem Model in R (TEMIR) provides two dry deposition schemes (Sun et al., 2022): Wesely and Zhang.

962 Wesely in TEMIR largely follows GEOS-Chem version 12.0.0, while Zhang follows Zhang et al. (2003). In both schemes, the

963 default stomatal resistance is highly empirical. TEMIR can also use two photosynthesis-based stomatal conductance models

964 (hereinafter, psn): the Farquhar-Ball-Berry model (hereinafter, BB; Farquhar et al., 1980; Ball et al., 1987) and the Medlyn et al.

965 (2011) model (hereinafter, Medlyn). Thus, for TEMIR Wesely and Zhang, three stomatal conductance models are used for each.

966 TEMIR Zhang parameters in Table S14 and TEMIR psn parameters in Table S15 are site-specific.

967 **3.8.1 Surface resistance**

968 For Wesely, surface resistance (r_c) follows:

969
$$r_c = \left(\frac{1}{r_{st}} + \frac{1}{r_{cut}} + \frac{1}{r_{dc} + r_{cl}} + \frac{1}{r_{ac} + r_g}\right)^{-1} \tag{101}$$

970

971 For Zhang, surface resistance (r_c) follows:

972
$$r_c = \left(\frac{1 - W}{r_{st}} + \frac{1}{r_{cut}} + \frac{1}{r_{ac} + r_g}\right)^{-1} \tag{102}$$

973 The parameter W [fractional] is used to account for leaf wetness. If P is greater than 0.2 mm hr^{-1} then:

$$W = \begin{cases} 0, & G \leq 200 \\ \frac{G-200}{800}, & 200 \leq G \leq 600 \\ 0.5, & G > 600 \end{cases} \quad (103)$$

3.8.2 Stomatal resistance

For Wesely, stomatal resistance (r_{st}) follows:

$$r_{st} = R_{diff,st} \frac{r_i}{LAI_{eff} f(T_a)} \quad (104)$$

The parameter r_i is initial resistance to stomatal uptake (same for GEOS-Chem Wesely; Table S6); LAI_{eff} [m^2 m^{-2}] is effective LAI, which is the surface area of actively transpiring leaves per ground surface area. The variable LAI_{eff} is calculated using function of LAI, θ, and cloud fraction using a parameterization developed by Wang et al. (1998). In GEOS-Chem, if G is zero then LAI_{eff} equals 0.01. For the single-point model, we set G to be zero when θ is greater than 95° so that nighttime r_{st} values in the single-point model more similar GEOS-Chem. GEOS-Chem almost never has non-zero G at night but measured values are frequently small and non-zero. Here cloud fraction is assumed to be zero.

Effects of T_a follow:

$$f(T_a) = \begin{cases} 0.01, & T_a \leq 0 \\ T_a \frac{(40-T_a)}{400}, & 0 < T_a < 40 \\ 0.01, & 40 \leq T_a \end{cases} \quad (105)$$

$$r_{cut} = \begin{cases} r_{lu} \min\{2, e^{0.2(-1-T_a)}\} \left(\frac{H}{10^5} + f_0\right)^{-1}, & T_a < -1 \\ \left(\frac{r_{lu}}{LAI} + 1000 \, e^{-T_a - 4}\right) \left(\frac{H}{10^5} + f_0\right)^{-1}, & T_a \geq -1 \end{cases} \quad r_{dc} = 100 \left(1 + \frac{1000}{G+10}\right) \quad r_{cl} = \left(\frac{H}{10^5 r_{cl,S}} + \frac{f_0}{r_{cl,O}}\right)^{-1} \quad r_g = \left(\frac{H}{10^5 r_{g,S}} + \frac{f_0}{r_{g,O}}\right)^{-1}$$

For Zhang, stomatal resistance (r_{st}) follows:

$$r_{st} = R_{diff,st} \frac{r_i(LAI, PAR)}{f(T_a) f(VPD) f(\psi_{leaf})} \quad (106)$$

Dependencies on T_a, VPD, and ψ_{leaf} are as described in Brook et al. (1999).

The variable $r_i(LAI, PAR)$ follows:

$$r_i(LAI, PAR) = \left(\frac{LAI_{sun}}{r_i\left(1 + \frac{b_{rs}}{PAR_{sun}}\right)} + \frac{LAI_{shd}}{r_i\left(1 + \frac{b_{rs}}{PAR_{shd}}\right)}\right)^{-1} \quad (107)$$

The parameter r_i is initial resistance to stomatal uptake (Table S14); b_{rs} [W m^{-2}] is empirical (Table S14); LAI_{sun} and LAI_{shd} [m^2 m^{-2}] are sunlit and shaded LAI:

$$LAI_{sun} = \frac{1 - e^{-K_b LAI}}{K_b} \quad (108)$$

$$LAI_{shd} = LAI - LAI_{sun} \quad (109)$$

The variable K_b is canopy light extinction coefficient [unitless]:

064    $K_b = \frac{0.5}{\cos\left(\frac{\pi}{180}\theta\right)}$ (110)

065   The variables PAR_{sun} and PAR_{shd} [W m^{-2}] are PAR reaching sunlit and shaded leaves:

066    $PAR_{shd} = R_{diff}\, e^{-0.5\, LAI^a} + 0.07\, R_{dir}\,(1.1 - 0.1\, LAI)\, e^{-\cos\left(\frac{\pi}{180}\theta\right)}$ (111)

067    $PAR_{sun} = PAR_{shd} + \frac{R_{dir}^b \cos\left(\frac{\pi}{180}\alpha\right)}{\cos\left(\frac{\pi}{180}\theta\right)}$ (112)

068   The parameter α is the angle between the leaf and the sun [60º]; R_{diff} and R_{dir} are downward visible radiation fluxes from diffuse

069   and direct-beam radiation above the canopy. Here we use diffuse fraction from the reanalysis product Modern-Era Retrospective

070   analysis for Research and Applications, Version 2 (MERRA-2) (GMAO, 2015) to separate R_{diff} and R_{dir} from observed PAR. If

071   LAI is less than 2.5 m^2 m^{-2} or G is less than 200 W m^{-2} then a equals 0.7 and b equals 1. Otherwise, a equals 0.8 and b equals 0.8.

072   Effects of T_a follow:

073    $f(T_a) = \left(\frac{T_a - T_{min}}{T_{opt} - T_{min}}\right)\left(\frac{T_{max} - T_a}{T_{max} - T_{opt}}\right)^{\frac{T_{max} - T_{opt}}{T_{opt} - T_{min}}}$ (113)

074   Parameters T_{min}, T_{max}, and T_{opt} [ºC] are minimum, maximum, and optimum temperature, respectively (Table S14).

075   Effects of VPD follow:

076    $f(VPD) = 1 - b_{VPD}\, VPD$ (114)

077   The parameter b_{VPD} [kPa^{-1}] is empirical (Table S14).

078   Effects of ψ_{leaf} follow:

079    $f(\psi_{leaf}) = \frac{\psi_{leaf} - \psi_{leaf,2}}{\psi_{leaf,1} - \psi_{leaf,2}}$ (115)

080   Parameters $\psi_{leaf,1}$ and $\psi_{leaf,2}$ [MPa] are empirical (Table S14); ψ_{leaf} is parameterized as:

081    $\psi_{leaf} = -0.72 - 0.0013\, G$ (116)

082    $r_{cut} = \begin{cases} \frac{c_{cut,dry}}{u^* LAI^{0.25}\, e^{3\,RH}}, & dry \\ \frac{c_{cut,wet}}{u^* LAI^{0.5}}, & wet \end{cases}$ $r_{cut} = \left(\frac{1 - f_{snow}}{r_{cut}} + \frac{2 f_{snow}}{2000}\right)^{-1}$ $r_{ac}\frac{LAI^{0.25}}{(u^*)^2}$ $r_{ac0} = r_{ac0,min} + \frac{LAI - LAI_{min}}{LAI_{max} - LAI_{min}}(r_{ac0,max} - r_{ac0,min})$ $r_g =$

083    $\left(\frac{1 - \min\{1,2f_{snow}\}}{200} + \frac{\min\{1,2f_{snow}\}}{2000}\right)^{-1}$ $f_{snow} = \min\left\{1, \frac{SD}{SD_{max}}\right\}$

084   We now describe psn options for TEMIR Wesely and TEMIR Zhang. For BB (Ball et al., 1987; Farquhar et al., 1980; von

085   Caemmerer and Farquhar, 1981; Collatz et al., 1991, 1992),

086    $r_{st} = \left(\beta_t\, g_0 + g_1\, \frac{A_n\, RH}{\frac{p_{CO_2,l}}{p_a}}\right)^{-1} \frac{p_a}{R\,\theta_a}$ (117)

087   The parameter g_0 equals 0.01 mol m^{-2} s^{-1}; g_1 equals 9; A_n is net photosynthesis [mol m^{-2} s^{-1}]; β_t is a soil water stress factor

088   [unitless]; $p_{CO_2,l}$ is carbon dioxide partial pressure at leaf surface [Pa]; R is the universal gas constant [J mol^{-1} K^{-1}]; θ_a is potential

089   air temperature [K].

090

For Medlyn (Medlyn et al., 2011),

$$r_{st} = \left(\beta_t \, g_0 + \frac{D_w}{D_{CO_2}} \left(1 + \frac{g_{1M}}{\sqrt{VPD}}\right) \frac{A_n}{\frac{p_{CO_2,l}}{p_a}} \right)^{-1} \frac{p_a}{R \, \theta_a} \quad (118)$$

The parameter g_{1M} [kPa$^{0.5}$] is empirical (Table S15); g_0 equals 0.0001 mol m^{-2} s^{-1}; D_w [m^2 s^{-1}] is the diffusivity of water vapor in air (Table 1); the ratio of diffusivities is 1.6.

A single-layer bulk soil formulation considering the root zone (0-100 cm) is used to calculate β_t:

$$\beta_t = \begin{cases} 1, & \psi_{soil} > \psi_{soil,fc} \\ \frac{\psi_{soil,wlt} - \psi_{soil}}{\psi_{soil,wlt} - \psi_{soil,fc}}, & \psi_{soil,wlt} \leq \psi_{soil} \leq \psi_{soil,fc} \quad (119) \\ 0, & \psi_{soil} < \psi_{soil,fc} \end{cases}$$

The variable ψ_{soil} [kPa] is soil matric potential (Table 1):

$$\psi_{soil} = \psi_{soil,sat} \, w_2^{-B} \quad (120)$$

For both Medlyn and BB, leaf-level r_{st} is calculated individually for sunlit and shaded leaves, and then scaled up:

$$r_{st} = R_{diff,st} \left(\frac{LAI_{sun}}{r_{b,leaf} + r_{st,sun}} + \frac{LAI_{shd}}{r_{b,leaf} + r_{st,shd}} \right)^{-1} \quad (121)$$

Variables $r_{st,sun}$ and $r_{st,shd}$ are leaf-level stomatal resistances for sunlit and shaded leaves, respectively; LAI_{sun} and LAI_{shd} are sunlit and shaded LAI, respectively; $r_{b,leaf}$ is leaf boundary layer resistance:

$$r_{b,leaf} = \frac{1}{c_v} \sqrt{\frac{\overline{u_*}}{l}} \quad (122)$$

The parameter c_v [0.01 m s$^{-0.5}$] is the turbulent transfer coefficient; l [0.04 m] is the characteristic dimension of leaves.

Variables LAI_{sun} and LAI_{shd} follow:

$$LAI_{sun} = PAI_{sun} \frac{LAI}{LAI + SAI} \quad (123)$$

$$LAI_{shd} = PAI_{shd} \frac{LAI}{LAI + SAI} \quad (124)$$

The variable SAI [m^2 m^{-2}] is stem area index; PAI_{sun} and PAI_{shd} [m^2 m^{-2}] are sunlit and shaded plant area index, respectively:

$$PAI_{sun} = \frac{1 - e^{-K_b(LAI + SAI)}}{K_b} \quad (125)$$

$$PAI_{shd} = LAI + SAI - PAI_{sun} \quad (126)$$

The variable SAI follows Zeng et al. (2002):

$$SAI_n = \max \{0.5 \, SAI_{n-1} + \max\{LAI_{n-1} - LAI_n, 0\}, 1\} \quad (127)$$

The parameter n is nth month of the year.

Leaf-level photosynthesis of C$_3$ plants is represented by the formulation that relates to Michaelis–Menten enzyme kinetics and photosynthetic biochemical pathways, as in Community Land Model 4.5 (CLM4.5) (Oleson et al., 2013) and following Collatz et al. (1992):

177    $A_n = \min\{A_c, A_j, A_p\} - R_d$ (128)

Deleted: 148

178   The Rubisco-limited photosynthetic rate (A_c) [mol m^{-2} s^{-1}] follows:

179    $A_c = V_{cmax} \dfrac{c_i - \Gamma_*}{c_i + K_c\left(1 + \frac{o_i}{K_o}\right)}$ (129)

Deleted: 149

180   The variable c_i is intercellular carbon dioxide partial pressure [Pa]; K_c and K_o are Michaelis–Menten constants for carboxylation

181   and oxygenation [Pa]; o_i is intercellular oxygen partial pressure [0.029 p_a Pa]; Γ_* is carbon dioxide compensation point [Pa]; V_{cmax}

182   is maximum rate of carboxylation [mol m^{-2} s^{-1}] adjusted for leaf temperature:

183    $V_{cmax} = V_{cmax,25}\, f(T_l)\, f_H(T_l)\, \beta_t$ (130)

Deleted: 150

184   The parameter $V_{cmax,25}$ is the value of V_{cmax} at 25ºC (Table S15).

185   The function of leaf temperature (T_l) [K] follows:

186    $f(T_l) = e^{\frac{\Delta H_a}{298.15 * 0.001 R}\left(1 - \frac{298.15}{T_l}\right)}$ (131)

Deleted: 151

187   The parameter R is the universal gas constant [J kg^{-1} K^{-1}]. The high temperature function of T_l follows:

188    $f_H(T_l) = \dfrac{1 + e^{\frac{298.15\, \Delta S - \Delta H_d}{298.15 * 0.001\, R}}}{1 + e^{\frac{\Delta S T_v - \Delta H_d}{0.001\, R\, T_l}}}$ (132)

Deleted: 152

189   The variables ΔH_a [J mol^{-1}], ΔS [J mol^{-1} K^{-1}], and ΔH_d [J mol^{-1}] are temperature dependent and follow definitions in CLM4.5 (see

190   Table S15 for the CLM4.5 plant functional types used for each site).

Deleted: PFTs

191   The ribulose-1,5-bisphosphate (RuBP)-limited photosynthetic rate (A_j) [mol m^{-2} s^{-1}] follows:

192    $A_j = \dfrac{J}{4} \dfrac{c_i - \Gamma_*}{c_i + 2\Gamma_*}$ (133)

Deleted: 153

193   The parameter J is the electron transport rate [mol m^{-2} s^{-1}], taken as the smaller of the two roots of the equation below:

194    $\theta_{PSII} J^2 - (I_{PSII} + J_{max}) J + I_{PSII} J_{max} = 0$ (134)

Deleted: 154

195    $J_{max} = 1.97\, V_{cmax,25}\, f(T_l)\, f_H(T_l)$ (135)

Deleted: 155

196    $I_{PSII} = 0.5\, \Phi_{PSII}\, 4.6\, x\, 10^{-6}\, \phi$ (136)

Deleted: 156

197   The parameter θ_{PSII} [unitless] represents curvature; I_{PSII} [mol m^{-2} s^{-1}] is light utilization in electron transport by photosystem II;

198   J_{max} [mol m^{-2} s^{-1}] is potential maximum electron transport rate; Φ_{PSII} [unitless] is quantum yield of photosystem II; ϕ [W m^{-2}] is

199   photosynthetically active radiation absorbed by leaves, converted to photosynthetic photon flux density with 4.6 x 10^{-6} mol J^{-1}.

200   The product-limited photosynthetic rate (A_p) [mol m^{-2} s^{-1}] follows:

201    $A_p = 3\, T_p$ (137)

Deleted: 157

202   The parameter T_p is the triose phosphate utilization rate [mol m^{-2} s^{-1}].

203    $T_p = 0.167\, V_{cmax,25}\, f(T_l)\, f_H(T_l)$ (138)

Deleted: 158

204   Dark respiration (R_d) [mol m^{-2} s^{-1}] follows:

205    $R_d = 0.015\, V_{cmax,25}\, f(T_l)\, f_H(T_l)\, \beta_t$ (139)

Deleted: 159

206   Calculation for A_n and r_{st} involves a coupled set of equations that are solved iteratively at each time step until c_i converges (see

207   Sect. 8.5 of Oleson et al., 2013):

221 $$A_n = \frac{p_{CO_2,a} - p_{CO_2,i}}{\left(1.4\, r_{b,leaf} + \frac{D_w}{D_{CO_2}}\, r_{st}\right) p_a} = \frac{p_{CO_2,a} - p_{CO_2,l}}{1.4\, r_{b,leaf}\, p_a} = \frac{p_{CO_2,l} - p_{CO_2,i}}{\frac{D_w}{D_{CO_2}}\, r_{st}\, p_a} \quad (130)$$

222 Variables $p_{CO_2,a}$, $p_{CO_2,l}$, and $p_{CO_2,i}$ are carbon dioxide partial pressure [Pa] in air, at leaf level, and in intercellular space,

223 respectively.

3.8.3 Cuticular resistance

225 For Wesely, cuticular resistance (r_{cut}) follows:

226 $$r_{cut} = \begin{cases} r_{lu} \min\{2, e^{0.2(-1-T_a)}\} \left(\frac{H}{10^5} + f_0\right)^{-1}, T_a < -1 \\ \left(\frac{r_{lu}}{LAI} + 1000\, e^{-T_a - 4}\right) \left(\frac{H}{10^5} + f_0\right)^{-1}, T_a \geq -1 \end{cases} \quad (131)$$

227 The parameter r_{lu} is initial resistance for cuticular uptake. Values follow GEOS-Chem Wesely (Table S6).

229 For Zhang, cuticular resistance (r_{cut}) follows:

230 $$r_{cut} = \begin{cases} \frac{c_{cut,dry}}{u^* LAI^{0.25}\, e^{3\,RH}}, dry \\ \frac{c_{cut,wet}}{u^* LAI^{0.5}}, wet \end{cases} \quad (132)$$

231 Parameters $c_{cut,dry}$ and $c_{cut,wet}$ [unitless] are empirical coefficients related to dry and wet cuticular uptake (Table S14). If P is

232 greater than 0.2 mm hr^{-1} then cuticles are wet; otherwise, cuticles are dry.

233 The variable r_{cut} is adjusted for snow:

234 $$r_{cut} = \left(\frac{1 - f_{snow}}{r_{cut}} + \frac{2 f_{snow}}{2000}\right)^{-1} \quad (133)$$

3.8.4 Resistances to the lower canopy and ground (and associated resistances to transport)

236 For Wesely, the resistance associated with in-canopy convection (r_{dc}) follows:

237 $$r_{dc} = 100 \left(1 + \frac{1000}{G + 10}\right) \quad (134)$$

238 The resistance to the lower canopy (r_{cl}) follows:

239 $$r_{cl} = \left(\frac{H}{10^5\, r_{cl,S}} + \frac{f_0}{r_{cl,O}}\right)^{-1} \quad (135)$$

240 Parameters $r_{cl,S}$ and $r_{cl,O}$ are initial resistances to uptake to the lower canopy and follow GEOS-Chem Wesely (Table S6).

241 Resistance to the ground (r_g) follows:

242 $$r_g = \left(\frac{H}{10^5\, r_{g,S}} + \frac{f_0}{r_{g,O}}\right)^{-1} \quad (136)$$

243 Parameters $r_{g,S}$ and $r_{g,O}$ are initial resistances to the ground and follow GEOS-Chem Wesely (Table S6). The resistance to turbulent

244 transport to the ground (r_{ac}) follows GEOS-Chem Wesely (Table S6). The changes in resistances when there is snow follow GEOS-

245 Chem Wesely (Table S6).

247 For Zhang, in-canopy aerodynamic resistance (r_{ac}) follows:

249   $r_{ac} = r_{ac0} \frac{LAI^{0.25}}{(u_*)^2}$ (137)

250   The variable r_{ac0} follows:

251   $r_{ac0} = r_{ac0,min} + \frac{LAI - LAI_{min}}{LAI_{max} - LAI_{min}} \left(r_{ac0,max} - r_{ac0,min} \right)$ (138)

252   Variables LAI_{min} and LAI_{max} [m² m⁻²] are minimum and maximum observed LAI during a specific year; $r_{ac0,min}$ and $r_{ac0,max}$ are

253   initial resistances (Table S14).

254   Resistance to the ground (r_g) follows:

255   $r_g = \left(\frac{1 - \min\{1,2 f_{snow}\}}{200} + \frac{\min\{1,2 f_{snow}\}}{2000} \right)^{-1}$ (139)

256   The variable f_{snow} is the fraction of the surface covered by snow [unitless]:

257   $f_{snow} = \min\left\{ 1, \frac{SD}{SD_{max}} \right\}$ (140)

258   **3.9 DO₃SE**

259   DO₃SE as described below is consistent with the parameterization in the EMEP model (Simpson et al., 2012). DO₃SE uses two

260   methods to estimate r_{st}: the multiplicative method based on Jarvis (1976) ("DO₃SE multi") and the coupled photosynthesis-

261   stomatal conductance method based on Leuning (1995) ("DO₃SE psn"). Unless stated otherwise, the components are the same

262   between DO₃SE multi and then to DO₃SE psn. Parameters in Table S16 are site-specific.

263   **3.9.1 Surface resistance**

264   Surface resistance (r_c) follows:

265   $r_c = \left(\frac{LAI}{r_{st}} + \frac{StAI}{r_{cut}} + \frac{1}{r_{ac} + r_g} \right)^{-1}$ (141)

266   The parameter $StAI$ is the stand area index [m² m⁻²].

267   For forests,

268   $StAI = LAI + 1$ (142)

269   For the other LULC types examined here,

270   $StAI = LAI$ (143)

271   $r_{ac} = 14 \frac{h \, StAI}{u_*}$ $r_g = 200 + 1000 \, e^{-T_a - 4} + 2000 \, \delta_{snow}$ **3.9.2 Stomatal resistance**

272   For DO₃SE multi, according to Simpson et al. (2012), stomatal resistance (r_{st}) follows:

273   $r_{st} = \left(g_{max} \max\{f_{min}, f(T_a) \, f(VPD) \, f(w_2)\} \, a_{phen} \, a_{light} \right)^{-1}$ (144)

274   The parameter g_{max} is maximum stomatal conductance [m s⁻¹] (Table S16); f_{min} is the minimum factor [unitless] (Table S16).

275   Effects of T_a follow:

276   $f(T_a) = \begin{cases} \frac{T_a - T_{min}}{T_{opt} - T_{min}} \left(\frac{T_{max} - T_a}{T_{max} - T_{opt}} \right)^{\frac{T_{max} - T_{opt}}{T_{opt} - T_{min}}}, & T_{min} \leq T_a \leq T_{max}, \\ 0.01, & \text{otherwise} \end{cases}$ (145)

Marginal annotations (tracked changes):

- Moved (insertion) [38]
- Moved (insertion) [39]
- Formatted: Justified
- Moved (insertion) [40]
- Formatted: Justified
- Moved (insertion) [41]
- Moved (insertion) [42]
- Formatted: Justified
- Deleted: 2.1
- Formatted: Justified
- Deleted: First, we describe
- Deleted: that
- Deleted: DO₃SE psn. Second, we describe the components unique to DO₃SE multi and
- Deleted: If we reference Table S16, then the parameter's value is in the table.
- Formatted: English (UK)
- Formatted: English (US)
- Formatted: Justified
- Deleted: 161
- Formatted: English (US)
- Deleted: r_{cut} is resistance to cuticular uptake [2500 s m⁻¹];
- Deleted: 162
- Deleted: 163
- Moved down [43]: The resistance to in-canopy turbulence (r_{ac}) follows Erisman et al. (1994): ¶ $r_{ac} = 14 \frac{h \, StAI}{u_*}$ (
- Moved down [44]: (r_g) follows:¶ $r_g = 200 + 1000 \, e^{-T_a - 4} + 2000 \, \delta_{snow}$
- Moved down [45]: The parameter δ_{snow} equals 1 when snow is present and 0 when snow is absent.¶
- Deleted: 164)¶ Resistance to soil
- Deleted: (165)¶
- Formatted: English (UK)
- Formatted: Justified
- Deleted: 166
- Deleted: $f(T_a) = \frac{T_a - T_{min}}{T_{opt} - T_{min}} \left(\frac{T_{max} - T_a}{T_{opt} - T_{opt}} \right)^{\frac{T_{max} - T_{opt}}{T_{opt} - T_{min}}}$ (167)¶

The parameters T_{min}, T_{max}, and T_{opt} [ºC] are minimum, maximum, and optimum temperature, respectively (Table S16).

Effects of VPD follow:

$$f(VPD) = \min\left\{1, \max\left\{f_{min}, f_{min} + (1 - f_{min})\frac{VPD_{min} - VPD}{VPD_{min} - VPD_{max}}\right\}\right\} \quad (146)$$

Parameters VPD_{min} and VPD_{max} [kPa] are minimum and maximum VPD, respectively (Table S16).

Effects of w_2 follow:

$$f(w_2) = \min\left\{1, \max\left\{f_{min}, f_{min} + (1 - f_{min})\frac{w_{wlt} - w_2}{w_{max} - 0.5\,(w_{fc} - w_{wlt})}\right\}\right\} \quad (147)$$

The variable a_{phen} follows:

$$a_{phen} = \begin{cases} 0, d_y \le d_{SGS} \text{ or } d_y > d_{EGS} \\ \emptyset_a + \left(\frac{d_y - d_{SGS}}{(d_{SGS} + \emptyset_d) - d_{SGS}}\right)(\emptyset_b - \emptyset_a), d_{SGS} \le d_y < d_{SGS} + \emptyset_d \\ \emptyset_b, d_{SGS} + \emptyset_d < d_y \le d_{EGS} - \emptyset_e \\ \emptyset_b - \left(\frac{d_y - (d_{EGS} - \emptyset_e)}{d_{EGS} - \emptyset_e}\right)(\emptyset_b - \emptyset_c), d_{EGS} - \emptyset_e < d_y \le d_{EGS} \end{cases} \quad (148)$$

The variable d_y is the day of the year; d_{SGS} is day of the year that corresponds to the start of the growing season; d_{EGS} is the day of the year that corresponds to the end of the growing season. For forests, d_{SGS} and d_{EGS} are estimated whereby d_{SGS} equals 105 at 50ºN and alters by 1.5 day per degree latitude earlier on moving south and later on moving north, and d_{EGS} equals 297 at 50ºN and alters by 2 days per degree latitude earlier on moving north and later on moving south. The values of $\emptyset_a$, $\emptyset_b$, $\emptyset_c$, $\emptyset_d$, and $\emptyset_e$ are given in Table S16. For other LULC, we assume a year-long growing season.

The variable a_{light} follows:

$$a_{light} = \frac{LAI_{sun}}{LAI}\left(1 - e^{-\alpha\, I_{PAR}^{sun}}\right) + \frac{LAI_{shd}}{LAI}\left(1 - e^{-\alpha\, I_{PAR}^{shd}}\right) \quad (149)$$

The parameter α is empirical (Table S16); sunlit and shaded portions of LAI (LAI_{sun} and LAI_{shd}, respectively) follow Norman (1979, 1982):

$$LAI_{sun} = \left(1 - e^{-0.5\frac{LAI}{\cos\theta}}\right) 2\cos\theta \quad (150)$$

$$LAI_{shd} = LAI - LAI_{sun} \quad (151)$$

The variables I_{PAR}^{sun} and I_{PAR}^{shade} [W m^{-2}] follow:

$$I_{PAR}^{shd} = I_{diff}\, e^{-0.5\, LAI^{0.7}} + 0.07\, I_{dir}(1.1 - 0.1\, LAI)\, e^{-\cos\theta} \quad (152)$$

$$I_{PAR}^{sun} = \frac{I_{dir}\cos\alpha_1}{\cos\theta} + I_{PAR}^{shd} \quad (153)$$

The parameter α_1 is the average inclination of leaves [º60]; I_{diff} and I_{dir} are diffuse and direct radiation [W m^{-2}] estimated as a function of the potential to actual PAR. Potential PAR is estimated using standard solar geometry methods assuming no cloud cover and a sky transmissivity of 0.9.

For DO₃SE psn (Leuning, 1990, 1995), which requires an estimate of net photosynthesis (A_n) [mol CO$_2$ m^{-2} s^{-1}] (Farquhar et al., 1980), stomatal resistance (r_{st}) follows:

Deleted: function $f(T_a)$ equals 0.01 when T_a is outside T_{min} to T_{max};

Formatted: Justified

Deleted: 169

Deleted: 170

Deleted: 171

Deleted: 172

Deleted: 173

Deleted: 174

Deleted: 175

Deleted: PAR

Deleted: PAR

Deleted: ;

340 $$r_{st} = \left(g_0 + g_1 \frac{A_n}{([CO_2]_l - \Gamma_*)\left(1 + \left(\frac{VPD}{D_0}\right)^8\right)} \right)^{-1} \frac{D_{CO_2}}{D_{O_3}} \frac{1000.0\,\rho}{M_{air}} \quad (154)$$

341 The parameter g_0 is minimum conductance [mol air m^{-2} s^{-1}] (Leuning, 1990); g_1 is empirical [unitless]; D_0 is a parameter related

342 to VPD [kPa] (Leuning et al., 1998) (Table S16); $[CO_2]_l$ is the leaf surface carbon dioxide mixing ratio [mol CO_2 mol air^{-1}]; Γ_* is

343 carbon dioxide compensation point [mol CO_2 mol air^{-1}]. The ratio of the diffusivities is 0.96. The variable $[CO_2]_l$ is calculated

344 from $[CO_2]$ and leaf boundary layer resistance ($r_{b,leaf}$):

345 $$r_{b,leaf} = 186 \sqrt{\frac{\overline{u}}{l}} \quad (155)$$

346 The parameter l is the characteristic dimension of leaves [m].

347 The variable A_n follows Sharkey et al. (2007):

348 $$A_n = \min\{A_c, A_j, A_p\} - R_d \quad (156)$$

349 The parameter R_d is dark respiration [0.015 x 10^{-6} mol m^{-2} s^{-1}].

350 The Rubisco-limited rate (A_c) [mol m^{-2} s^{-1}] follows:

351 $$A_c = a_{phen} f(w_2) V_{cmax,25} \frac{[CO_2]_i - \Gamma_*}{[CO_2]_i + K_c\left(1 + \frac{o_i}{K_o}\right)} \quad (157)$$

352 The variable $[CO_2]_i$ is intercellular carbon dioxide partial pressure [Pa]; K_c and K_o are Michaelis–Menten constants for

353 carboxylation and oxygenation [Pa]; o_i is intercellular oxygen partial pressure [Pa]; Γ_* is CO_2 compensation point [Pa]; $V_{cmax,25}$ is

354 maximum rate of carboxylation at 25°C [mol m^{-2} s^{-1}] (Table S16); a_{phen} follows Eq. (148); $f(w_2)$ follows Eq. (147).

355 The ribulose-1,5-bisphosphate (RuBP)-limited rate (A_j) [mol m^{-2} s^{-1}] follows:

356 $$A_j = J \frac{[CO_2]_i - \Gamma_*}{a[CO_2]_i + b\,\Gamma_*} \quad (158)$$

357 The variable J is electron transport rate [mol m^{-2} s^{-1}]; a and b denote electron requirements for formation of NADPH and ATP,

358 respectively. We use a equals 4 and b equals 8 (Sharkey et al., 2007).

359 The product-limited photosynthetic rate (A_p) [mol m^{-2} s^{-1}] follows:

360 $$A_p = 0.5 V_{cmax,25} \quad (159)$$

361 **3.9.3 Cuticular resistance**

362 The resistance to cuticles (r_{cut}) is prescribed [2500 s m^{-1}].

363 **3.9.4 Resistances to the lower canopy and ground (and associated resistances to transport)**

364 The resistance to in-canopy turbulence (r_{ac}) follows Erisman et al. (1994):

365 $$r_{ac} = 14 \frac{h\,StAI}{u_*} \quad (160)$$

366 Resistance to the ground (r_g) follows:

367 $$r_g = 200 + 1000\,e^{-T_a - 4} + 2000\,\delta_{snow} \quad (161)$$

Deleted: 176

Deleted:

Deleted: We assume the diffusivity

Deleted: 177

Deleted: 178

Deleted: 179

Deleted: c_i

Deleted: 170

Deleted: 169

Deleted: $\frac{c_i - \Gamma_*}{a\,c_i + b\,\Gamma_*}$

Deleted: 180

Deleted: 181

Deleted: 2.1

Moved (insertion) [43]

Formatted: English (UK)

Formatted: Justified

Moved (insertion) [44]

Formatted: Justified

381 The parameter δ_{snow} equals 1 when snow is present and 0 when snow is absent.

382 **3.10 MLC-CHEM**

383 The Multi-layer Canopy and Chemistry Exchange Model (MLC-CHEM) has been applied to evaluate the role of in-canopy

384 interactions on atmosphere-biosphere exchanges and atmospheric composition at field sites (e.g., Visser et al., 2021) and the global

385 scale (e.g., Ganzeveld et al., 2010). MLC-CHEM requires a minimum h of 0.5 m so it has not been configured for all sites. The

386 canopy environment is represented by an understory and crown layer. However, radiation dependent processes such as biogenic

387 emissions, photolysis, and stomatal conductance are estimated at four canopy layers to consider observed large gradients in in-canopy

388 radiation as a function of the vertical distribution of biomass. For the single-point model, ~75% and ~25% of the total LAI is present in

389 the crown layer and understory, respectively. These canopy structure settings are used to calculate in-canopy profiles of direct and

390 diffusive radiation as well as the fraction of sunlit leaves from the surface incoming solar radiation (Norman, 1979). Simulated radiation-

391 dependent processes for the four layers are then scaled-up to two layers for in-canopy and canopy-top fluxes and concentrations using the

392 vertical LAI distribution.

393 MLC-CHEM diagnoses canopy-scale v_d from simulated canopy-top ozone fluxes divided by $[O_3]$, which is ambient ozone mixing

394 ratio at z_r [ppbv] (Table 1). Turbulent exchanges of ozone between the crown layer (subscript: cl) and understory (subscript: us)

395 and between the surface layer (subscript: sl) and crown layer are calculated from assumed linear $[O_3]$ gradients between heights,

396 and eddy diffusivities. The eddy diffusivity ($K_{sl \to cl}$) [m^2 s^{-1}] follows (Ganzeveld and Lelieveld, 1995):

397 $$K_{sl \to cl} = (z_{sl} - z_{cl})/r_a \quad (162)$$

398 The eddy diffusivity between the crown layer and understory ($K_{cl \to us}$) [m^2 s^{-1}] follows:

399 $$K_{cl \to us} = K_{sl \to cl} \, {}^{u_{cl \to us}}/u \quad (163)$$

400 The variable $u_{cl \to us}$ is wind speed at the crown layer-understory interface [m s^{-1}] calculated as a function of u and canopy structure

401 (Cionco, 1978).

402 Resistance to leaf-level uptake per layer ($r_{l,layer}$) follows:

403 $$r_{l,layer} = \frac{r_{b,leaf} + \left(\frac{1}{r_{st}} + \frac{1}{r_{cut}}\right)^{-1}}{\max\{LAI_{layer}, 10^{-5}\}} \quad (164)$$

404 The variable $r_{b,leaf}$ is the resistance to transport through the quasi-laminar boundary layer resistance around leaves (Table S3).

405 Leaf-level stomatal resistance (r_{st}) is calculated using a photosynthesis-stomatal conductance model (Ronda et al., 2001):

406 $$r_{st} = f(w_2) \, R_{diff,st} \left(\frac{D_w}{D_{CO_2}} \left(g_0 + g_1 \frac{A_n}{([CO_2] - \Gamma_*)\left(1 + 8.09\frac{VPD}{D_0}\right)} \frac{M_{air}}{1000 \, \rho}\right)\right)^{-1} \quad (165)$$

407 The ratio of diffusivities of water vapor to carbon dioxide is 1.6; g_0 is set to 0.025 x 10^{-3} m s^{-1} (Leuning, 1990); g_1 is set to 9.09;

408 A_n is net photosynthesis [μmol CO$_2$ m^{-2} s^{-1}], calculated as a function of G, leaf temperature, $[CO_2]$, and soil moisture (Ronda et

409 al., 2001); Γ_* is CO$_2$ compensation point [45 ppmv]; D_0 [kPa] is VPD at which stomata close (this term is calculated each timestep

410 from vegetation-specific constants; Ronda et al., 2001). The soil moisture effect follows:

$$f(w_2) = 2 \max\left\{\min\left\{10^{-3}, \frac{w_s - w_{wlt}}{0.75 w_{fc} - w_{wlt}}\right\}, 1\right\} - \left(\max\left\{\min\left\{10^{-3}, \frac{w_s - w_{wlt}}{0.75 \, w_{fc} - w_{wlt}}\right\}, 1\right\}\right)^2 \quad (166)$$

Leaf-level cuticular resistance (r_{cut}) follows (Wesely, 1989; Ganzeveld and Lelieveld, 1995; Ganzeveld et al., 1998):

$$r_{cut} = \left(\frac{1 - f_{wet}}{5 \, x \, 10^5} + \frac{f_{wet}}{1000}\right)^{-1} \quad (167)$$

In-canopy aerodynamic resistance (r_{ac}) considers turbulent transport through the understory to the ground:

$$r_{ac} = 14 \frac{0.25 \, h \, LAI}{u^*} \quad (168)$$

To estimate dry deposition to the ground, r_{ac} is added in series with r_g, which is the resistance to the ground [400 s m^{-1}] (Wesely, 1989; Ganzeveld and Lelieveld, 1995; Ganzeveld et al., 1998). If there is snow, then r_g is 2000 s m^{-1}. Resistances are combined with the lower most understory leaf resistance ($r_{l,layer,1}$) to create a lower most understory canopy resistance ($r_{c,layer,1}$):

$$r_{c,layer,1} = \left(\frac{1}{r_{l,layer,1}} + \frac{1}{r_{ac} + r_g}\right)^{-1} \quad (169)$$

In contrast to big-leaf schemes, effective conductances for MLC-CHEM do not add up exactly to v_d because there is an in-canopy $[O_3]$ gradient due to sources and sinks and transport.

4 Measurements for driving and evaluating single-point models

4.1 Turbulent fluxes of ozone

Our best observational constraints on dry deposition are turbulent fluxes, but fluxes integrate the influence of many processes and are not necessarily only reflective of dry deposition. For example, ambient chemical loss of ozone can influence ozone fluxes when the chemistry occurs on the timescale of turbulence. Relevant reactions for ozone fluxes are ozone reacting with highly reactive biogenic volatile organic compounds (BVOCs) or nitrogen oxide (NO). When there are no other sources and sinks aside from dry deposition below the measurement height, dividing the observed turbulent flux by ambient concentration at the same height can give a measure of efficiency of dry deposition ('the deposition velocity'). While fluxes provide key constraints on the amount of gas removed by the surface, deposition velocities aid in building predictive ability of dry deposition given that they indicate how the strength of the removal changes with meteorology and environmental conditions. Turbulent fluxes are mostly measured at individual sites, representing the 'ecosystem' scale where the measurement footprint typically extends from the order of 100 m to 1 km. Turbulent fluxes can also be measured from airplanes (e.g., Lenschow et al., 1981; Godowitch, 1990; Mahrt et al., 1995; Wolfe et al., 2015). Turbulent fluxes record changes on hourly or half hourly timescales, which is important because there is strong sub-daily variability in dry deposition.

Here we leverage existing long-term and short-term ozone flux datasets over a variety of LULC types to develop current understanding of model performance and the model spread. Strong observed interannual variability in ozone deposition velocities (Rannik et al., 2012; Clifton et al., 2017; Gerosa et al., 2022), as well as development of dry deposition schemes based on short-term data (e.g., days to months), motivates our emphasis on multiyear evaluation. Although our evaluation effort would ideally

include fluxes of many reactive gases (as well as aerosols), there are not long-term flux measurements of most compounds for which the fluxes primarily represent dry deposition. Generally, such flux observations are oftentimes few and far between and/or challenging to access (Guenther et al., 2011; Fares et al., 2018; Clifton et al., 2020a; Farmer et al., 2021; He et al., 2021). A key reason is that obtaining high-frequency concentration measurements of some compounds (e.g., NO_2, SO_2, HNO_3, H_2O_2) can be challenging due to the detection limits of fast response sensors, the demands of running research grade instruments in an eddy covariance configuration (e.g., consumables, dedicated staff, data storage), and potential flux divergences due to atmospheric chemical consumption or production on the same time scale as deposition processes (Ferrara et al., 2021; Fischer et al., 2021). Nonetheless, recent work further developing or creating new instruments for eddy covariance fluxes of black carbon, ozone, NO_2, ammonia, and a large suite of organic gases (Philips et al., 2013; Nguyen et al., 2015; Emerson et al., 2018; Fulgham et al., 2019; Novak et al., 2020; Hannun et al., 2020; Ramsay et al., 2018; Schobesberger et al., 2023; Vermeuel et al., 2023) demonstrates the potential for more widespread measurements that would assist in assessing the accuracy of dry deposition schemes more broadly.

Ozone fluxes are the most measured turbulent fluxes of any dry depositing reactive gas, and they can be measured over seasonal to multiyear timescales. We note that while the model evaluation component of Activity 2 is only for ozone, the model comparison component can be performed for other gases.

Ozone turbulent fluxes are measured either via eddy covariance or the gradient method. Eddy covariance is the most fundamental and direct method for measuring turbulent exchange (e.g., Hicks et al., 1989; Dabberdt et al., 1993). Eddy covariance fluxes require concentration analyzers with high measurement frequency to capture the transport of material via turbulent eddies. While fast analyzers are available for ozone, they are resource intensive to operate. Gradient techniques are more practical because slow analyzers can be used. However, gradient techniques assume transport only occurs down the local mean concentration gradient while in reality organized turbulent motions can transport material up-gradient (e.g., Raupach, 1979; Gao et al., 1989; Collineau and Brunet, 1993; Thomas and Foken, 2007; Steiner et al., 2011; Patton and Finnigan, 2013). We use some gradient ozone flux datasets, but caution that they may be particularly uncertain, especially for tall vegetation.

4.2 Site-specific datasets

We simulate ozone deposition velocities by driving single-point models with meteorological and environmental variables measured or inferred from measurements at eight sites. Table 2 summarizes site locations, LULC types, vegetation composition, and soil types. The set of sites represents a variety of LULC types and climates. The sites include deciduous, evergreen, and mixed forests, shrubs, grasses, and a peat bog. Climate types include Mediterranean, temperate, and boreal, as well as maritime and continental. Dry deposition parameterizations strongly rely on the concept that key processes and parameters are specific to LULC type. While we examine several LULC types here, we emphasize that our measurement testbed is likely insufficient to generalize the results of our study to specific LULC types, and thus we focus our discussion on individual sites. We also cannot discount the fact that differences in ozone flux methods and instrumentation and a lack of coordinated processing protocols across data sets limit meaningful synthesis of our results across sites. Table S17 summarizes details about ozone flux measurements, time periods

examined, and post-processing of data. Five of eight sites selected have at least three and up to twelve years of ozone flux data (Borden Forest, Easter Bush, Harvard Forest, Hyytiälä, Ispra). The rest have fewer than three years of ozone flux data (Auchencorth Moss, Bugacpuszta, Ramat Hanadiv) but were included to diversify climate and LULC types examined.

The eddy covariance technique is used for Auchencorth Moss, Bugacpuszta, Harvard Forest, Hyytiälä, Ispra, and Ramat Hanadiv. The gradient technique is used for Borden Forest and Easter Bush. The gradient technique used at Borden Forest is described in Wu et al. (2015, 2016) and was developed for Harvard Forest by comparing gradient and eddy covariance fluxes. Wu et al. (2015) shows that the gradient technique used at Borden Forest strongly overestimates ozone deposition velocities at night and during winter at Harvard Forest, as compared to the ozone deposition velocities calculated from the ozone eddy covariance flux measurements. Wu et al. (2015) also show that parameter choice can strongly influence deposition velocities inferred from the gradient technique. Thus, seasonal and diel cycle amplitudes as well as the magnitude of observed ozone deposition velocities at Borden Forest are uncertain.

Table 2: Summary of ozone flux tower sites.

Site	Location	Land use/land cover Type	More complete description of vegetation	Soil properties
Auchencorth Moss, Scotland	55.79ºN, 3.24ºW	Peat bog	Covered with heather, moss, and grass; vegetation primarily *Calluna vulgaris*, *Juncus effusus*, grassy hummocks, and hollows; drained and cut over 100 years ago but rewetted over many decades (Leith et al., 2014); low intensity grazing by sheep	85% Histosols
Borden Forest, Canada	44.32ºN, 79.93ºW	Temperate mixed forest	Boreal-temperate transition forest with mostly *Acer rubrum L.* but also *Pinus strobes L.*, *Populus grandidentata Michx.*, *Fraxinus americana L.,* and *Fagus grandifolia*; regrowing on farmland abandoned about a century ago (Froelich et al., 2015; Wu et al., 2016)	Tioga sand/sandy loam
Bugacpuszta, Hungary	46.69ºN, 19.60ºE	Grass	Semi-natural and semi-arid; primarily *Festuca pseudovina*, *Carex stenophylla*, and *Cynodon dactylon* (Koncz et al., 2014); grazing during most of the year (Machon et al., 2015)	Chernozem with 79% sand and 13% clay in upper soil layer (10 cm) (Horváth et al., 2018)
Easter Bush, Scotland	55.87ºN, 03.03ºW	Grass	On the boundary between two fields that have been managed for silage harvest and intensive grazing by sheep and cattle	Imperfectly drained Macmerry with Rowanhill soil association (Eutric Cambisol)

			(Coyle, 2006); greater than 90% *Lolium perenne* (Coyle, 2006; Jones et al., 2017)	and with 20-26% clay (Jones et al., 2017)
Ispra, Italy	45.81ºN, 8.63°E	Deciduous broadleaf forest	Grassland and meadowland prior to 1960s but has since regrown undisturbed; mainly *Quercus robur, Robinia pseudoacacia, Alnus glutinosa*, and *Pinus rigida* (Ferréa et al., 2012; Putaud et al., 2014); *Q. robur* (~80%) dominates except to the southeast of the flux tower where *A. glutinosa* dominates due to a higher water table	Mostly umbrisols with sandy-loam or loamy-sand texture for top 50 cm below which soil is mainly sandy (Ferréa et al., 2012)
Harvard Forest, USA	42.54ºN, 72.17ºW	Temperate mixed forest	Regrowing on farmland abandoned over 100 years ago; dominated by *Quercus rubra* and *Acer rubrum*, with scattered individual and patches of *Tsuga canadensis, Pinus resinosa*, and *Pinus strobus* particularly to the northwest of the tower where *T. canadensis* are most common (Munger and Wofsy, 2021)	Canton fine sandy loam, Scituate fine sandy loam, and hardwood peat swamp (Savage and Davidson, 2001)
Hyytiälä, Finland	61.85ºN, 24.29ºE	Evergreen needleleaf forest	Boreal forest; predominately *Pinus sylvestris*; shrubs underneath the canopy are *Vaccinium vitis-idaea* and *Vaccinium myrtillus*, and dense moss covers forest floor (Launiainen et al., 2013); *P. sylvestris* stand established in 1962 and thinned by 25% between January and March 2002 (Vesala et al., 2005)	Haplic podzol formed on glacial kill with 5-cm average organic layer thickness (Kolari et al., 2006)
Ramat Hanadiv, Israel	32.55ºN, 34.93°E	Shrub	Near eastern Mediterranean coast, mostly *Quercus calliprinos* and *Pistacia lentiscus*, but also include *Phillyrea latifolia, Cupressus, Sarcopoterium spinosum, Rhamnus lycioides*, and *Calicotome villosa*; west of the measurement tower are scattered *Pinus halepensis* (~5%) (Li et al., 2018)	Xerochrept (Li et al., 2018) and clay to silty clay (Kaplan, 1989)

520

522 For Activity 2, we selected sites without known influences of highly reactive BVOCs on ozone fluxes. However, there may be
523 unknown influences, especially at coniferous or mixed forests (Kurpius and Goldstein, 2003; Goldstein et al., 2004; Clifton et al.,
524 2019; Vermeuel et al., 2021), and generally the magnitude of the contribution and how it changes with time are uncertain (Wolfe
525 et al., 2011; Vermeuel et al., 2023). Most sites are expected to have very low NO. There may be some influences of NO on ozone
526 fluxes at Ramat Hanadiv (Li et al., 2018) and Ispra, but the magnitude and timing of the contribution is uncertain. Constraining
527 contributions of highly reactive BVOCs and NO to ozone fluxes is beyond the scope of our work here.

528

529 Removal of observed hourly or half-hourly ozone deposition velocity outliers for all sites leverages a univariate adjusted boxplot
530 approach following Hubert and Vandervieren (2008), which explicitly accounts for skewness in distributions and identifies the
531 most extreme ozone deposition velocities at each site. Non-Gaussian univariate distributions, or skewness, are present to some
532 degree in each observational dataset used here. This method designates the most extreme 0.7% of a normal unimodal distribution
533 as outliers, but the exact percentage depends on the degree of skewness. For datasets used here, which can be highly skewed, we
534 filter 1–6% of ozone deposition velocities across sites. Table S17 describes any other antecedent post-processing of ozone
535 deposition velocities performed for this effort.

536

537 Many dry deposition schemes include adjustments for snow. Table S18 identifies sites with snow depth (SD) measurements. Unless
538 the single-point model directly takes SD input to infer fractional snow coverage of the surface, we define the presence of snow as
539 SD greater than 1 cm. Models assume no snow if SD less than or equal to 1 cm or missing.

540

541 Canopy wetness is an input to several single-point models. Others do not ingest canopy wetness explicitly as an input variable, but
542 rather indicate canopy wetness using a precipitation and/or dew indicator. For the latter type, the fraction of canopy wetness (f_{wet})
543 from datasets is not used, and models' indicators are used. Table S18 details canopy wetness measurements at each site. For sites
544 where f_{wet} data are not available, f_{wet} values are approximated using an approach used in CMAQ (Table S18).

545

546 Soil moisture and soil properties and hydraulic variables are important for stomatal conductance as well as soil deposition processes
547 (Fares et al., 2014; Fumagalli et al., 2016; Stella et al., 2011, 2019). Site-specific details of variables used for near-surface and
548 root-zone volumetric soil water content are described in Table S19. A set of soil hydraulic properties (Table S20) are estimated for
549 each site from soil texture and used across models employing these parameters. For example, the variable B is an empirical
550 parameter, which is calculated as the slope of the water retention curve in log space (Cosby et al. 1984), that relates volumetric
551 soil water content to soil matric potential and can be referred to as a bulk hydraulic property of the soil (Clapp and Hornberger,
552 1978; Letts et al., 2000).

553

554 Overall, the core description for each site includes the key information needed to drive the single-point models: LULC type,
555 vegetation composition, soil type, and measurement height for ozone fluxes (Tables 2 and S17). We also describe inputs for snow,

558 canopy wetness, h, and LAI (Table S18). Outside of the core description, other meteorological variables are measured with standard

559 techniques, which are not discussed here. When an input variable is inferred, we detail assumptions involved in the inference

560 because variability in inferred input variables may not be accurately represented and this may need to be accounted for in comparing

561 simulated versus observed ozone deposition velocities (Tables S17 and S19).

562

563 We note that in addition to data screening conducted by data providers, driving datasets were visually inspected and clearly

564 erroneous values were set to missing (e.g., in one case T_a less than -50°C). Driving datasets are not gap-filled (unless explicitly

565 stated otherwise) so simulated ozone deposition velocities have gaps whenever one or more of a model's input variables is missing.

566 We emphasize that single-point models require different sets of input variables. Thus, output from different models may have

567 different data gaps at a given site. Additionally, because data capture for observed deposition velocities is based on availability of

568 ozone flux measurements, and data gaps in input variables may be different from data gaps in the ozone flux measurements,

569 simulated deposition velocities can have different data gaps from observed deposition velocities. We address data coverage

570 discrepancies across models and observed deposition velocities in two ways. First, we identify time-averaged observed and

571 simulated deposition velocities with suboptimal coverage in our results (e.g., see Figure 1). Second, we account for diel imbalances

572 in our analysis. Both approaches are described more fully in Section 4.3.

573 **4.3 Creation of monthly and seasonal average observed and simulated quantities**

574 We examine averages across 24 hours, except for Ramat Hanadiv. For Ramat Hanadiv, many months have missing values during

575 night and morning and thus we limit our analysis to 11am–5pm. Across sites and analyses, we use a weighted averaging approach

576 for daily averages that considers the number of observations for a given hour to avoid over-representation of any given hour due

577 to sampling imbalances across the diel cycle (e.g., more valid observations during daylit hours).

578

579 There are sometimes periods of missing ozone fluxes in the datasets. We indicate year-specific monthly averages with low data

580 capture for observed v_d on Figure 1. Low data capture is defined as less than or equal to 25% data capture averaged across 24

581 hours (or 11am–5pm for Ramat Hanadiv). In other words, we first compute data capture for each hour of a given month (or season),

582 and then average across hour-specific data capture rates to compare against the 25% threshold. We indicate multiyear monthly

583 averages with low data capture for observations and models on Figures 2 and 3. Note that the number of data points used in

584 constructing monthly averages differs between models and observations, and across models. Data capture for each model depends

585 on availability of the specific measured input data required for driving that model. Data capture for observed v_d is based on

586 availability of ozone flux measurements.

587

588 When we examine multiyear averages, we do not consider sampling biases across years (e.g., more valid observations in one year

589 over the other). Thus, more data for one year may skew multiyear averages towards values for that year (Fig. 1). However, results

590 are generally similar if we include weighting by years, except when there are only a few years contributing to multiyear averages,

591 and one or some of those years have low data coverage. For seasonal averages, months are not given equal weight unless stated

596 otherwise. For example, all non-missing data for a given hour across months of the season are considered equally (e.g., that there
597 may be more data at noon in July than August is not considered in a summertime average).

5 Results

599 Figure 1 shows monthly mean observed ozone deposition velocities (v_d) across years, as well as multiyear averages, at all sites.
600 There are a variety of seasonal patterns and magnitudes of observed v_d across sites. Interannual variability is strong in terms of the
601 standard deviation across yearly annual averages normalized by the multiyear average (range of 10% to 60% across sites). In some
602 cases, periods with low data coverage contribute to apparent interannual variability and/or seasonality, and thus in these cases the
603 degree of interannual variability is uncertain. However, more complete ozone flux records also show strong variability from year
604 to year and month to month, suggesting that we can expect strong interannual variability on a monthly basis to be a generally
605 robust feature of the observations. The following discussion focuses on multiyear averages, but we briefly examine summertime
606 (June-August) interannual variability at sites with three or more years of data in the individual site subsections below to establish
607 whether models capture the range of interannual variability and/or ranking among different summers.

609 Figure 2 shows multiyear monthly mean v_d from observations and the spread in multiyear monthly mean v_d across models,
610 whereas Figure 3 shows multiyear monthly mean values from each individual model and the observations. The minimum and
611 maximum of the monthly averages across the models bracket the observations across most sites and sites (Fig. 2). The exceptions are
612 Auchencorth Moss (all months except July), Borden Forest (October-November only), and Ispra (October-February only). In some cases,
613 model outliers allow the full set of models to bracket observations (Fig. 3), which suggests limited skill of the model ensemble. If we instead
614 consider the interquartile range across models (hereinafter, 'the central models'), then there are at least a few months at every site when
615 observations fall out of range. At the same time, at every site except Auchencorth Moss, there are also at least a few months when the
616 observations are within the range, indicating that failure of the central models to capture observations consistently across the seasonal cycle
617 does not suggest a complete lack of skill from the model ensemble that de-emphasizes outliers. Further, the central models are very close
618 to bracketing observations across months at Easter Bush, Hyytiälä, and Harvard Forest.
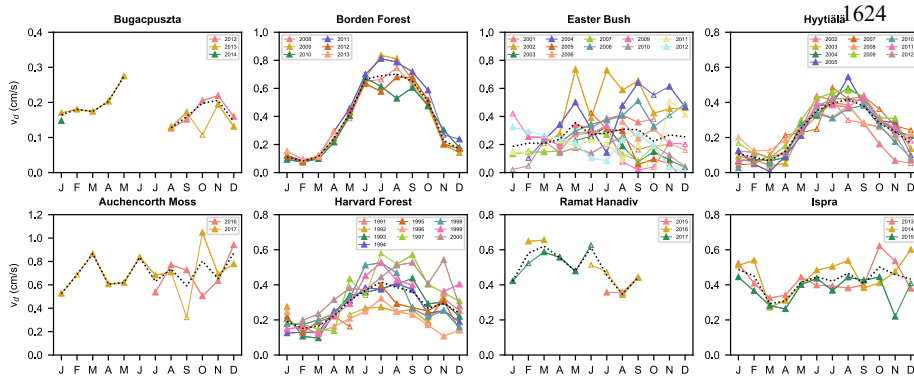
Figure 1 Monthly mean ozone deposition velocities (v_d) from the ozone flux observations. Multiyear average is in black. Different years are in colors. Open symbols indicate months for a given year with low data capture.

The model spread in multiyear mean v_d across months and sites is large (Fig. 2). The spread in terms of the model with the highest annual average divided by the model with the lowest ranges from a factor of 1.8 to 2.3 except Hyytiälä (2.7) and Auchencorth Moss (5). The spread in wintertime (December-February) averages is very high at some sites: Borden (10), Hyytiälä (21), Auchencorth Moss (9.1), and Harvard Forest (6.3). The spread in wintertime averages is a factor of 2 to 3.3 at other sites. The spread is typically lower during summer (June-August) than winter, on par with annual values. We also use the 75th percentile divided by the 25th percentile as a metric of the spread. This metric for the annual average is a factor of 1.2–1.8. For winter, the metric is also lower for sites with high spreads based on all models (a factor of 3 for Borden Forest, 2.4 for Hyytiälä, 3 for Auchencorth Moss, and 2.7 for Harvard Forest), but still higher than the summer and annual spreads (except Ispra).
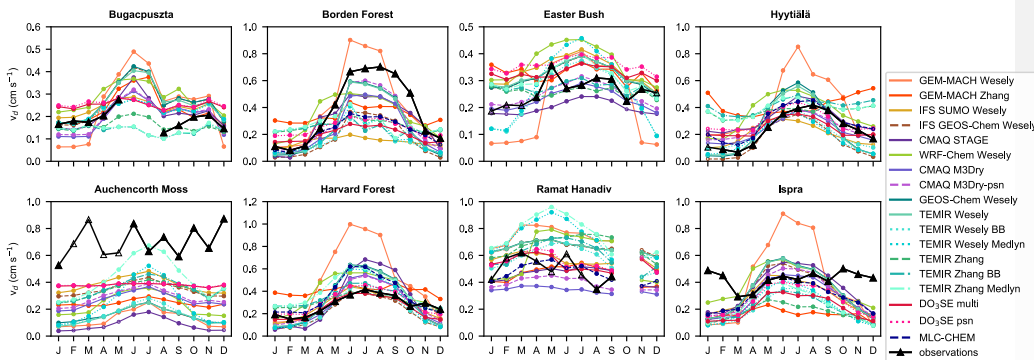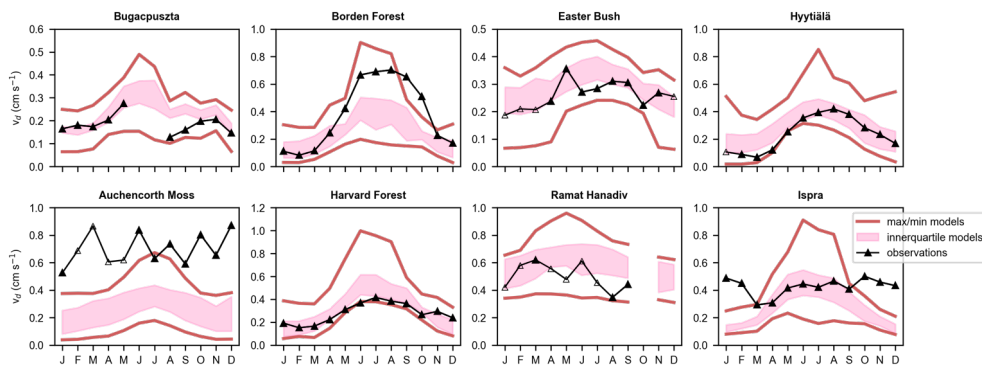
Figure 2 Multiyear monthly mean ozone deposition velocities (v_d) from ozone flux observations and single-point models. Pink shading denotes the interquartile range across models. Red lines denote the minimum and maximum across monthly simulated values. Open symbols on observations indicate months with low data capture.

Figure 4 shows the relative biases (simulated minus observed divided by observed) across months, sites, and seasons. When we consider individual model performance, then we find that no model is always within 50% of observed multiyear averages across sites and seasons (Fig. 4). Models are very low against observations at Auchencorth Moss, but the previous statement holds even excluding this site. In general, a key finding here is that model performance varies strongly by model, season, and site. Below, we first discuss mean absolute biases across sites, and then drivers of seasonality across models and sites. Then, in the subsections, we discuss each site, starting with short vegetation, and then forests.

The absolute bias (simulated minus observed) averaged across multiyear seasonal averages and sites is highest for GEM-MACH Wesely (0.22 cm s^{-1}) and lowest for CMAQ M3Dry-psn (0.12 cm s^{-1}) (Fig. 4). GEM-MACH Zhang, WRF-Chem Wesely, GEOS-Chem Wesely, TEMIR Wesely, TEMIR Wesely BB, and TEMIR Wesely Medlyn are on the higher end of the spread in mean absolute bias across seasons and sites (0.17–0.18 cm s^{-1}), while DO$_3$SE multi, DO$_3$SE psn, and IFS SUMO Wesely (0.13 cm s^{-1}) and CMAQ M3Dry (0.14 cm s^{-1}) are on the lower end, with the rest in between (0.15–0.16 cm s^{-1}). (MLC-CHEM does not simulate

Figure 3 Multiyear monthly mean ozone deposition velocities (v_d) from ozone flux observations and single-point models. Open symbols indicate months with low data capture.

three sites so we exclude it here).

The absolute biases averaged across seasons may overemphasize model performance when v_d are high. Given that wintertime v_d tends to be lower in magnitude than during other seasons, we also examine wintertime mean absolute biases across sites (Fig. 4). Values are highest for GEM-MACH Zhang (0.22 cm s^{-1}), GEM-MACH Wesely (0.20 cm s^{-1}), TEMIR Wesely (0.20 cm s^{-1}), and TEMIR Wesely Medlyn (0.19 cm s^{-1}). Otherwise, model biases are below 0.16 cm s^{-1}.

669

670   Figure 5 shows simulated multiyear wintertime and summertime mean effective conductances, as well as the observed multiyear seasonal

671   average v_d (recall that simulated effective conductances sum to simulated v_d). The three main pathways are stomata, cuticles, and soil;

672   even when models simulate lower canopy uptake, uptake via this pathway tends to be low. We thus focus on stomatal, cuticular, and soil

673   pathways. There are three important takeaways from Figure 5. First, models can disagree in terms of relative contributions from

674   pathways, even when they predict similar v_d. Conversely, models can agree in terms of relative contributions of pathways but

675   predict different v_d. Second, stomatal and nonstomatal pathways both have important contributions to v_d across models, and are

676   both key drivers of variability across models. Third, models tend to disagree on cuticular versus soil contributions to nonstomatal uptake

677   at some sites, while agreeing at others.

678

679   Figure 6 shows how multiyear mean seasonality of effective conductances contributes to the multiyear mean seasonality of simulated v_d

680   across models. Specifically, the variance in each pathway across months is shown, as well as twice the covariance between individual

681   pathways. Negative covariances imply offsetting seasonality between the two pathways (i.e., an anticorrelation in seasonal cycles of two

682   pathways, and this acts to dampen the total seasonality). Positive covariances mean that a positive correlation in seasonal cycles of the two

683   pathways acts to amplify total seasonality. Values are normalized by the absolute sum of the variance and twice the covariances so that

684   Figure 6 does not emphasize differences in the seasonal amplitude, rather what pathways control the seasonality.

685

686   The key finding from Figure 6 is that stomatal uptake is the most important driver of multiyear mean v_d seasonality for most models and

687   sites. For some models and sites, cuticular uptake also plays a role, albeit mostly just via correlations with stomatal uptake. Correlations

688   between stomatal and cuticular pathways are mostly positive, and thus tend to amplify v_d seasonality. Exceptions are Hyytiälä and Easter

689   Bush where some models show anticorrelations between stomatal and cuticular uptake seasonal cycles. With a few exceptions (e.g., at

690   Easter Bush and for GEM-MACH Wesely and DO₃SE models), soil uptake tends to play a more minor role.

691

692   In general, the parameters and dependencies driving simulated v_d seasonality are model dependent. Expected dominant influences include

693   changes in initial resistances with season, cuticular and stomatal dependencies on LAI, stomatal dependencies on soil moisture,

694   temperature response functions (used in Wesely (1989) to decrease nonstomatal deposition pathways at cold temperatures), and

695   changes with snow.

696

697   Figure 7 shows how multiyear monthly mean v_d changes with LAI, for both the models and the observations. Multiyear monthly mean

698   observed and simulated v_d generally increases with LAI across sites during at least some time periods of plant growth (Fig. 7). In general,

699   however, the relationship between v_d and LAI on monthly timescales is nonlinear for both observations and models, distinct between

700   observations versus models, and distinct across models. Many models show a strong sensitivity to LAI, which has been pointed out in

701   previous work (Cooter and Schwede, 2000; Charusombat et al., 2010; Schwede et al., 2011; Silva and Heald, 2018). Our analysis

708 here, combined with past work, suggests that advancing predictive ability requires better understanding of observed v_d-LAI
709 relationships in terms of seasonality and site-to-site differences.

710

711 Figure 8 shows snow's impact on multiyear mean v_d at sites with snow depth records and sufficient snowy periods. Observations suggest
712 modest reductions with snow at Bugacpuszta and Hyytiälä, but not much change at Borden Forest. At Borden Forest, some models show
713 decreases, while others show little change. At Hyytiälä and Bugacpuszta, some models capture decreases with snow despite biases whereas
714 other models understate or exaggerate decreases. Observed reductions with snow are larger at Bugacpuszta than Hyytiälä, and many
715 models capture this. Findings with respect to Borden Forest may reflect that snow is not measured there, rather 15 km away, and thus this
716 not reflect exact local conditions. Even though some models do not capture the magnitude of observed v_d decreases with snow, Figure 8
717 shows that models' inability to capture the magnitude of wintertime values (snow or snow-free) at a given site is a much larger problem
718 than models' inability to capturing responses to snow, at least at these three sites. The relative model spread (based on the standard deviation
719 across models divided by the average) does not change substantially under snowy versus all conditions, except at Bugacpuszta (27% versus
720 70%), further underscoring the need to better understand wintertime v_d in a more general sense.

721

722 The relatively low magnitude of snow-induced observed v_d changes indicates that snow-induced changes are not the main driver of
723 observed v_d seasonality (Fig. 8). For example, observed changes with snow are a small fraction of the observed absolute seasonal amplitude
724 of multiyear monthly averages at these sites, at least for Hyytiälä and Borden Forest. We also note that models simulate v_d reductions with
725 snow at Hyytiälä and Bugacpuszta even when snow is not model input, suggesting that other model dependencies (e.g., temperature
726 response functions) may lead to changes coincident with snow. Recent papers suggest that better snow cover representation may be key for
727 capturing v_d spatial variability at regional scales and regional average seasonal cycles as well as changes with climate change (Helmig et
728 al., 2007; Andersson and Engardt, 2010; Matichuk et al., 2017; Clifton et al., 2020b). Despite insufficient data to examine spatial variability
729 or responses to climate change, our analysis suggests drivers of wintertime v_d other than snow are important to understand.
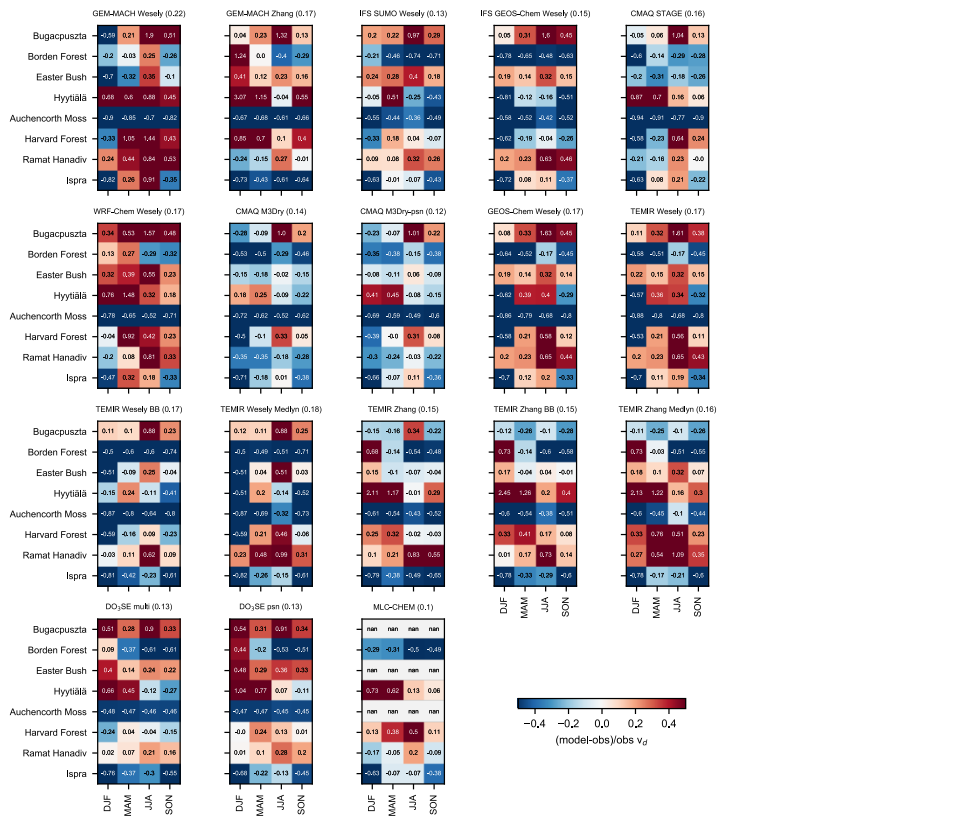
Figure 4 Seasonal mean relative biases (simulated minus observed divided by observed) across models, and sites, for ozone deposition velocities (v_d), expressed in fractions. Numbers next to model names in the subpanel titles are seasonal mean absolute biases in cm s^{-1}. DJF is December, January, and February. MAM is March, April, and May. JJA is June, July, and August. SON is September, October, and November.

749
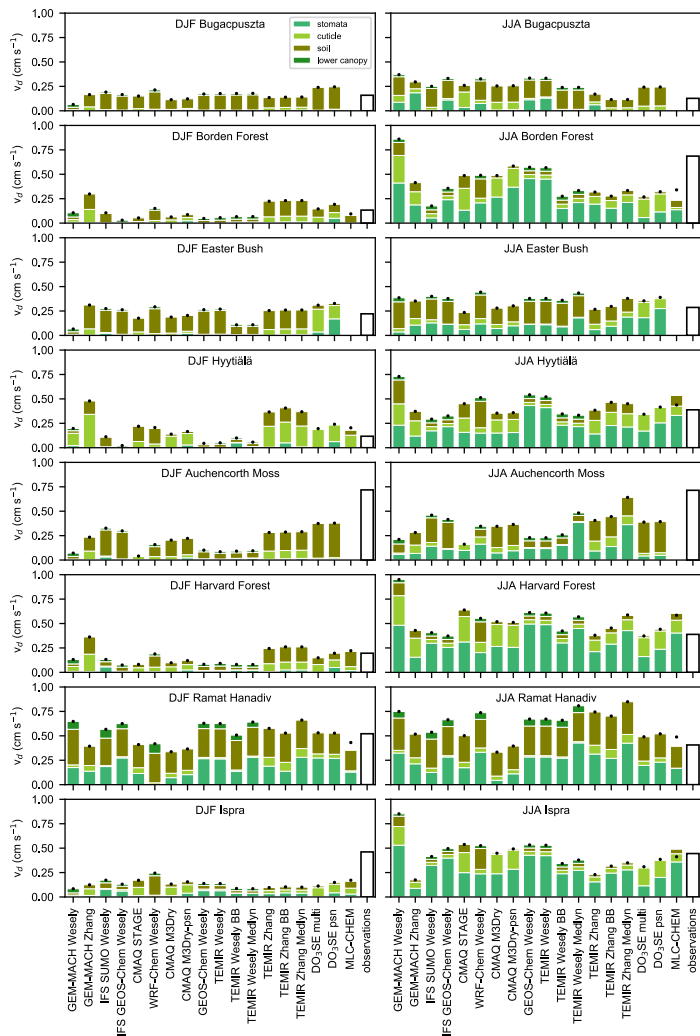
750 Figure 5 Multiyear seasonal mean simulated effective conductances and observed ozone deposition velocities (v_d). Black dots are
751 simulated v_d (black dots should equal the top of the bars). DJF is December, January, and February. JJA is June, July, and August.

753
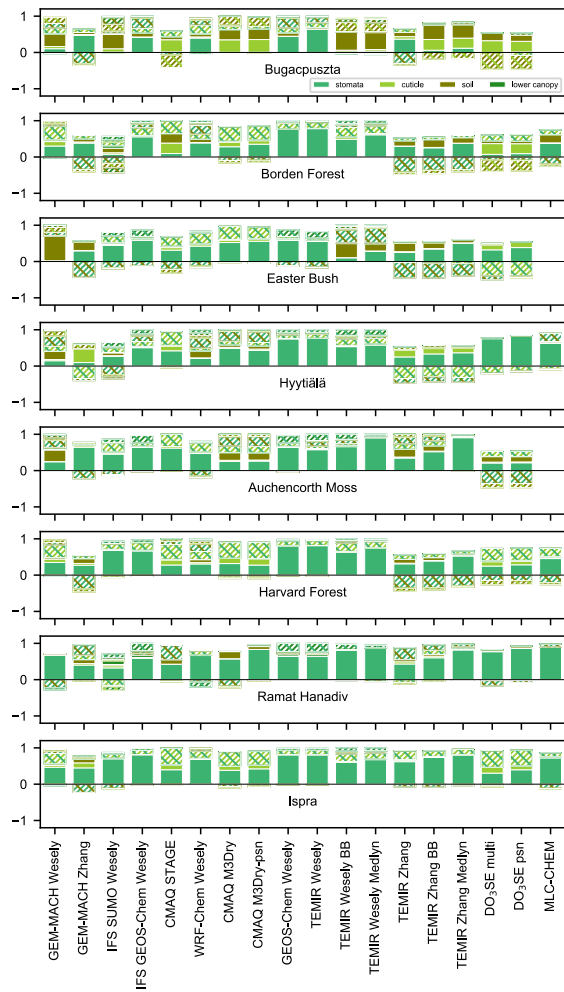
754 Figure 6 Pathways contributing to variability across simulated multiyear monthly mean ozone deposition velocities. The variance
755 for each effective conductance is a solid color. Twice the covariance between effective conductances is a hatched pattern (the
756 colors of hatch correspond to pathways examined). Each value is normalized by the absolute value of the sum of the variances and
757 twice the covariances so that we are comparing the pathways that drive seasonality across models in a relative sense (rather than
758 the seasonal amplitude as well).
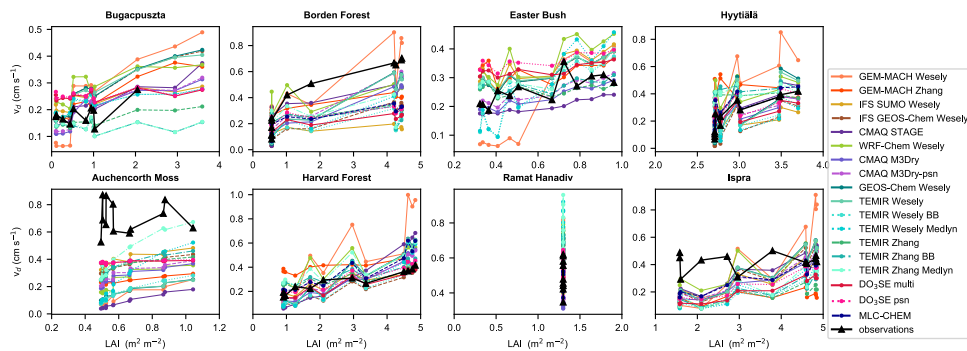
Figure 7 Multiyear monthly mean ozone deposition velocities (v_d) versus leaf area index (*LAI*).

5.1 Bugacpuszta

Bugacpuszta is a semi-arid and semi-natural grassland with grazing during most of the year in Hungary. In terms of variability across models, the model spread based on the model with the highest annual average v_d divided by the model with the lowest is a factor of 2.1 (2.8 during summer and 2.2 during winter) but based on the interquartile range is a factor of 1.3 (1.2 during summer and 1.3 during winter). This model spread at Bugacpuszta is on the lower end of the estimates across sites examined.

A longer ozone flux record data is needed to assess interannual variability at Bugacpuszta. Bugacpuszta has only a single year of data during February–May (from 2013), two years of data during August–December (from 2012 and 2013), and two years of data during January (from 2013 and 2014) (Fig. 1). Data are always missing during June and July. For time periods with two years of data, observed monthly mean v_d values are very close in magnitude between years. The exception is October when 2013 values are half of the 2012 values. However, October 2013 has very low data coverage (only ~2–3 days of coverage), and hourly values exhibit high uncertainty compared to other months (not shown). We thus focus below on the 'multiyear averages' at this site, acknowledging that there are only two years of data during six months of the year (and ten months total with data).

Without June and July observations, we cannot fully assess seasonality at Bugacpuszta. So, we evaluate seasonality across other months. The observed seasonal cycle for the months with data is as follows: v_d maximizes during May, following an increase from March, and minimizes during August, after which v_d increases to November and levels off from December–February (Fig. 1). Seasonal patterns are similar across many models, with mid-summer peaks after slow increases from winter and similar values from August–November (Fig. 3). Despite similar seasonal patterns across the models as well as fair agreement in the relative seasonal amplitude across the models (Fig. 9), the models disagree with respect to pathways dominating the seasonal cycle (Fig. 6). Notably, models disagree the most in terms of pathway(s) driving seasonality at Bugacpuszta relative to other sites, suggesting that changes in individual pathways on seasonal timescales at this location may be a key uncertainty.
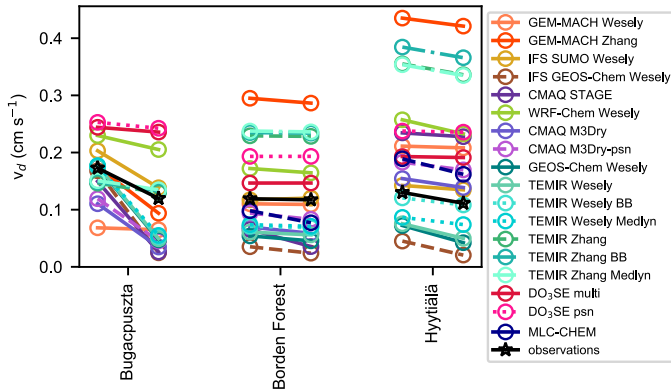
Figure 8 Multiyear mean ozone deposition velocity (v_d) during all conditions versus when snow depth greater than or equal to 1 cm for sites with snow depth records and sufficient time with snow (25% averaged across hours per month). Months considered are December-February for Bugacpuszta, December-February for Borden Forest, and November-March for Hyytiälä. Months are given equal weight in averages.

The central models bracket observed v_d at Bugacpuszta during December–May but are too high against the observations during August and September (and only slightly too high during October and November) (Fig. 2). Two clear model outliers during warm months are TEMIR Zhang models (Fig. 3), which show relatively low soil and cuticular uptake (Fig. 5). TEMIR psn also shows no stomatal uptake, following very low input root-zone soil moisture (below prescribed wilting point). At the same time as TEMIR Zhang models are clear model outliers during warm months, they allow the complete set of models to bracket observations during August-November, because the other models are mostly too high (or in a few cases just right). Without June and July ozone fluxes, however, it is unclear how TEMIR Zhang models alter the summertime performance of the model spread.

Only eight models show substantial summertime stomatal uptake at Bugacpuszta (Fig. 5). There is no summertime stomatal uptake simulated by TEMIR psn, IFS SUMO Wesely, and DO₃SE models, and very little by CMAQ STAGE, CMAQ M3Dry and CMAQ M3Dry-psn. Only these models employ soil moisture dependencies on stomatal conductance (MLC-CHEM does as well but does not simulate values at Bugacpuszta); these models simulate little-to-no stomatal uptake at Bugacpuszta because input soil moisture is below prescribed wilting point. We emphasize that wilting point, which is not a directly measurable quantity, is uncertain across sites. If we instead focus on the models with the models with substantial summertime stomatal uptake, then we can see that they show a large spread in the stomatal fraction of v_d – from 12.5% to 40% with one model simulating 60% (Fig. 12) – and produce distinct stomatal uptake seasonal cycles (Fig. 10). On the other hand, many models show similar v_d seasonal cycle shapes (Fig. 3)

but dissimilar stomatal uptake seasonal cycle shapes. These results suggest that nonstomatal uptake seasonality plays a role in normalizing differences in v_d seasonal cycles across models, and the models are more distinct than implied by v_d alone.

Bugacpuszta has the most similar summertime model spreads across the top three deposition pathways relative to other sites (except Hyytiälä) (Fig. 11), suggesting a high degree of uncertainty in the magnitude of all pathways during warm months. Most models show substantial summertime contributions from soil uptake, but the magnitude of soil uptake varies across models (Fig. 5). In contrast, for summertime cuticular and stomatal pathways, models disagree as to whether contributions are substantial in addition to disagreeing on the magnitude of uptake. For example, like how some models show very low stomatal uptake (as discussed above), some models show negligible cuticular uptake. Establishing whether there should be summertime stomatal and/or cuticular uptake at Bugacpuszta would be a first step towards further constraining models.

Multiyear monthly mean LAI at Bugacpuszta shows a sharp summer peak, maximizing during June (~3.6 m^2 m^{-2}) (Fig. 10). Values are similar during August to November, and then decrease from November to March, with a minimum during March. Observed v_d is missing for LAI greater than 2 m^2 m^{-2} (corresponding to June and July). There is no discernable observed v_d-LAI relationship for LAI below 1 m^2 m^{-2}, and models capture this (Fig. 7). Observations show a strong v_d increase from 1 to 2 m^2 m^{-2}. Models show an increase, but most do not capture the large observed slope. This is especially true for models with soil moisture dependencies on stomatal conductance, implying that during at least some periods of high vegetation density, there should not be soil moisture stress, or as strong of soil moisture stress as simulated by some models.

Models simulate that soil uptake dominates wintertime v_d at Bugacpuszta (Fig. 5). The exception is GEM-MACH Wesely, which underestimates wintertime v_d. Wintertime stomatal fractions of v_d can be up to 10% (due to low v_d overall) but are mostly within 0–5%. Because the central models capture wintertime v_d (Fig. 2), and models agree that soil uptake dominates, some models may have some skill during cooler months. There is variability in soil uptake across models (Fig. 11), however. Models largely capture observed wintertime v_d decreases with snow, with most slightly overestimating the change but a few (DO₃SE models, WRF-Chem Wesely, TEMIR Zhang, GEM-MACH Wesely) underestimating it (Fig. 8). Future attention to the non-central models should focus on better capturing wintertime nonstomatal uptake generally at this site, rather than changes with snow.

A key outstanding question at Bugacpuszta is: should models simulate low stomatal uptake throughout summer, or only during late summer? Most models are too high against observations during August and September. This includes models employing soil moisture dependencies on stomatal conductance (and thus simulate very-low-to-no stomatal uptake), implying too-high simulated nonstomatal uptake. Continuous year-round ozone flux observations, especially during periods of the growing season with and without moisture stress, are needed to better assess model performance at Bugacpuszta. Independent measures of stomatal conductance during periods of missing ozone fluxes would be useful in constraining the absolute stomatal portion of dry deposition,

Deleted: , suggesting

Formatted: Condensed by 0.25 pt

Deleted: for

Deleted: as compared

Deleted: decreases

Formatted: Condensed by 0.25 pt

Deleted: at Bugacpuszta.

Deleted: ,

863 but further constraining nonstomatal uptake, which models indicate is an important fraction of summertime v_d (despite disagreeing

864 on the exact pathway), requires additional ozone flux measurements.

865
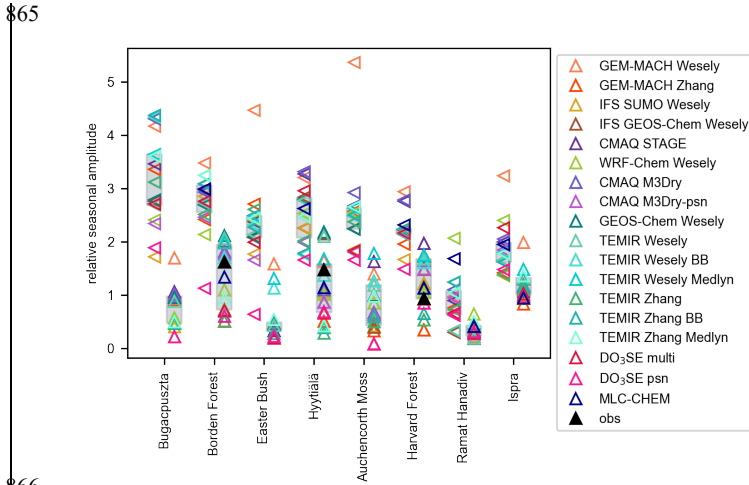
867 Figure 9 Relative seasonal amplitudes of multiyear monthly mean stomatal uptake (sideways triangles) and ozone deposition
868 velocities (upwards triangles) across models, defined as the maximum across months of multiyear monthly averages minus the
869 minimum, divided by the average. Black triangles denote the relative seasonal amplitude of observations for sites with wintertime
870 minima and summertime maxima. Grey shading denotes the interquartile range across models.

5.2 Auchencorth Moss

872 Auchencorth Moss is a peat bog covered with heather, moss, and grass in Scotland. The model spread in terms of the model with the

873 highest annual average v_d divided by the model with the lowest is a factor of 5 (4.3 during summer and 9.1 during winter) but based

874 on the interquartile range is a factor of 1.6 (1.5 during summer and 3 during winter). Across sites, for the annual metrics,

875 Auchencorth Moss has the largest spread for the maximum/minimum metric and the second largest for the interquartile range.

877 There is no clear shape of the observed v_d seasonal cycle at Auchencorth Moss (Fig. 1). Whether this is true on a climatological

878 basis is unclear due to 1) data incompleteness during the two-year period – observed values during February–May have low data

879 capture mostly because data are missing during 2016 – and 2) strong interannual variability when there are data, and 3) the fact

880 that there are only two years of data. A longer and more complete ozone flux record is needed to fully assess interannual variability

881 as well as seasonality at Auchencorth Moss. Below, we focus on 'multiyear averages', acknowledging that only half the months

882 of the year have two years of data.

883

890 A key finding is that models do not capture the high values of v_d that are observed year-round at Auchencorth Moss (Fig. 2). The
891 exception is TEMIR Zhang Medlyn during July. Auchencorth Moss is the only site examined with negative biases (> 30% of
892 observed multiyear seasonal averages) across seasons and models (except for TEMIR Zhang Medlyn during July) (Fig. 4). Biases
893 tend to be smallest during summer and largest during winter because many models simulate peak v_d during warm months (Fig. 3).
894 Notably, models differ substantially in their relative seasonal amplitudes, with a very even and wide distribution in relative seasonal
895 amplitude across models (Fig. 9), especially relative to other short vegetation sites.
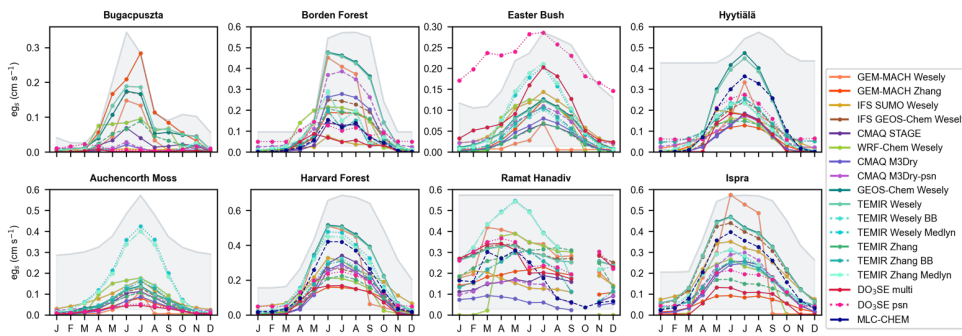
896
897 Figure 10 Multiyear monthly mean effective stomatal conductance (eg_s) from single-point models. Grey shading denotes multiyear
898 monthly mean leaf area index (used to emphasize seasonality in this variable; y-ranges not given).

899 Simulated v_d seasonality is mostly due to stomatal uptake (Fig. 6). Some models show that soil uptake plays a role, and all but two
900 models show moderate contributions from correlations between pathways. The seasonality shape of stomatal uptake is very similar
901 across most models, as well as the magnitude of stomatal uptake throughout the year (Fig. 10). Major exceptions are TEMIR
902 Medlyn models, which show peak values around 0.4 cm s^{-1} in contrast to the rest that average just under 0.1 cm s^{-1}. For the relative
903 seasonal amplitudes in stomatal uptake, the spread across the central models is low (Fig. 9). The value for GEM-MACH Wesely
904 is very high (> 5), with other models' values spanning a factor of 1.75 to 3. Models deviating from the rest with respect to stomatal
905 uptake's seasonality shape are GEM-MACH Zhang (near-zero during August and after; strong peak during July) and DO$_3$SE (low
906 during summer) as well as WRF-Chem Wesely and IFS SUMO Wesely (the latter two are similar and higher than others especially
907 during spring).

908

909 While high summertime stomatal uptake combined with moderately high year-round nonstomatal uptake distinguishes TEMIR
910 Zhang Medlyn from others (Fig. 5), we see the best agreement between this model and observations during warm months. However,
911 TEMIR Zhang Medlyn does not capture observed seasonality (or lack thereof). Thus, TEMIR Zhang Medlyn may have more skill during
912 summer than other models, but like other models, TEMIR Zhang Medlyn struggles with seasonality. Future work should establish whether
913 there is strong seasonality in stomatal uptake coupled with offsetting seasonality in nonstomatal uptake at Auchencorth Moss, or whether
914 stomatal uptake should be higher year-round.
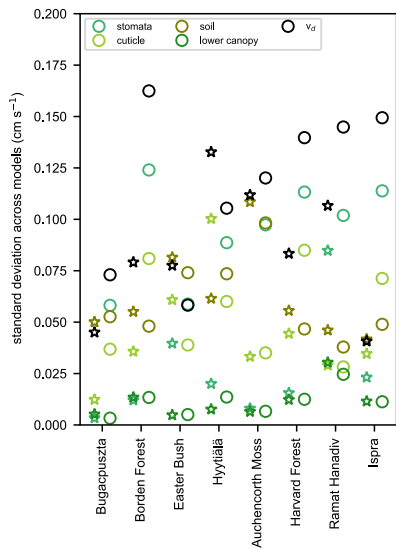
Figure 11 Model spread (standard deviation) across multiyear seasonal mean ozone deposition velocities (v_d) and effective conductances for DJF (stars) and JJA (circles). DJF is December, January, and February. JJA is June, July, and August.

For soil uptake, the model spread is large and similar between summer and winter (Fig. 11). During summer, the spread in stomatal uptake is on par with soil uptake; spreads for stomatal and soil uptake are the highest across pathways. During winter, the spread in stomatal uptake is very low, and the spread in soil uptake is the highest. Wintertime stomatal fractions vary from 0% to 20% across models (Fig. 12). Models except CMAQ STAGE simulate nonnegligible soil uptake (Fig. 5). However, during summer, models disagree on the soil contribution to v_d (0–80%) as well as the magnitude of soil uptake. In contrast, during winter, models agree that soil uptake contributes substantially to v_d (>60%) (apart from CMAQ STAGE and GEM-MACH Wesely) but disagree on the magnitude of soil uptake. Snow depth is measured at Auchencorth Moss, but data are missing during half of the ozone flux period, and there is not a substantial amount of time with snow when there are measurements.

Models estimate very-low-to-moderate cuticular uptake at Auchencorth Moss (Fig. 5), which is consistent across low vegetation sites. Moderate values of cuticular uptake are simulated by GEM-MACH Zhang and TEMIR Zhang models, and values are similar between summer and winter. Otherwise, models simulate very little cuticular uptake during winter and low cuticular uptake during summer. Nonetheless, the model spread in cuticular uptake is similar between seasons. Summertime stomatal fractions vary across the central models from 25% to 55% (Fig. 12). Aside from one model simulating 80% and two models around 10%, half are around 20–30% and the other half are around 45–60%. There is a clear division across models in that no model simulates stomatal fractions

947   between 32.5% and 45%. The dichotomy seems to be due to variability in both stomatal and soil uptake across models, consistent

948   with high summertime model spreads for these pathways (Fig. 11).

949
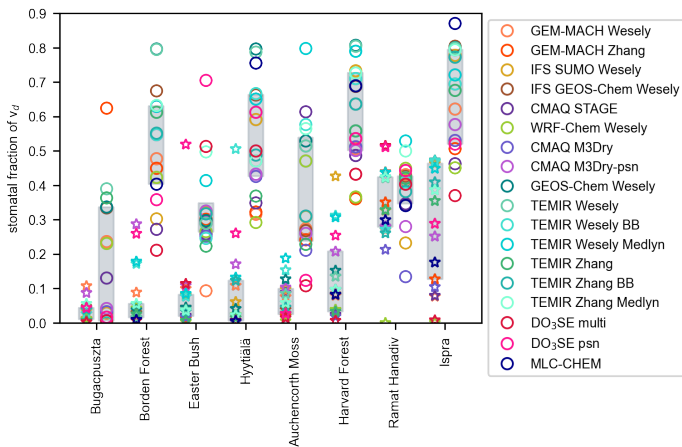
950

951   Figure 12 Multiyear seasonal mean stomatal fraction of ozone deposition velocities (v_d) across models during DJF (stars) and JJA

952   (circles). Grey shading denotes the interquartile range across models. DJF is December, January, and February. JJA is June, July,

953   and August.

954   Despite an unclear observed v_d seasonal pattern at Auchencorth Moss, the relationship between monthly mean *LAI* and v_d may

955   provide insights into model performance. With strong observed v_d variations at low *LAI* (less than 0.6 m^2 m^{-2}), there is no

956   relationship, but there is a positive relationship at moderate *LAI* (in the range of 0.6 to 0.9 m^2 m^{-2}) (Fig. 7). Observations then show

957   that v_d decreases with *LAI* increases above 0.8 m^2 m^{-2} but there is only one data point here. Most models seem to capture the observed

958   relationship at moderate *LAI* as well as that there should not be a relationship at low *LAI*. Some models (e.g., TEMIR models)

959   overestimate the increase's slope at moderate *LAI*, though. Thus, some models may have some skill at simulating seasonality in cuticular

960   and/or stomatal uptake. Nonetheless, strong observed v_d variability at low *LAI* and changes with *LAI* during peak vegetation density need

961   better understanding. With observational constraints on stomatal uptake, we will be able to understand whether nonstomatal uptake should

962   be higher year-round and/or seasonality in nonstomatal uptake should act to offset seasonality in stomatal uptake.

963

964   We close by emphasizing that very high observed v_d at Auchencorth Moss are uncertain – there is strong interannual and day-to-day

965   variability, but a lot of missing data. The peat/bog LULC type does not have many ozone flux measurements at other sites that could

966   be used to provide additional context to Auchencorth Moss measurements. Schaller et al. (2022) show that v_d ranges from 0.05

967   cm s^{-1} at night to 0.45 cm s^{-1} during the day in July 2017 at a peatland in NW Germany. El Madany et al. (2017) look at ozone

fluxes at the same site during 2014 but do not present v_d values. Fowler et al. (2001) present older measurements at Auchencorth Moss, estimated with the gradient technique (eddy covariance is used for the data examined here), showing much lower observed v_d than examined here (e.g., winter and fall values here are twice what they are during 1995-1998, summer are almost twice, and spring are higher but not twice). It is not clear what drives the higher, more recent v_d measurements at Auchencorth Moss analyzed in this study and more detailed analysis is needed to figure it out. In general, building understanding of ozone dry deposition at this LULC type provides a key test of understanding of soil uptake, and its dependence on its expected drivers (soil organic carbon and water content), given peat/bog soils are organic rich and wet.

5.3 Easter Bush

Easter Bush is a managed grassland used for silage harvest and intensive grazing in Scotland. In terms of variability across models, the spread based on the model with the highest annual average v_d divided by the model with the lowest is a factor of 1.8 (1.8 during summer and 3.0 during winter) but based on the interquartile range is a factor of 1.3 (1.3 during summer and 1.4 during winter). Model spreads at Easter Bush are some of the lowest compared to other sites.

Easter Bush has one of the longest ozone flux records (Clifton et al., 2020a), and the longest record examined here as well as strongest interannual variability. For example, the coefficient of variation across years is on average 60% across months. In contrast, other sites show coefficients of variations across years from 10% to 30%. There is also strong interannual variability in the observed seasonal cycle's shape at Easter Bush (Fig. 1). As for other sites with long term records, we focus on multiyear averages but touch on summertime interannual variability. Some models capture some low summers, but models do not capture high summers (except GEOS-Chem Wesely, IFS GEOS-Chem Wesely, and TEMIR Wesely, which capture one high year) and underestimate interannual spread (Fig. 13). Future work should focus on understanding observed interannual variability, and consider that interannual variability changes strongly by month, both in terms of the spread across years and ranking of years.

The central models' spread largely brackets observed multiyear monthly values across months. Specifically, observed values sit mostly on the lower end of or just below the central models' spread, except during May, November, and December when observed values are on the higher end (Fig. 2). Only CMAQ STAGE consistently shows lower v_d than observed, but the relative bias is low (-18% to -30%) (Fig. 4). During winter, GEM-MACH Wesely and TEMIR Wesely psn are too low, and the relative biases are substantial (-51% to -70%). With a few exceptions (i.e., winter for GEM-MACH Wesely and TEMIR Wesely psn, summer for WRF-Chem Wesely and TEMIR Wesely Medlyn), models are within $\pm 50\%$ of observed seasonal averages.

Overall, the below suggests that models may have skill at simulating climatological v_d seasonality at Easter Bush, aside from a clear set of outliers. There is a weak warm-season peak in observed v_d (Fig. 1). Models show weak warm-season maxima (Fig. 3) and relatively similar relative seasonal amplitudes (Fig. 9). Some models are clear outliers, however. For example, GEM-MACH Wesely and TEMIR Wesely psn show particularly strong relative seasonal amplitudes (Fig. 9), in part due low wintertime v_d. The absolute standard deviation across models for v_d is higher during winter than summer (Fig. 11). This only happens at Easter Bush

and Hyytiälä; however, as noted above, the wintertime model spread reduces when considering the full versus interquartile range, suggesting that low outliers may drive the large standard deviation across models.

For most models, the primary driver of v_d seasonality is stomatal uptake (Fig. 6). Individual contributions from stomatal uptake barely contribute for GEM-MACH Wesely, TEMIR Wesely, and TEMIR Wesely BB. Several models, including GEM-MACH Wesely, GEM-MACH Zhang, and TEMIR Wesely models, and to a lesser extent some TEMIR Zhang models, simulate large contributions from soil uptake individually and/or via correlations with other pathways. Only two models, in contrast to seven at the other grassland examined (Bugacpuszta), suggest that individual contributions from cuticular uptake matter for seasonality.

Most models are similar in terms of magnitude and seasonality shape of stomatal uptake (Fig. 10), as well as relative seasonal amplitudes (Fig. 9). Exceptions are GEM-MACH Wesely (a very strong peak during July and is near zero after July; and thus shows an anomalous seasonal amplitude), TEMIR Medlyn (much higher than other models during warm months), as well as IFS SUMO Wesely and WRF-Chem Wesely (slightly higher than other models especially during spring). DO₃SE models are also an exception – they show very different seasonal cycles from each other, despite both being high and seasonally distinctive relative to other models. DO₃SE psn also shows an anomalous seasonal amplitude.

At Easter Bush, *LAI* peaks during July, with a broad maximum from May to November and low values during February and March (Fig. 10). With some exceptions, models bound the observed relationship between v_d and *LAI*, agreeing on a fairly weak but positive dependence (Fig. 7). Outliers with respect to the v_d-*LAI* relationship (GEM-MACH Wesely and TEMIR Wesely psn) also indicate that stomatal uptake does not strongly influence v_d seasonality, suggesting the latter is incorrect.

During summer, model spreads for v_d and deposition pathways at Easter Bush are highest for soil uptake, then stomatal uptake, and then cuticular uptake (Fig. 11). Most models simulate moderate or substantial stomatal uptake, but there is a division as to whether models simulate very low, low, or moderate cuticular uptake (Fig. 5). Models simulate substantial soil uptake, both in terms of absolute magnitudes and the relative contribution to v_d. Exceptions are DO₃SE models, which have very low soil uptake. Stomatal fractions range from 10% to 70%, with most models around 30% and only four models above 40% (Fig. 12). The range across models for stomatal fractions is one of the largest across sites, but the interquartile range is one of the smallest. High agreement in the stomatal uptake magnitude, seasonality shape, and relative amplitude, as well as stomatal fractions, across most models suggests that an appropriate next step would be to use observation-based estimates of stomatal uptake (e.g., from water vapor fluxes) to evaluate whether models are accurate with respect to this pathway.

During winter, models simulate that v_d is dominated by soil uptake, with some models simulating low-to-moderate contributions from cuticular uptake (Fig. 5). Only DO₃SE models and GEM-MACH Wesely show little soil uptake; while soil uptake is still a large fraction of v_d for GEM-MACH Wesely, it is a small fraction for DO₃SE models. Stomatal uptake is very low except for

046   DO₃SE psn. Stomatal fractions are between 0% and 10% except DO₃SE psn (50%) (Fig. 12). Because models largely agree that

047   wintertime v_d is dominated by soil uptake, and most models overestimate January–April v_d, but underestimate November–

048   December values, future work should focus on changes in soil uptake on weekly to monthly timescales. We do not have snow

049   depth measurements at Easter Bush, but do not expect that accounting for snow would substantially impact simulated values.

050   **5.4 Ramat Hanadiv**

051   Ramat Hanadiv is a shrubland in Israel near the Mediterranean coast. The spread based on the model with the highest annual average

052   v_d divided by the model with the lowest is factor of 2.2 (2.3 during summer and 2 during winter) but based on the interquartile range

053   is factor of 1.4 (1.3 during summer and 1.5 during winter). Metrics are on the lower end of the cross-site range.

054

055   There are ozone flux observations at Ramat Hanadiv during January–September only, and only March, August, and September

056   have substantial data coverage. Three different years contribute to multiyear averages, with each year only having a few months

057   of data per year. For some months, years have overlapping data coverage. Some months with data for two years show interannual

058   variability while others do not. Like Bugacpuszta and Auchencorth Moss, more data is needed to assess interannual variability as

059   well as seasonality at Ramat Hanadiv. Below, we examine 'multiyear averages', acknowledging that only six months of the year

060   have two years of data, and three months have data from one year only.

061

062   Models show weak relative seasonal amplitudes for v_d (Fig. 9). Values are very similar across models, more so than other sites.

063   Most models also show weak relative seasonal amplitudes for stomatal uptake, but there is a larger spread across the central models

064   and some outliers. The lack of simulated seasonality for most models is likely due to constant *LAI*. Any simulated v_d seasonality

065   is from stomatal uptake (Fig. 6), more so than (or in contrast to) the other short vegetation sites. GEM-MACH Wesely and WRF-

066   Chem Wesely, which are two of three models with input initial resistances (i.e., model parameters) varying by season, have very

067   distinct v_d seasonal cycle shapes at this site, compared to the rest of the models (Fig. 3).

068

069   The seasonal cycle shape of observed v_d at Ramat Hanadiv is hard to discern with many months with low or no data coverage

070   (Fig. 1). The current set of observations indicates higher values during early spring and lower values during late summer. Individual

071   models do not capture this, with models simulating near-constant values year-round or increases from winter to early summer (Fig.

072   3). Exceptions are MLC-CHEM, DO₃SE models, and GEM-MACH Wesely, which at least somewhat capture that the predominant

073   seasonality feature should be lower late-summer values and higher early-spring values.

074

075   Across months with observations, models bracket observed v_d (Fig. 2). In particular, models are within -35% to +55% of observed

076   seasonal averages (Fig. 4). Exceptions occur during summer and include GEM-MACH Wesely, IFS GEOS-Chem Wesely, WRF-

077   Chem Wesely, GEOS-Chem Wesely, TEMIR Wesely models, and TEMIR Zhang models (biases are higher than +55%). The

078   central models' spread only brackets observed values during January-April and June, and is too high during May and July-

September. The largest deviation happens during August. Thus, like Bugacpuszta, late summer is when the largest model biases occur at Ramat Hanadiv.
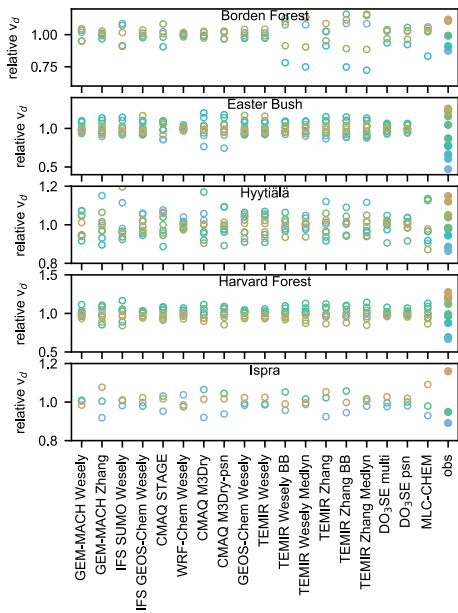
Figure 13 Simulated and observed yearly summertime mean ozone deposition velocities (v_d) for sites with records of at least three summers. Values are normalized by the multiyear average of the respective model or observations to emphasize ranking and spread across years. Colors rank yearly values from low (blue) to high (gold) for the observations. Model year when observed year is missing is not shown. The highest year for Easter Bush is not shown because it is very high (2x the multiyear mean observed value).

DO3SE models, MLC-CHEM, and TEMIR psn show weak v_d decreases from spring to fall. These models plus CMAQ models consider stomatal conductance dependencies on soil moisture. CMAQ models show weaker v_d declines from spring to fall, compared to DO3SE models, MLC-CHEM, and TEMIR psn. This behavior is consistent with their soil moisture dependencies. For example, TEMIR psn and IFS SUMO Wesely models' stomatal conductance is set to zero when input soil moisture is less than wilting point, but CMAQ models have more of a taper effect. Future work should aim to understand the role of soil moisture on observed seasonal variation in v_d and stomatal uptake.

Models with the highest biases during April-September are TEMIR models, GEM-MACH Wesely, WRF-Chem Wesely, GEOS-Chem Wesely, and IFS GEOS-Chem Wesely (Fig. 3). These models simulate the highest stomatal uptake during this period, apart

102 from a few models with lower-than-average nonstomatal uptake (CMAQ STAGE, DO₃SE models, GEM-MACH Zhang) (Fig. 5).

103 Only CMAQ M3Dry models capture low observed v_d during August. CMAQ M3Dry-psn captures July, but CMAQ M3Dry does

104 not, and they do not capture observed values during other months. Notably, CMAQ M3Dry models show much lower summertime

105 stomatal uptake than other models. CMAQ M3Dry models may have more skill during summer than other models, but like the

106 other models, they struggle with seasonality.

107

108 Lower canopy uptake is the highest for Ramat Hanadiv, during both summer and winter, across sites. However, relative and

109 absolute contributions of lower canopy uptake are still low compared to soil and stomatal uptake (and in some cases cuticular

110 uptake). Lower canopy uptake is only simulated by Wesely models. Mostly Wesely models simulate low cuticular uptake compared

111 to other models, so lower canopy uptake does not necessarily contribute to the very high model biases of Wesely models.

112

113 Uptake by soil and stomata mostly comprises v_d at Ramat Hanadiv during winter and summer (Fig. 5). The model spread is highest

114 for stomatal uptake during winter and summer, compared to other pathways (Fig. 11). The spread for soil uptake is remarkably

115 low given its importance across models (less than 20% relative spread compared to mostly between 40–75% of v_d). Ramat Hanadiv

116 is the only site with a large wintertime spread across stomatal uptake estimates, and similar model ranges of stomatal fractions

117 during winter and summer. Models except WRF-Chem Wesely show substantial wintertime stomatal uptake. In general, stomatal

118 uptake is very high compared to other sites during winter, presumably due to the site's Mediterranean climate. Models also show

119 substantial summertime stomatal uptake except CMAQ M3Dry. Wintertime stomatal fractions range from 20% to 50% across

120 models (Fig. 12). The range is only slightly less across central models (25–40%), suggesting that wintertime stomatal uptake is a

121 key uncertainty at this site. The central models simulate a very small range of summertime stomatal fractions (similar to only

122 Easter Bush), centering on 40%, but the full range spans 12.5% to 50%.

123

124 At Ramat Hanadiv, most models should simulate lower stomatal and/or nonstomatal uptake during late summer, on par with

125 CMAQ M3Dry models, which have both lower stomatal and nonstomatal uptake than other models. However, stomatal and/or

126 nonstomatal uptake should be higher than simulated by CMAQ M3Dry during other times of year, and other models bracket

127 observations well at this time so they may provide insight here as to driving processes. Observational constraints on stomatal

128 uptake year-round will help to further narrow uncertainties as to whether and when models need improvement with respect to

129 stomatal versus nonstomatal uptake, including when they capture the absolute magnitude of v_d well.

130 **5.5 Ispra**

131 Ispra is a deciduous broadleaf forest in northern Italy. The model spread in terms of the model with the highest annual average

132 v_d divided by the model with the lowest is a factor of 2.3 (3.1 during summer and 2.9 during winter) but based on the interquartile

133 range is 1.5 (1.5 during summer and winter). These metrics are towards the higher end of the metrics for other sites.

134

Observed multiyear monthly mean v_d values are similar year-round except during March and April when values are lower (Fig. 1). This observed climatological seasonal pattern is consistent across years except during October–December. For example, observed v_d is high during October 2013, low during November 2015, and high during December 2014. As discussed below, the causes of high year-round values are uncertain; this, together with strong interannual variability during fall, indicates a need for more years of observations at Ispra, coupled with complementary measurements targeting individual pathways. Below, we focus on multiyear averages, after briefly evaluating summertime interannual variability.

Summertime observed v_d at Ispra is higher during 2014 than 2013 and 2015 (Fig. 1). Accordingly, model skill at interannual variability should be determined by whether models capture the much higher summertime average during 2014 versus other years. Some models suggest that v_d should be highest during 2014, but hardly any models capture the large observed relative difference between this year and other years (Fig. 13). The exception is MLC-CHEM, and to a lesser extent GEM-MACH Zhang. Thus, most models have little skill at simulating summertime interannual variability at this site.

The v_d seasonality shape is a clear discrepancy between observations and models at Ispra. In contrast to the observations, multiyear monthly mean v_d peaks during warm months in the central models (Fig. 2). There are similar v_d relative seasonal amplitudes across models, aside from GEM-MACH Wesely (Fig. 9), especially relative to other forests. The central models bracket the observations during April–September, but models show a low bias during October–March. Relative summertime and springtime biases range from -33% to +32% except DO₃SE multi, TEMIR Zhang, TEMIR Wesely BB, and GEM-MACH Zhang (lower) as well as GEM-MACH Wesely (higher) (Fig. 4). Relative wintertime and fall biases range from -22% to -89% across models. Ispra is the only site besides Auchencorth Moss where models are biased in the same direction for an extended period (i.e., longer than three months).

Models show that stomatal uptake largely drives v_d seasonality at Ispra (Fig. 6). Models simulate contributions from cuticular uptake, mostly via positive correlations with the stomatal pathway. Models with non-zero individual contributions from cuticular uptake (GEM-MACH Zhang, CMAQ models, and DO₃SE models) are the same as at Harvard Forest and Borden Forest. Models show v_d maxima during warm months because v_d strongly depends on *LAI* (Fig. 7), which has a broad maximum during warm months (Fig. 10). Specifically, simulated v_d tends to increase with *LAI*, which contrasts with observed v_d.

A couple of models deviate from the majority in terms of the v_d seasonal cycles (Fig. 3). For example, GEM-MACH Zhang is low during warm months and GEM-MACH Wesely is very high during warm months. WRF-Chem Wesely shows higher wintertime v_d than other models, especially January–March, due to high soil uptake, as well as high early-springtime uptake due to combined high soil and stomatal uptake (Figs. 5, 10). GEM-MACH Wesely and WRF-Chem Wesely are two of three models with input initial resistances (i.e., model parameters) varying by season, which likely causes these models to produce distinct seasonal cycle shapes. GEM-MACH Zhang has low summertime stomatal and nonstomatal uptake, compared to the rest (Fig. 5).

Deleted: is

Deleted: vs.

Deleted: Figure 13 shows that some

Deleted: .

Deleted: Ispra

Deleted: central models'

Deleted: Models show

Deleted: ,

Deleted: (Fig. 9). Central

183

184 Even though the central models bracket observed multiyear monthly mean v_d during April–September at Ispra (Fig. 2), and many

185 individual models capture the increase from April to May, individual models fail to capture that values should be roughly constant

186 from July to September, rather than decrease (Fig. 3). For example, some models (including DO₃SE psn, MLC-CHEM) simulate

187 April–July multiyear monthly mean v_d very well but not August and September when they are low (because they simulate

188 decreases from early to late summer). Models may erroneously simulate decreases from early to late summer because they depend

189 too strongly on *LAI*, which weakly declines from July to September, or soil moisture.

190

191 During summer at Ispra, the model spread is largest for stomatal uptake relative to other pathways (Fig. 11). Models simulate

192 substantial stomatal uptake, with DO₃SE multi and GEM-MACH Zhang simulating the lowest (but nonnegligible) values (Fig. 5).

193 The highest stomatal uptake is simulated by GEM-MACH Wesely, GEOS-Chem Wesely, IFS GEOS-Chem Wesely, IFS SUMO

194 Wesely, TEMIR Wesely, and MLC-CHEM. The central models show stomatal fractions of 50% to 77.5%, but the full model range

195 is 37.5% to 87.5% (Fig. 12). The model spread across pathways is second largest for cuticular uptake. Soil uptake is very low

196 across models except WRF-Chem Wesely as well as CMAQ STAGE and GEM-MACH Wesely where it is higher. The ranking

197 and spread across pathways of pathways' standard deviations at Ispra is very similar to Borden Forest and Harvard Forest, but not

198 Hyytiälä. Given that the central models capture the average magnitude of v_d during the warm season well but disagree mainly on

199 stomatal versus cuticular fractions as well as monthly changes within the warm season (or lack thereof), future work should

200 prioritize using observational constraints on stomatal uptake to further evaluate model performance.

201

202 During winter at Ispra, simulated v_d tends not to be dominated by one pathway; instead, there are small contributions from 2–4

203 pathways (Fig. 5). Exceptions are WRF-Chem Wesely where soil uptake dominates and a few models where cuticular uptake tends

204 to dominate (e.g., CMAQ STAGE, CMAQ M3Dry, DO₃SE multi). The model spread in soil uptake is largest across pathways

205 (Fig. 11), and high WRF-Chem Wesely values play a role in this. Otherwise, soil uptake is low, or in a few cases moderately low

206 (e.g., MLC-CHEM, IFS SUMO Wesely). Cuticular uptake is close behind soil uptake in terms of the spread. Stomatal fractions

207 span 0% to 47.5%, with the largest range across the central models (10–45%) across sites (Fig. 12). Eleven models show low-to-

208 moderately-low stomatal uptake, but others predict none (GEM-MACH Wesely, GEM-MACH Zhang, CMAQ STAGE, GEOS-

209 Chem Wesely, CMAQ M3Dry, TEMIR Wesely, DO₃SE multi). More models predict non-zero stomatal uptake at Ispra compared

210 to other sites, apart from Ramat Hanadiv. Whether simulated wintertime stomatal, cuticular, soil, and/or lower canopy uptake

211 should be higher at Ispra is uncertain. There may also be fast ambient losses of ozone. Ispra does not have snow depth observations,

212 but we anticipate that accounting for snow would not substantially change model results. Future attention should be placed

213 elsewhere with respect to better understanding of large wintertime model biases. A key first step is to understand whether there is

214 stomatal uptake during winter, and then what its magnitude is.

Deleted: July–September

Deleted: -

Deleted: Central

Deleted: -

Deleted: v_d

Deleted: vs.

5.6 Hyytiälä

Hyytiälä is a boreal evergreen needleleaf forest in Finland. The model spread in terms of the model with the highest annual average v_d divided by the model with the lowest is a factor of 2.7 (1.9 during summer and 21 during winter) but based on the interquartile range is a factor of 1.6 (1.4 during summer and 2.4 during winter). The metrics of model spread at Hyytiälä are at the higher end of other sites' values, especially for annual and winter values.

Observed multiyear monthly mean v_d maximizes during warm months, and this is consistent across years (Fig. 1). Most models simulate higher values during warm months relative to cool months (Fig. 3). Outliers with respect to the seasonality are TEMIR Zhang (strong overestimate during cold months leading to near constant values year-round), GEM-MACH Wesely (strong overestimate during warm months), GEOS-Chem Wesely and TEMIR Wesely (overestimate during summer), and WRF-Chem Wesely (strongly overestimate during early spring). Here we examine observed relative seasonal amplitude for v_d because observed and (most) modeled values have warm-month maxima and cool-month minima as well as full years of observations, allowing meaningful comparisons. The observed relative seasonal amplitude falls within the central models' range, but towards the upper end, and most models predict too-low values (Fig. 9).

In general, the largest relative model v_d biases at Hyytiälä occur during cool months (Fig. 4) and the wintertime v_d model spread is the highest relative to other sites (Fig. 11), implying that wintertime v_d at this site is a key uncertainty. Wintertime relative biases range from -81% to +87% except for a few models that have much higher positive biases: GEM-MACH Zhang (+307%), TEMIR Zhang models (+211 to +245%), and DO$_3$SE psn (+104%). However, most models are biased high, apart from IFS SUMO Wesely (-5%), IFS GEOS-Chem Wesely (-81%), GEOS-Chem Wesely (-62%), and TEMIR Wesely models (-15% to -57%). Models largely simulate that cuticular and soil uptake are dominant contributors (Fig. 5). Most models simulate near-zero wintertime stomatal uptake, despite relatively high LAI (Fig. 10), implying that models have at least rudimentary skill at capturing the seasonality of evergreen vegetation. The central models show stomatal fractions between 0% and 12.5%, but a few models show contributions of 17.5% to 50% (Fig. 12). The model with the 50% (TEMIR Wesely BB) in addition to very low stomatal uptake has very low nonstomatal uptake.

During winter, models also show differences in partitioning and magnitudes of cuticular versus soil uptake (Fig. 5). The model spread in cuticular uptake is larger than soil uptake (Fig. 11) – Hyytiälä is the only site where this happens – presumably because LAI remains relatively high at this site year-round and models seem to suggest that cuticular uptake is more important than ground uptake at forests. Ten models show substantial cuticular uptake, whereas only two models show low cuticular uptake, and the rest show none. Seven models show substantial soil uptake, while ten show very little to none. Models showing high versus low cuticular and soil uptake are sometimes the same. For example, four simulate substantial cuticular uptake and soil uptake, and five simulate minimal cuticular uptake and soil uptake. In the former case, models overestimate wintertime v_d; in the latter, models underestimate it. Most models capture small observed decreases in wintertime v_d with snow, but the spread across models during snow and snow-free periods is very large (Fig. 8). Thus, attention

should focus on constraining wintertime cuticular versus soil uptake. Establishing whether there is cuticular and/or soil uptake during winter is an important first step towards narrowing model uncertainties.

Within the warm season, whether models show pronounced v_d seasonality varies (Fig. 3). Models also do not capture that observations maximize during August and minimize during March (Fig. 2). Specifically, models tend to overestimate late-winter/spring v_d while underestimating fall/early-winter v_d, as indicated by comparing the interquartile range to observations. Multiyear monthly mean *LAI* peaks during August (around 3.75 m^2 m^{-2}), after an increase from May (Fig. 10). Then, *LAI* decreases to November, and is constant from November to May (around 2.75 m^2 m^{-2}). Models bound the observed v_d-*LAI* relationship, and largely capture the increase in v_d as *LAI* increases from 3 to 3.5 m^2 m^{-2} (Fig. 7). However, most models do not capture the v_d change as *LAI* increases from 3.5 to 3.75 m^2 m^{-2} where observations suggest that the slope should be the same as for 3 to 3.5 m^2 m^{-2} (instead models suggest decreases). Models also overestimate the increase in v_d as *LAI* increases from 2.75 to 3 m^2 m^{-2}. Some effect overrides *LAI*'s influence on seasonality in stomatal uptake in models, given that both observed *LAI* and v_d peak during August, but simulated stomatal uptake and v_d do not. Simulated declines with soil moisture may play a role here.

Models simulate that stomatal uptake and co-variations between pathways are important seasonality drivers (Fig. 6). Only two models suggest that there are not individual contributions by stomatal uptake (GEM-MACH Wesely, GEM-MACH Zhang), but several models suggest that the sum of individual contributions from other pathways and co-variations are at least as important as stomatal uptake. There are similarly evenly distributed spreads across models in terms of relative seasonal amplitudes for stomatal uptake and v_d (Fig. 9). Most models' stomatal uptake seasonal cycles show a broad warm-season peak, apart from some models with more pronounced seasonality during warm months (e.g., GEM-MACH Wesely, GEOS-Chem Wesely, TEMIR Wesely, CMAQ M3Dry models) (Fig. 10). IFS SUMO Wesely peaks during May and then declines afterwards. Model outliers in terms of high magnitudes of summertime stomatal uptake include GEOS-Chem Wesely, TEMIR Wesely, MLC-CHEM, and GEM-MACH Wesely.

During summer, relative model biases range from -14% to +20% except for GEM-MACH Wesely (+88%), IFS SUMO Wesely (-25%), WRF-Chem Wesely (+32%), TEMIR Wesely (+34%), and GEOS-Chem Wesely (+40%) (Fig. 4). Models show substantial stomatal uptake (Fig. 5) with stomatal fractions spanning 27.5% to 80% (Fig. 12). The central models show 42.5–65%. Models that simulate lower canopy uptake show low uptake via this pathway, like other forests. The largest model spread is for soil and stomatal uptake, but closely followed by cuticular uptake (Fig. 11), which is distinct from other forests. Soil uptake's high model spread is due to high values from WRF-Chem Wesely and GEM-MACH Wesely and zero values from DO$_3$SE models; other models simulate more similar estimates of soil uptake, ranging from low to moderate. Models show nonnegligible cuticular uptake but disagree as to whether it is low or moderate. Observational constraints on stomatal uptake will help to further narrow uncertainties as to the magnitude and relative contribution of summertime stomatal uptake, as well as changes on weekly to monthly timescales.

Deleted: vs.

Formatted: Not Expanded by / Condensed by

Deleted: a number of

Deleted: Central

Deleted: uptakes'

Deleted: large estimates

Deleted: soil uptake

Deleted: values

298 Key findings regarding seasonality at Hyytiälä include: models struggle to capture the exact timing of maximum and minimum values,

299 models overestimate wintertime values and thus underestimate the relative seasonal amplitude, and models disagree about seasonality

300 within the warm season, while generally capturing that there should higher values during warm months. Silva et al. (2019) use Hyytiälä

301 observations to train a machine learning model and apply the model to predict v_d at Harvard Forest, finding that their model predicts a late

302 summertime peak in v_d, which is observed at Hyytiälä but not at Harvard Forest. Assuming that differences between these two sites are

303 characteristic of sites' broad LULC classifications, both our findings and theirs suggest a need for improved predictive ability of seasonality

304 differences between coniferous versus deciduous forests.

305

306 Thus far we have discussed multiyear averages at Hyytiälä. We now turn to summertime interannual variability. Models do not capture the

307 summertime ranking across years (Fig. 13). Several models predict particularly low (high) v_d during some summers, but the observations

308 do not indicate low (high) values for these years. Some models are close to capturing the degree of summertime interannual variability, but

309 typically these models show a more uneven distribution across years than suggested by observations. Notably, models show more variability

310 in their year-to-year rankings at Hyytiälä compared to other sites with longer records. Nonetheless, we conclude that model skill is poor at

311 this site in terms of summertime interannual variability.

312 **5.7 Harvard Forest**

313 Harvard Forest is a temperate mixed forest in the northeastern United States. The model spread in terms of the model with the highest

314 annual average v_d divided by the model with the lowest is a factor of 1.9 (1.8 during summer and 4.8 during winter) but based on the

315 interquartile range is a factor of 1.2 (1.4 during summer and 2.6 during winter). Like other forests, the wintertime spread is largest.

316 Aside from winter values, the metrics of the spread at Harvard Forest are on the lower end of estimates across sites.

317

318 Observed multiyear monthly mean v_d maximizes during May–September (Fig. 1). Observed seasonal cycles vary across years, but values

319 are generally higher during warmer versus cooler months across years. We focus on multiyear averages until the subsection end, where we

320 touch on summertime interannual variability. Models capture that v_d peaks during warm months (Fig. 2). The exception is GEM-MACH

321 Zhang, which has similar monthly averages year-round. Despite capturing seasonality shape, models overestimate the relative seasonal

322 amplitude (Fig. 9), apart from GEM-MACH Zhang, TEMIR Zhang, and TEMIR Zhang BB (substantial underestimate) as well as DO₃SE

323 psn (slight underestimate). Outliers show high wintertime v_d relative to other models and observations, implying that the models bounding

324 the observed relative seasonal amplitude does not necessarily indicate ensemble skill.

325

326 Models are within ±65% of observed values across seasons (Fig. 4). Exceptions occur during spring and summer for GEM-MACH Wesely,

327 winter and spring for GEM-MACH Zhang, and spring for WRF-CHEM Wesely and TEMIR Zhang Medlyn. The central models bracket

328 observations well. Specifically, observations fall in the lower end of the spread during warm months and the upper end during November–

329 January, but otherwise are in the middle of the spread. Across models, summertime biases are positive, ranging from +4 to +144%, except

330 IFS GEOS-CHEM Wesely (-4%) and TEMIR Zhang (-2%). Thus, overestimated relative seasonal amplitudes (Fig. 9) are likely due to

331 high summertime v_d. Previous work suggests that GEOS-Chem's overestimate at Harvard Forest is due to too-high model *LAI* (Silva and

338 Heald, 2018), but clearly there is another issue because models are forced with site-specific *LAI* here. Most models tend to underestimate

339 v_d at low *LAI* and overestimate v_d at high LAI, overstating v_d increases with *LAI* (Fig. 7).

340

341 During winter, model biases tend to be negative, ranging from -24% to -71%, with exceptions of GEM-MACH Wesely (+85%), TEMIR

342 Zhang models (+25% to +33%), and MLC-CHEM (+13%) as well as two models with very low negative biases (DO₃SE psn and WRC

343 Chem Wesely) (Fig. 4). The wintertime model spread is highest for soil uptake across pathways, with cuticular uptake close behind. Soil

344 uptake is always at least 37.5% (and up to 70%) of v_d except for GEM-MACH Wesely (20%) (Fig. 5). Most models show little-to-no

345 stomatal uptake, but some models show nonnegligible values. The central models show stomatal fractions of 5–15% (Fig. 12). Estimates

346 for cuticular uptake vary across models – there are substantial, small, and negligible contributions. Lower canopy uptake is low for models

347 that simulate this pathway but can be an important fraction of v_d. There are no snow depth observations at Harvard Forest. Assuming no

348 snow throughout the time period may influence some models' ability to estimate wintertime v_d well. However, based on our analysis at

349 other sites, we do not anticipate the lack of snow data to be the main driver of model-observation or model-to-model differences.

350 Establishing whether there should be stomatal or cuticular uptake during winter would be a useful first step in further constraining models.

351 Otherwise, attention should focus on narrowing uncertainties related to wintertime ground uptake.

352

353 Some models capture the broad observed v_d maximum during the warm season while others show more seasonality within the warm

354 season (Fig. 3). A few models show pronounced declines after July (e.g., MLC-CHEM, TEMIR psn). Pronounced declines after July do

355 not occur in observed multiyear monthly averages but occur during several individual years (Fig. 1). Simulated pronounced declines may

356 follow these models' soil moisture dependencies (note that not all models have soil moisture dependencies, and there are differences among

357 models that do have them). That models with soil moisture dependencies are not capturing the observed multiyear mean seasonality may

358 be due to soil moisture dependencies themselves, and/or with uncertainty in soil moisture input. For example, soil moisture was not

359 measured during all years with ozone fluxes at Harvard Forest, and thus we use a climatological average during those years. Future work

360 should examine seasonality during individual years, paying attention to years with climatological average versus year-specific input soil

361 moisture, to determine model strengths and limitations.

362

363 Models show stomatal uptake is an important driver of v_d seasonality at Harvard Forest (Fig. 6). Six models estimate that stomatal uptake

364 largely drives seasonality, with some contributions from covariations between pathways (mainly positive covariations between stomatal

365 and cuticular pathways). The rest estimate moderate contributions from stomatal uptake, but at least as much of an influence from individual

366 nonstomatal pathways or covariations (positive or negative). Models show a clear seasonality to stomatal uptake, with a peak during warm

367 months and zero or near zero values during winter (Fig. 10). The spread for relative seasonal amplitude for stomatal uptake across the

368 central models is the smallest across sites (Fig. 9). Six models deviate from the rest, however. CMAQ M3Dry, CMAQ STAGE, and GEM-

369 MACH Wesely have high relative seasonal amplitudes for stomatal uptake, GEM-MACH Zhang, IFS SUMO Wesely, and DO₃SE psn

370 have low values. In contrast, the spread for relative seasonal amplitude for v_d has a more even distribution across models. Thus, while there

371 is a fair amount of agreement across models in terms of seasonality in stomatal uptake, models disagree as to nonstomatal uptake seasonality

379 and its role on v_d seasonality. Together with findings that models exaggerate the v_d-*LAI* relationship and most models overestimate the
380 relative seasonal amplitude for v_d, this result implies future work should aim to better constrain nonstomatal influences on seasonality.
381
382 During summer, the model spread is highest for stomatal uptake, with cuticular uptake close behind (Fig. 11). Models show substantial
383 contributions from stomatal uptake – the model range spans 30% to 80%, but the central models' range spans 50% to 70% (Fig. 12).
384 Estimates for cuticular uptake vary across models (Fig. 5) – there are substantial, moderate, and low contributions. Soil uptake is low,
385 except for WRF-Chem Wesely and GEM-MACH Wesely. Similar to other forests, lower canopy uptake is low for models that simulate
386 this pathway. Observational constraints on stomatal uptake will help to further narrow model uncertainties as to magnitude and
387 relative contribution of summertime stomatal uptake.
388
389 Interannual variability is strong across months (Fig. 1). A series of papers pointed this out for daytime values and investigated
390 drivers during summer (Clifton et al., 2017, 2019). Models capture neither the large observed spread across years during summer
391 nor the ranking of years (Fig. 13). Most models simulate that some of the summers with the highest observed v_d have low v_d.
392 Previous work points to nonstomatal pathways driving summertime interannual variability (Clifton et al., 2017, 2019), and thus
393 models may be lacking in their ability to simulate the degree to which nonstomatal uptake varies from year to year, and likely key
394 process dependencies.

395 **5.8 Borden Forest**
396 Borden Forest is a mixed forest in the boreal-temperate transition zone in Canada. The model spread in terms of the model with the
397 highest annual average v_d divided by the model with the lowest is a factor of 2.3 (3.4 during summer and 10 during winter) but based
398 on the interquartile range is a factor of 1.4 (1.8 during summer and 3 during winter). The metrics of model spread are towards the
399 higher end of other sites, except for winter and the summertime interquartile range when they are the highest.
400
401 Observed multiyear monthly mean v_d shows a broad maximum during warm months at Borden Forest (Fig. 1), like Harvard Forest
402 and Hyytiälä. However, uniquely, observations at Borden Forest show particularly large winter versus summer differences and steep
403 changes during spring and fall. Specifically, v_d increases from March to June by 0.5 cm s^{-1}. Then, v_d remains high from June to
404 September (0.6–0.65 cm s^{-1}) and declines steeply from September to November. Models simulate higher v_d during warmer versus
405 cooler months (Fig. 3), and the observed relative seasonal amplitude lies close to the middle of the central models' spread (Fig. 9).
406 However, there is a clear discrepancy between models and observations in that models do not capture very high v_d across warm
407 months (Fig. 3). All models except GEM-MACH Wesely have low summertime biases, with a range from -15% to -74% (Fig. 4).
408 In general, high observed v_d during warm months at Borden Forest needs better understanding, given uncertainty in ozone flux
409 measurements from the gradient technique (see discussion in Sect. 4.2).
410
411 The individual contribution from stomatal uptake is a key driver of v_d seasonality, apart from IFS SUMO Wesely, CMAQ STAGE,
412 and DO$_3$SE models (Fig. 6). These four models do, however, show stomatal contributions to seasonality via correlations with other

pathways. Notably, there are more individual nonstomatal (e.g., ground, cuticular) contributions to seasonality at Borden Forest than other forests. There are also a variety of simulated v_d seasonal cycle shapes at Borden Forest, in contrast to Harvard Forest and Ispra. Some models simulate weak changes from cooler to warm months (DO$_3$SE models, TEMIR Zhang models, IFS SUMO Wesely, GEM-MACH Zhang) while others simulate moderate changes (WRF-Chem Wesely, MLC-CHEM, CMAQ STAGE) or strong changes (GEOS-Chem Wesely, TEMIR Wesely, IFS GEOS-Chem Wesely, GEM-MACH Wesely, CMAQ M3Dry models, TEMIR Wesely psn). TEMIR psn models simulate erratic monthly changes during June to October. Generally, models with the strongest changes from cooler to warm months simulate that stomatal uptake predominately drives v_d seasonality (Fig. 6). Conversely, models with weak changes from cooler to warm months indicate that nonstomatal pathways contribute more predominantly.

With respect to the relationship between multiyear monthly mean v_d and *LAI*, observed v_d increases with *LAI* but the slope varies (Fig. 7). The observed slope is strongest for *LAI* increases from 0.5 to 1 m^2 m^{-2}, and models tend to underestimate the change, but do simulate increases. Then, the observed slope weakens but remains positive for *LAI* increases from 1 to 2 m^2 m^{-2} – most models suggest decreases instead. Then, the observed slope weakens even further for *LAI* increases above 2 m^2 m^{-2}. Some models capture the slope of *LAI* increases above 2 m^2 m^{-2} but others exaggerate it (e.g., GEM-MACH Wesely, GEOS-Chem Wesely, TEMIR Wesely, CMAQ M3Dry models). The main issue is that individual models tend not to capture that there should be relatively high v_d during May and October (Fig. 3). Specifically, models simulate a later spring onset with respect to the v_d seasonality as well as an earlier fall decline, and thus a shorter season of elevated v_d than observed. We thus suggest that models are too strongly tied to *LAI*, which strongly increases from May to June and strongly decreases from September to October (Fig. 10).

Additionally, many models do not capture that multiyear monthly mean v_d is similar during June–September (Fig. 3). Some models simulate declines from August to September (e.g., CMAQ M3Dry-psn, GEOS-Chem Wesely, TEMIR Wesely, GEM-MACH Wesely). A weak decline from August to September occurs in the observed multiyear average (the strong decline happens from September to November); some models capture the August-to-September decline's magnitude while others exaggerate it. Some models show low values during July (e.g., TEMIR psn), in addition to August-to-September declines. Observations show low values during July not in multiyear monthly mean seasonal cycles, but during 2012 and perhaps 2008 (Fig. 1). Many models show peak v_d during June. Again, this does not happen in observed multiyear monthly averages, but occurs in 2010. Thus, models may exaggerate depositional responses (in particular, stomatal) to changes in environmental conditions (e.g., soil moisture) on a climatological basis but have some skill in certain years.

During summer, the largest model spread across pathways occurs for stomatal uptake, followed by cuticular uptake and then soil uptake (Fig. 11), similar to Harvard Forest and Ispra. Models show substantial stomatal uptake, apart from two with very low values (IFS SUMO Wesely and DO$_3$SE multi). Stomatal fractions range from 20% to 80% across models, but 40% to 62.5% across the central models (Fig. 12). Eight models simulate lower cuticular uptake, while the rest simulate higher cuticular uptake (Fig. 5).

Models that have the lower canopy uptake pathway show low values of cuticular uptake, with two exceptions: GEM-MACH Wesely, which has high cuticular uptake, and MLC-CHEM, which does not archive lower canopy uptake diagnostic but has low cuticular uptake. Most models simulate low soil uptake, but a few models simulate moderate-to-high soil uptake (GEM-MACH Wesely, GEM-MACH Zhang, CMAQ STAGE, WRF-Chem Wesely, and MLC-CHEM). Observational constraints on stomatal uptake will help to further narrow model uncertainties as to the magnitude and relative contribution of stomatal uptake.

During winter, models show a mixture of over- and under-estimates. Models with overestimates are TEMIR Zhang models (+68 to +73%), GEM-MACH Zhang (+124%), WRF-Chem Wesely (+13%), DO$_3$SE multi (+9%) and DO$_3$SE psn (+44%). Otherwise, underestimates span -20% to -78%. Models with high v_d simulate high cuticular uptake, generally high soil uptake, and in one case nonnegligible stomatal uptake (DO$_3$SE psn) (Fig. 5). Soil and cuticular uptake show the highest spreads across models, with soil uptake the highest, similar to Harvard Forest and Ispra (Fig. 11). The central models show very low stomatal fractions, but outliers span 10% to 30% (Fig. 12). Apart from DOS$_3$E psn, high stomatal fractions are due to high nonstomatal uptake, rather than high stomatal uptake. Many models largely capture that observations show no v_d change with snow, although some slightly overestimate the change. Thus, the primary issue with wintertime model biases is likely unrelated to responses to snow, and rather related to mischaracterized magnitudes of pathways or responses to other environmental conditions.

In terms of summertime interannual variability, some models underestimate the relative spread across years (Fig. 13), but some only slightly underestimate it (IFS SUMO Wesely, CMAQ STAGE, TEMIR Zhang, MLC-CHEM, DO$_3$SE models) and a few exaggerate it (TEMIR psn). Models generally struggle to capture the observed relative distribution across summers (i.e., two high years, two low years, and one middle year). No model captures the year-to-year ranking across summers but many capture one of the high years and in some cases that one of low years. CMAQ STAGE captures a second high year, whereas no other model captures this (or distinguish it from other years). Given variability within summer in the yearly observations (Fig. 1), future work should examine interannual variability in monthly averages to further establish model skill.

6 Conclusion

We introduce AQMEII4 Activity 2 for the intercomparison and evaluation of eighteen dry deposition schemes configured as single-point models driven by the same set of meteorological and environmental conditions at eight sites with ozone flux records. We provide our approach's rationale, document the single-point models, and describe the observational datasets used to drive and evaluate the models. The emphasis on driving models with a consistent set of inputs in Activity 2 allows us to focus on parameter and process uncertainty.

We launch the Activity 2 results by analyzing simulated multiyear mean ozone deposition velocities and effective conductances for plant stomata, cuticles, the lower canopy, and soil, as well as observed multiyear mean ozone deposition velocities. Our focus is monthly and seasonal averages across all hours of the day, apart from one site for which we examine afternoon averages (Ramat

Hanadiv). We evaluate the magnitudes and seasonal cycles (e.g., shape, amplitude) of simulated ozone deposition velocities against observations, and identify how differences and similarities in the relative and absolute contributions of individual deposition pathways and how some dependencies on environmental conditions influence the model spread and comparison with observations. We encourage future work to examine the roles of parameters, sensitivities, and transport related processes. For example, previous work shows that differences in deposition velocities among air quality models under stable conditions may at least in part be due to different empirical formulations of Monin-Obukhov Similarity Theory (Toyota et al., 2016).

There are a variety of observed climatological seasonal patterns and magnitudes of ozone deposition velocities across the sites. We emphasize that our measurement testbed is likely insufficient to generalize results to specific LULC types, so we focus on site-specific results. We also cannot discount the fact that differences in ozone flux methods and instrumentation and a lack of coordinated processing protocols across data sets limit meaningful synthesis of our results across sites. However, given that key processes and parameters are strongly tied to LULC type in dry deposition parameterizations, a core question is whether the magnitude and dependencies of ozone deposition velocities can be described from a LULC-type perspective. To address this question, future work will need to better understand observed site-to-site differences in ozone deposition velocities, which likely requires new multiscale ozone flux datasets.

We also emphasize incomplete understanding of observed variations in ozone deposition velocities at several sites. Namely, there are unexpectedly high ozone deposition velocities year-round at Auchencorth Moss, during the cool season at Ispra, and during the warm season at Borden Forest; models do not capture these high values. Further model evaluation at these sites requires better understanding of these features in the observations, and whether the models should capture them.

Observed interannual variation in ozone deposition velocities is strong at most sites examined here, demonstrating the importance of long-term ozone flux records for model evaluation. For example, even if a model captures values for a given year, the model may not reproduce interannual variability or the multiyear average. Our focus of this first paper is climatological evaluation, with the caveat that three sites (Ramat Hanadiv, Auchencorth Moss, and Bugacpuszta) do not have multiple years of data for several months and two are missing some months of data across all years. Of course, full annual records with several years of data are required for confident constraints on climatological seasonality. Nonetheless, sites with short-term records have very similar monthly averages between years when there is good data coverage, with only a few exceptions (October at Auchencorth Moss and fall at Ispra), implying some utility of these datasets towards our aim.

Despite the focus on climatological evaluation, for sites with more than three summers of data, we briefly identify whether models capture the ranking and spread across summers. We find that models do not capture observed summertime interannual variability, a finding that agrees with earlier work with one model at Harvard Forest (Clifton et al., 2017). Our work here shows that the issue is widespread across models and sites. Specifically, we show poor model skill in simulating the degree of the interannual spread as well as the ranking across years.

An important conclusion here is that individual model performance strongly varies by season and site. Throughout this paper, we examine individual models as well as model ensembles including the full set of models as well as the interquartile range, which helps us to narrow our focus to key common uncertainties across models. The interquartile range across simulated averages of ozone deposition velocities ranges from a factor of 1.2 to 1.9 annually across sites, and largely, reasonably bounds multiyear monthly mean ozone deposition velocities. Exceptions to the latter finding are times denoted as particularly uncertain at Auchencorth Moss, Ispra, and Borden Forest, in addition to late summer at Bugacpuszta and Ramat Hanadiv. The latter finding, together with our finding that many models that include soil moisture dependencies on stomatal conductance exaggerate late-summer decreases in ozone deposition velocities at forests, suggests a need to focus on refining soil moisture dependencies. Such work should probe interannual variability and seasonality with additional observational constraints on stomatal uptake in the context of uncertainty in soil moisture input data. In general, in some cases, gaps in site-specific measurement data (e.g., soil moisture and characteristics) forced us to make assumptions or derive estimates for key model variables and parameters. This may influence model performance, and points to a need for a standard minimum set of observations at future field studies.

Even beyond differing effects of soil moisture across the ensemble of models, there are differences in the shapes of the simulated seasonal cycles of ozone deposition velocities. Models that rely strongly on seasonally dependent parameters are often identified as outliers, so we recommend that related canopy resistance equations should be tied to variables like leaf area index instead of only seasonally varying parameters. In principle, seasonally varying parameters are not problematic, but a challenge seems to be indicating site-specific phenology accurately. At half the sites, the model spread is highest during cooler months, implying a need for better understanding of wintertime deposition processes. Strong wintertime sensitivities of tropospheric ozone abundances in regional-to-global chemical transport models (Helmig et al., 2007; Matichuk et al., 2017; Clifton et al., 2020b) also point to this need. By compositing observed and simulated ozone deposition velocities for all versus snowy conditions during cool months at sites with snow depth observations, we show that models' inability to capture the magnitude of wintertime values generally is a larger issue than models' inability to capturing responses to snow. While our analysis suggests that snow-induced changes are not the main driver of observed seasonality in ozone deposition velocities, we also find models may too strongly rely on leaf area index to determine seasonality.

Several papers illustrate challenges in determining which ozone dry deposition parameterization is best given observations compiled from the literature (Wong et al., 2019; Cao et al., 2022; Sun et al., 2022) or comparing seasonal differences for ozone and sulfur dioxide deposition velocities at Borden Forest (Wu et al., 2018). While we agree with these earlier findings with our more complete and diverse testbed, we take the evaluation a step further by pinpointing how different pathways contribute to the spread. In general, both stomatal and nonstomatal pathways are key drivers of variability in ozone deposition velocities across models. Additionally, in some cases, ozone deposition velocities are similar across models when the partitioning among deposition pathways is very different (i.e., similar results for different reasons).

For the most part, models simulate that stomatal uptake predominately drives seasonality in ozone deposition velocities. Like large model differences in seasonality of ozone deposition velocities, there are large model differences in seasonality of stomatal uptake. A few models show that seasonality in nonstomatal uptake terms is also important for seasonality in ozone deposition velocities. Across sites, both stomatal and nonstomatal pathways are important contributors to ozone deposition velocities during the growing season. For example, during summer, the median of the stomatal fraction of the ozone deposition velocity across models ranges from 30% to 55% across most sites. Thus, like observationally based estimates of stomatal fraction over physiologically active vegetation compiled by a recent review (Clifton et al., 2020a), models clearly indicate a codominant role for dry deposition through nonstomatal pathways. Nonetheless, as stated in the previous paragraph, we emphasize large differences in simulated nonstomatal uptake, in addition to stomatal uptake, across models.

In general, we confirm here with our unprecedented full documentation of eighteen dry deposition schemes that dry deposition schemes, especially nonstomatal deposition pathways, are highly empirical. While some schemes can capture some of the salient features of observations and schemes could be adjusted to better capture the magnitude of observed ozone deposition velocities at the sites examined here, better mechanistic understanding of observed variability, and a firm grasp on how different deposition pathways change in time and space on different scales, are needed to improve predictive ability of ozone dry deposition. We will continue to chip away at this problem; next for Activity 2 will be to leverage observation-based constraints on stomatal conductance, together with inferred stomatal fractions of ozone deposition velocities, and examine diel, seasonal, and interannual variations to further evaluate single-point models.

Data Availability

The hourly or half hourly observed ozone flux and forcing datasets are available to individuals wishing to participate in this effort on a password-protected site managed by the U.S. EPA, subject to the individual's agreement that the people who created and maintained the observation datasets are included in publications as the people see fit. Some datasets are already available publicly, and in these cases, we have included the references to the datasets in the text.

Author Contributions

O. E. C. lead the manuscript's direction and writing, data processing and analysis, and coordination among authors. D. S. and C. H. contributed to the manuscript's direction, data processing, and coordination among authors. J. O. B. contributed CMAQ STAGE results and documentation. S. B. contributed DO$_3$SE results and documentation. P. C. contributed GEM-MACH results and documentation. M. C. contributed data from Easter Bush and Auchencorth Moss. L. E. contributed DO$_3$SE results and documentation and assisted with direction. J. F. contributed IFS results and documentation and assisted with direction. E. F. contributed data from Ramat Hanadiv. S. G. assisted with direction. L. G. contributed MLC-CHEM results and documentation. O. G. contributed data from Ispra. C. D. H. assisted with direction and contributed GEOS-Chem results and documentation. I. G. contributed data from Ispra. L. H. contributed data from Bugacpuszta. V. H. contributed model results and documentation from

IFS. Q. L. contributed data from Ramat Hanadiv. P. A. M. contributed model results and documentation from GEM-MACH and assisted with direction. I. M. contributed data from Hyytiälä. G. M. contributed data from Ispra. J. W. M. contributed data from Harvard Forest. J. L. P. C. contributed WRF-Chem results and documentation. J. P. contributed M3Dry results and documentation. L. R. contributed M3Dry results and documentation. R. S. J. contributed WRF-Chem results and documentation. R. S. contributed data from Borden Forest. S. J. S. assisted with data processing and assisted with direction. S. S. and A. P. K. T contributed TEMIR results and documentation. E. T. contributed data from Ramat Hanadiv. T. V. contributed data from Hyytiälä. T. W. contributed data from Bugacpuszta. Z. W. and L. Z. contributed data from Borden Forest. All authors contributed to manuscript writing and useful discussions on data analysis and processing and results.

Acknowledgements

The views expressed in this article are those of the author(s) and do not necessarily represent the views or policies of the U.S. Environmental Protection Agency. Borden Forest Research Station is funded and operated by Environment and Climate Change Canada. For Easter Bush and Auchencorth Moss, we thank the field teams at and other UK CEH staff, as well as Ivan Simmons and Carole Helfter. Easter Bush measurements were funded by European Union projects GREENGRASS (EC EVK2-CT2001-00105), NitroEurope Integrated Project (contract no. 017841) and CarboEurope (contract no. GOCE-CT-2003-505572), and by the UK DEFRA 1/3/201 Effects of Ground Level Ozone on Vegetation in the UK and the UK NERC Core national capability. For Hyytiälä, we acknowledge Petri Keronen, Pasi Kolari, and Üllar Rannik. For Ispra, we acknowledge technical assistance from Carsten Gruening and Olga Pokorska. For Ramat Hanadiv, E. T. and E. F. acknowledge the Israel Science Foundation, Grant No. 1787/15, the Joseph H. and Belle R. Braun Senior Lectureship in Agriculture to E. T., and the crew at Ramat Hanadiv. Harvard Forest observations were supported in part by the U.S. Department of Energy, Office of Science (BER), and National Science Foundation Long-Term Ecological Research. O. E. C. acknowledges support from an appointment to the NASA Postdoctoral Program at the NASA Goddard Institute for Space Studies, administered by Oak Ridge Associated Universities under contract with NASA. C. D. H. was supported by the National Science Foundation (grant no. 1848372). I. M. and T. V. thank the Academy of Finland Flagship funding (grant no. 337549) and ICOS-Finland by University of Helsinki funding. L. H. and T. W. was partly supported by the National Research, Development and Innovation Office Grant K138176, ÉCLAIRE (Project Number 282910), and the FAIR Network of micrometeorological measurements COST Action (CA20108). D. DO$_3$SE runs performed by L. E. and S. B. were in part supported by a project grant (NE/V02020X/1) of the Future of UK Treescapes research program funded by the UKRI.

Competing Interests

None

References

Abramoff, R., and Finzi, A: Phenology and Carbon Allocation of Roots at Harvard Forest 2011-2013 version 3, Environmental Data Initiative, https://doi.org/10.6073/pasta/b545e796e37ecdf11fd7ff1275b41a12, 2019.

Ainsworth, E. A., Yendrek, C. R., Sitch, S., Collins, W. J., and Emberson, L. D.: The effects of tropospheric ozone on net primary productivity and implications for climate change, Annu. Rev. Plant Biol., 63(1), 637–661, https://doi.org/10.1146/annurev-arplant-042110-103829, 2012.

Altimir, N., Kolari, P., Tuovinen, J.-P., Vesala, T., Bäck, J., Suni, T., Kulmala, M., and Hari, P.: Foliage surface ozone deposition: A role for surface moisture?, Biogeosciences, 3, 209–228, https://doi.org/10.5194/bgd-2-1739-2005, 2006.

Ammann, C., Brunner, C., Spirig, A., and Neftel, A.: Technical note: Water vapour concentration and flux measurements with PTR-MS, Atmos. Chem. Phys., 6, 4643–4651, https://doi.org/10.5194/acp-6-4643-2006, 2006.

Anav, A., Proietti, C., Menut, L., Carnicelli, S., De Marco, A., and Paoletti, E.: Sensitivity of stomatal conductance to soil moisture: implications for tropospheric ozone, Atmos. Chem. Phys., 18, 5747–5763, https://doi.org/10.5194/acp-18-5747-2018, 2018.

Andersson, C., and Engardt, M.: European ozone in a future climate: Importance of changes in dry deposition and isoprene emissions, J. Geophys. Res., 115(D02303), https://doi.org/10.1029/2008JD011690, 2010.

Archibald, A. T., Neu, J. L., Elshorbany, Y. F., Cooper, O. R., Young, P. J., Akiyoshi, H., et al.: Tropospheric Ozone Assessment Report: A critical review of changes in the tropospheric ozone burden and budget from 1850 to 2100, Elem. Sci. Anth., 8, 1, https://doi.org/10.1525/elementa.2020.034, 2020.

Baldocchi, D. D., Hicks, B. B., and Camara, P.: A canopy stomatal resistance model for gaseous deposition to vegetated surfaces, Atmos. Environ., 21, 91–101, https://doi.org/10.1016/0004-6981(87)90274-5, 1987.

Bales, R., Valdez, M., and Dawson, G.: Gaseous deposition to snow 2. Physical-chemical model for SO_2 deposition, J. Geophys. Res., 92, 9789–9799, https://doi.org/10.1029/JD092iD08p09789, 1987.

Ball, M. C., Woodrow, I. E., and Berry, J. A.: A model predicting stomatal conductance and its contribution to the control of photosynthesis under different environmental conditions, in Progress in Photosynthesis Research, edited by: Biggins, J., Martinus Nijhoff Publishers, Dordrecht, Netherlands, 221–224, https://doi.org/10.1007/978-94-017-0519-6, 1987.

Barford, C. C., Wofsy, S. C., Goulden, M. L., Munger, J. W., Pyle, E. H., Urbanski, S. P., Hutyra, L., Saleska, S. R., Fitzjarrald, D., and Moore, K.: Factors controlling long- and short-term sequestration of atmospheric CO_2 in a mid-latitude forest, Science, 294, 1688–1691, https://doi.org/10.1126/science.1062962, 2001.

Baublitz, C. B., Fiore, A. M., Clifton, O. E., Mao, J., Li, J., Correa, G., Westervelt, D. M., Horowitz, L. W., Paulot, F., and Williams, A. P.: Sensitivity of Tropospheric Ozone Over the Southeast USA to Dry Deposition, Geophys. Res. Lett., 47(7), e2020GL087158, https://doi.org/10.1029/2020GL087158, 2020.

Beddows, A. V., Kitwiroon, N., Williams, M. L., and Beevers, S. D.: Emulation and sensitivity analysis of the community multiscale air quality model for a UK Ozone pollution episode, Environ. Sci. Tech., 51(11), 6229–6236, https://doi.org/10.1021/acs.est.6b05873, 2017.

Bela, M. M., Longo, K. M., Freitas, S. R., Moreira, D. S., Beck, V., Wofsy, S. C., Wiedemann, K., Andreae, M. O., and Artaxo, P.: Ozone production and transport over the Amazon Basin during the dry-to-wet and wet-to-dry transition seasons, Atmos. Chem. Phys., 15(2), 757–782, https://doi.org/10.5194/acp-15-757-2015, 2015.

Bonan, G. B., Lawrence, P. J., Oleson, K. W., Levis, S., Jung, M., Reichstein, M., Lawrence, D. M., and Swenson, S. C.: Improving canopy processes in the Community Land Model version 4 (CLM4) using global flux fields empirically inferred from FLUXNET data, J. Geophys. Res., 116, G02014, https://doi.org/10.1029/2010JG001593, 2011.

Boose, E., and Gould, E.: Shaler Meteorological Station at Harvard Forest 1964–2002, Harvard Forest Data Archive: HF000, https://doi.org/10.6073/pasta/84cf303ea3331fb47e8791aa61aa91b2, 1999.

Brook, J., Zhang, L., Franco, D., and Padro, J.: Description and evaluation of a model of deposition velocities for routine estimates of air pollutant dry deposition over North America, Part I: Model development, Atmos. Environ., 33, 5037–5051, https://doi.org/10.1016/S1352-2310(99)00250-2, 1999.

Campbell, G. S., and Norman, J. M.: An Introduction to Environmental Biophysics, Springer Sci. & Business Media, New York, ISBN: 978-1-4612-1626-1, 1998.

Cao, J., Chang, M., Pan, Y., Song, T., Liu, Z., Zhao, H., Zhou, M., Zhang, L., and Wang, X.: Assessment and intercomparison of ozone dry deposition schemes over two ecosystems based on Noah-MP in China, Atmos. Environ., 290, 119353, https://doi.org/10.1016/j.atmosenv.2022.119353, 2022.

Cape, J. N., Hamilton, R., and Heal, M. R.: Reactive uptake of ozone at simulated leaf surfaces: Implications for "non-stomatal" ozone flux, Atmos. Environ., 43(5), 1116–1123, https://doi.org/10.1016/j.atmosenv.2008.11.007, 2009.

Charusombat, U., Niyogi, D., Kumar, A., and Wang, X.: Evaluating a new deposition velocity module in the Noah land-surface model, Boundary-Layer Meteorol., 137(2), 271–290. https://doi.org/10.1007/s10546-010-9531-y, 2010.

Cionco, R. M.: Analysis of canopy index values for various canopy densities, Boundary-Layer Meteorol., 15, 81–93, https://doi.org/10.1007/BF00165507, 1978.

Clapp, R. B., and Hornberger, G. M.: Empirical equations for some soil hydraulic properties, Water Resour. Res., 14(4), 601– 604, https://doi.org/10.1029/WR014i004p00601, 1978.

Clifton, O. E., Fiore, A. M., Massman, W. J., Baublitz, C. B., Coyle, M., Emberson, L., Fares, S., Farmer, D. K., Gentine, P., Gerosa, G., Guenther, A. B., Helmig, D., Lombardozzi, D. L., Munger, J. W., Patton, E. G., Pusede, S. E., Schwede, D. B., Silva, S. J., Sörgel, M., Steiner, A. L., and Tai, A. P. K.: Dry deposition of ozone over land: processes, measurement, and modeling, Rev. Geophys., 58(1), e2019RG000670, https://doi.org/10.1029/2019RG000670, 2020a.

Clifton, O. E., Fiore, A. M., Munger, J. W., and Wehr, R.: Spatiotemporal controls on observed daytime ozone deposition velocity over northeastern U.S. forests during summer, J. Geophys. Res. Atmos., 124(10), 5612–5628, https://doi.org/10.1029/2018JD029073, 2019.

Clifton, O. E., Fiore, A. M., Munger, J. W., Malyshev, S., Horowitz, L. W., Shevliakova, E., Paulot, F., Murray, L. T., and Griffin, K. L.: Interannual variability in ozone removal by a temperate deciduous forest, Geophys. Res. Lett., 44, 542–552, https://doi.org/10.1002/2016GL070923, 2017.

Clifton, O. E., Patton, E. G., Wang, S., Barth, M., Orlando, J., and Schwantes, R. H.: Large Eddy Simulation for Investigating Coupled Forest Canopy and Turbulence Influences on Atmospheric Chemistry, J. Adv. Model. Earth Sys., 14(10), e2022MS003078, https://doi.org/10.1029/2022MS003078, 2022.

Clifton, O. E., Paulot, F., Fiore, A. M., Horowitz, L. W., Correa, G., Baublitz, C. B., Fares, S., Goded, I., Goldstein, A. H., Gruening, C., Hogg, A. J., Loubet, B., Mammarella, I., Munger, J. W., Neil, L., Stella, P., Uddling, J., Vesala T., and Weng, E.: Influence of dynamic ozone dry deposition on ozone pollution, J. Geophys. Res. Atmos., 125, e2020JD032398, https://doi.org/10.1029/2020JD032398, 2020b.

Coe, H., Gallagher, M. W., Choularton, T. W., and Dore, C.: Canopy scale measurements of stomatal and cuticular O_3 uptake by Sitka spruce, Atmos. Environ., 29(12), 1413–1423, https://doi.org/10.1016/1352-2310(95)00034-V, 1995.

806 Collatz, G. J., Ball, J. T., Grivet, C., and Berry, J. A.: Physiological and environmental regulation of stomatal conductance,
807 photosynthesis and transpiration: a model that includes a laminar boundary layer, Agric. For. Meteorol., 54(2–4), 107–136,
808 https://doi.org/10.1016/0168-1923(91)90002-8, 1991.
809
810 Collatz, G., Ribas-Carbo, M., and Berry, J.: Coupled Photosynthesis-Stomatal Conductance Model for Leaves of C_4 Plants, Funct.
811 Plant Biol., 19(5), 519–538, https://doi.org/10.1071/PP9920519, 1992.
812
813 Collineau, S., and Brunet, Y.: Detection of turbulent coherent motions in a forest canopy part II: Time-scales and conditional
814 averages, Boundary-Layer Meteorol., 66, 49–73, https://doi.org/10.1007/bf00705459, 1993.
815
816 Colorado State University, Soil Hydraulic Properties: https://biocycle.atmos.colostate.edu/shiny/soils/, last access: 8 June 2022.
817
818 Conklin, M. H., Sigg, A., Neftel, A., and Bales, R. C.: Atmosphere-snow transfer function for H_2O_2: microphysical considerations,
819 J. Geophys. Res., 98(D1), 18367–18376, https://doi.org/10.1029/93JD01194, 1993.
820
821 Cooter, E. J., and Schwede, D. B.: Sensitivity of the National Oceanic and Atmospheric Administration multilayer model to
822 instrument error and parameterization uncertainty, J. Geophys. Res., 105(D5), 6695–6707. https://doi.org/10.1029/1999JD901080,
823 2000.
824
825 Cosby, B. J., Hornberger, G. M., Clapp, R. B., Ginn, T. R.: A statistical exploration of the relationships of soil moisture
826 characteristics to the physical properties of soils, Water Resour. Res., 20(6), 682–690, https://doi.org/10.1029/WR020i006p00682,
827 1984.
828
829 Coyle, M., Nemitz, E., Storeton-West, R., Fowler, D., and Cape, J. N.: Measurements of ozone deposition to a potato canopy,
830 Agric. For. Meteorol., 149(3-4), 655–666, https://doi.org/10.1016/j.agrformet.2008.10.020, 2009.
831
832 Coyle, M.: The Gaseous Exchange of Ozone at Terrestrial Surfaces: Non-stomatal Deposition to Grassland, PhD Thesis, University
833 of Edinburgh, Edinburgh, 2006.
834
835 Dabberdt, W. F., Lenschow, D. H., Horst, T. W., Zimmerman, P. R., Oncley, S. P., and Delany, A. C.: Atmosphere-surface
836 exchange measurements, Science, 260, 1472–1481, https://doi.org/10.1126/science.260.5113.1472, 1993.
837
838 Davidson, E., and Savage, K.: Soil respiration, temperature and moisture at Harvard Forest EMS Tower since 1995, Harvard Forest
839 Data Archive: HF006, https://doi.org/10.6073/pasta/33ba3432103297fe0644de6e0898f91f, 1999.
840

858 Dentener, F., Drevet, J., Lamarque, J. F., Bey, I., Eickhout, B., Fiore, A. M., Hauglustaine, D., Horowitz, L. W., Krol, M.,
859 Kulshrestha, U. C., Lawrence, M., Galy-Lacaux, C., Rast, S., Shindell, D., Stevenson, D., Van Noije, T., Atherton, C., Bell, N.,
860 Bergman, D., Butler, T., Cofala, J., Collins, B., Doherty, R., Ellingsen, K., Galloway, J., Gauss, M., Montanaro, V., Müller, J. F.,
861 Pitari, G., Rodriguez, J., Sanderson, M., Solmon, F., Strahan, S., Schultz, M., Sudo, K., Szopa, S., and Wild, O.: Nitrogen and
862 sulfur deposition on regional and global scales: A multimodel evaluation, Global Biogeochem. Cy., 20(4), GB4003,
863 https://doi.org/10.1029/2005GB002672, 2006.
864

865 Echer, F. R., and Rosolem, C. A.: Cotton leaf gas exchange responses to irradiance and leaf aging, Biol. Plant., 59(2), 366–372,
866 https://doi.org/10.1007/s10535-015-0484-3, 2015.
867

868 El-Madany, T. S., Niklasch, K., and Klemm, O.: Stomatal and Non-Stomatal Turbulent Deposition Flux of Ozone to a Managed
869 Peatland, Atmosphere, 8, 175; https://doi.org/10.3390/atmos8090175, 2017.
870

871 Ellsworth, D. S., and Reich, P. B.: Canopy structure and vertical patterns of photosynthesis and related leaf traits in a deciduous
872 forest, Oecologia, 96, 169–178, https://doi.org/10.1007/BF00317729, 1993.
873

874 Emberson, L. D., Kitwiroon, N., Beevers, S., Büker, P., and Cinderby, S.: Scorched Earth: how will changes in the strength of the
875 vegetation sink to ozone deposition affect human health and ecosystems?, Atmos. Chem. Phys., 13(14), 6741–6755,
876 https://doi.org/10.5194/acp-13-6741-2013, 2013.
877

878 Emberson, L.: Effects of ozone on agriculture, forests and grasslands, Philos. Trans. Royal Soc. A, 378(2183),
879 https://doi.org/10.1098/rsta.2019.0327, 2020.
880

881 Emerson, E. W., Katich, J. M., Schwarz, J. P., McMeeking, G. R., and Farmer, D. K.: Direct measurements of dry and wet
882 deposition of black carbon over a grassland, J.Geophy. Res. Atmos., 123, 12,277–12,290, https://doi.org/10.1029/2018JD028954,
883 2018.
884

885 Erisman, J. W., van Pul, A., and Wyers, P.: Parameterization of dry deposition mechanisms for the quantification of atmospheric
886 input to ecosystems, Atmos. Environ., 28(16), 2595–2607, https://doi.org/10.1016/1352-2310(94)90433-2, 1994.
887

888 Fares, S., Conte, A., and Chabbi, A.: Ozone flux in plant ecosystems: new opportunities for long-term monitoring networks to
889 deliver ozone-risk assessments, Environ. Sci. Pollut. Res., 25, 8240–8248, https://doi.org/10.1007/s11356-017-0352-0, 2018.
890

Fares, S., Savi, F., Muller, J., Matteucci, G., and Paoletti, E.: Simultaneous measurements of above and below canopy ozone fluxes help partitioning ozone deposition between its various sinks in a Mediterranean Oak Forest, Agric. For. Meterol., 198-199, 181–191, https://doi.org/10.1016/j.agrformet.2014.08.014, 2014.

Farmer, D. K., Boedicker, E. K., and DeBolt, H. M.: Dry Deposition of Atmospheric Aerosols: Approaches, Observations, and Mechanisms, Ann. Rev. Phys. Chem., 72, 16.1–16.23, https://doi.org/10.1146/annurev-physchem-090519- 034936, 2021.

Farquhar, G. D., von Caemmerer, S., and Berry, J. A.: A biochemical model of photosynthetic CO_2 assimilation in leaves of C_3 species, Planta, 149(1), 78–90, https://doi.org/10.1007/BF00386231, 1980.

Ferrara, R. M., Tommasi, P. D., Famulari, D., and Rana, G.: Limitations of the eddy covariance system in measuring low ammonia fluxes, Boundary-Layer Meteorol., 180, 173-186, https://doi.org/10.1007/s10546-021-00612-6, 2021.

Ferréa, C., Zenone, T., Comolli, R., and Seufert, G.: Estimating heterotrophic and autotrophic soil respiration in a semi-natural forest of Lombardy, Italy, Pedobiologia, 55(6), 285–294, http://dx.doi.org/10.1016/j.pedobi.2012.05.001, 2012.

Finco, A., Coyle, M., Nemitz, E., Marzouli, R., Chiesa, M., Loubet, B., Fares, S., Diaz-Pines, E., Gasche, R., and Gerosa, G.: Characterization of ozone deposition to a mixed oak-hornbeam forest – flux measurements at five levels above and inside the canopy and their interactions with nitric oxide, Atmos. Chem. Phys., 18(24), 17945–17961, https://doi.org/10.5194/acp-18-17945-2018, 2018.

Fischer, L., Breitenlechner, M., Canaval, E., Scholz, M., Graus, M., Karl, T.G., Petäjä, T., Kulmala, M., and Hansel, A.: First eddy covariance fluxes measurements of semi-volatile organic compounds with the PTR3-TOF-MS, Atmos. Meas.Tech., 14(12), 8019–8039, https://doi.org/10.5194/amt-14-8019-2021, 2021.

Fitzjarrald, D., and Sakai, R.: Measurements at Harvard Forest EMS Tower 1991-2007, Harvard Forest Data Archive: HF102 (v.22), Environmental Data Initiative, https://doi.org/10.6073/pasta/673330eb6a4e045fbc89d8e862b2c920, 2009.

Flechard, C. R., Nemitz, E., Smith, R. I., Fowler, D., Vermeulen, A. T., Bleeker, A., Erisman, J. W., Simpson, D., Zhang, L., Tang, Y. S., and Sutton, M. A.: Dry deposition of reactive nitrogen to European ecosystems: A comparison of inferential models across the NitroEurope network, Atmos. Chem. Phys., 11(6), 2703–2728, https://doi.org/10.5194/acp-11-2703-2011, 2011.

Foken, T., Göockede, M., Mauder, M., Mahrt, L., Amiro, B., and Munger, W.: Post-field data quality control, in: Handbook of Micrometeorology, Springer, Dordrecht, 181–208, https://doi.org/10.1007/1-4020-2265-4_9, 2004.

946 Fowler, D., Flechard, C., Cape, J.N. Storeton-West, R. L., and Coyle, M.: Measurements of Ozone Deposition to Vegetation
947 Quantifying the Flux, the Stomatal and Non-Stomatal Components, Water Air Soil Pollut., 130(1-4), 63–74,
948 https://doi.org/10.1023/A:1012243317471, 2001.

950 Fowler, D., Pilegaard, K., Sutton, M. A., Ambus, P., Raivonen, M., Duyzer, J., Simpson, D., Fagerli, H., Fuzzi, S., Schjoerring, J.
951 K., Granier, C., Neftel, A., Isaksen, I. S. A., Laj, P., Maione, M., Monks, P. S., Burkhardt, J., Daemmgen, U., Neirynck, J.,
952 Personne, E., Wichink Kruit, R. J., Butterbach-Bahl, K., Flechard, C., Tuovinen, J. P., Coyle, M., Gerosa, G. Loubet, B., Altimir,
953 N., Gruenhage, L., Ammann, C., Cieslik, S., Paoletti, E., Mikkelsen, T. N., Ro-Poulsen, H., Cellier, P., Cape, J. N., Horvath, L.,
954 Loreto, F., Niinemets, U., Palmer, P. I., Rinne, J., Misztal, P., Nemitz, E., Nilsson, D., Pryor, S., Gallagher, M. W., Vesala, T.,
955 Skiba, U., Brueggemann, N., Zechmeister-Boltenstern, S., Williams, J., O'Dowd, C., Facchini, M. C., de Leeuw, G., Flossman,
956 A., Chaumerliac, N., and Erisman, J. W.: Atmospheric composition change: Ecosystems- atmosphere interactions, Atmos.
957 Environ., 43(33), 5193–5267, https://doi.org/10.1016/j.atmosenv.2009.07.068, 2009.

959 Froelich, N., Croft, H., Chen, J. M., Gonsamo, A., and Staebler, R. M.: Trends of carbon fluxes and climate over a mixed temperate–
960 boreal transition forest in southern Ontario, Canada, Agric. For. Meterol., 211-212, 72–84,
961 https://doi.org/10.1016/j.agrformet.2015.05.009, 2015.

963 Fuentes, J. D., and Gillespie, T. J.: A gas exchange system to study the effects of leaf surface wetness on the deposition of ozone,
964 Atmos. Environ., 26A(6), 1165–1173, https://doi.org/10.1016/0960-1686(92)90048-P, 1992.

966 Fuentes, J. D., Gillespie, T. J., den Hartog, G., and Neumann, H. H.: Ozone deposition onto a deciduous forest during dry and wet
967 conditions, Agric. For. Meteorol., 62, 1–18, https://doi.org/10.1016/0168-1923(92)90002-L, 1992.

969 Fulgham, S. R., Brophy, P., Link, M., Ortega, J., Pollack, I., and Farmer, D. K.: Seasonal Flux Measurements over a Colorado
970 Pine Forest Demonstrate a Persistance Source of Organic Acids, ACS Earth Space Chem., 3, 9, 2017–2032,
971 https://doi.org/10.1021/acsearthspacechem.9b00182, 2019.

973 Fuller, E. N, Schettler, P. D., and Giddings, J. C.: A new method for prediction of binary gas phase diffusion coefficients, Ind.
974 Eng. Chem., 53, 19–27, https://doi.org/10.1021/ie50677a007, 1966.

976 Fumagalli, I., Gruening, C., Marzuoli, R., and Cieslik, S.: Long-term measurements of NO_x and O_3 soil fluxes in a temperate
977 deciduous forest, Agric. For. Meteorol., 228-229, 205–216, https://doi.org/10.1016/j.agrformet.2016.07.011, 2016.

979 Galmarini, S., Bianconi, R., Klug, W., Mikkelsen, T., Addis, R., Andronopoulos, S., et al.: Ensemble dispersion forecasting—Part
980 I: concept, approach and indicators, Atmos. Environ., 38(28), 4607–4617, https://doi.org/10.1016/j.atmosenv.2004.05.030, 2004.

Galmarini, S., Makar, P., Clifton, O., Hogrefe, C., Bash, J., Bianconi, R., Bellasio, R., Bieser, J., Butler, T., Ducker, J., Flemming, J., Hozdic, A., Holmes, C., Kioutsioukis, I., Kranenburg, R., Lupascu, A., Perez-Camanyo, J. L., Pleim, J., Ryu, Y.-H., San Jose, R., Schwede, D., Silva, S., Garcia Vivanco, M., and Wolke, R.: Technical Note – AQMEII4 Activity 1: Evaluation of Wet and Dry Deposition Schemes as an Integral Part of Regional-Scale Air Quality Models, Atmos. Chem. Phys., 21, 15663–15697, https://doi.org/10.5194/acp-21-15663-2021, 2021.

Ganzeveld, L., and Lelieveld, J.: Dry deposition parameterization in a chemistry general circulation model and its influence on the distribution of reactive trace gases, J. Geophys. Res., 100, 20999–21012, https://doi.org/10.1029/95jd02266, 1995.

Ganzeveld, L., Bouwman, L., Stehfest, E., van Vuuren, D., Eickhout, B., and Lelieveld, J.: Impacts of future land cover changes on atmospheric chemistry-climate interactions, J. Geophys. Res., 115, https://doi.org/10.1029/2010JD014041, 2010.

Ganzeveld, L., Lelieveld, J., and Roelofs, G. J.: A dry deposition parameterization for sulfur oxides in a chemistry and general circulation model, J. Geophys. Res. Atmos., 103, 5679–5694, https://doi.org/10.1029/97JD03077, 1998.

Gao, W., Shaw, R. H., and Paw, U. K. T.: Observation of organized structure in turbulent flow within and above a forest canopy, Boundary-Layer Meteorol., 47, 349–377, https://doi.org/10.1007/BF00122339, 1989.

Garratt, J. R.: The Atmospheric Boundary Layer, Cambridge University Press, Cambridge, Great Britain, 316 pp, 1992.

Gerosa, G. A., Marzuoli, R., and Finco, A.: Interannual variability of ozone fluxes in a broadleaf deciduous forest in Italy, Elem. Sci. Anth., 10(1), https://doi.org/10.1525/elementa.2021.00105, 2022.

Global Modeling and Assimilation Office (GMAO): MERRA-2 tavg1_2d_flx_Nx: 2d,1-Hourly,Time-Averaged,Single-Level,Assimilation,Surface Flux Diagnostics V5.12.4 (M2T1NXFLX), Greenbelt, MD, USA: Goddard Space Flight Center Distributed Active Archive Center (GSFC DAAC), Last access: 1 July 2020, https://doi.org/10.5067/7MCPBJ41Y0K6, 2015.

Godowitch, J. M.: Vertical ozone fluxes and related deposition parameters over agricultural and forested landscapes, Boundary-Layer Meteorol., 50, 375–404, https://doi.org/10.1007/BF00120531, 1990.

Goldstein, A. H., McKay, M., Kurpius, M. R., Schade, G. W., Lee, A., Holzinger, R., and Rasmussen, R. A.: Forest thinning experiment confirms ozone deposition to forest canopy is dominated by reaction with biogenic VOCs, Geophys. Res. Lett., 31, L22106, https://doi.org/ 10.1029/2004GL021259, 2004.

Gong, C., Liao, H., Yue, X., Ma, Y., and Lei, Y.: Impacts of Ozone-Vegetation Interactions on Ozone Pollution Episodes in North China and the Yangtze River Delta, Geophys. Res. Lett., 48(12), e2021GL093814, https://doi.org/10.1029/2021GL093814, 2021.

Grulke, N. E., and Heath, R. L.: Ozone effects on plants in natural ecosystems, Plant Biology, 22(S1), 12–37, https://doi.org/10.1111/plb.12971, 2019.

Grünzweig, J. M., Navon, Y., Kanas, D., Dirks, I., and Dumbur, R.: Study of major processes in the biogeochemical cycles of the Phillyrea latifolia shrubland in Ramat Hanadiv, Final Research Report, The Hebrew University of Jerusalem and Ramat Hanadiv, Israel, 2010.

Guarin, J. R., Emberson, L., Simpson, D., Hernandez-Ochoa, I. M., Rowland, D., and Asseng, S.: Impacts of tropospheric ozone and climate change on Mexico wheat production, Clim. Change, 155(2), 157–174, https://doi.org/10.1007/s10584-019-02451-4, 2019.

Guenther, A., Kulmala, M., Turnipseed, A., Rinne, J., Suni, T., and Reissell, A.: Integrated land ecosystem-atmosphere processes study (iLEAPS) assessment of global observational networks, Boreal Environ. Res., 16(4), 321–336, 2011.

Güsten, H., and Heinrich, G.: On-line measurements of ozone surface fluxes. 1. Methodology and instrumentation, Atmos. Environ., 30(6), 897–909, https://doi.org/10.1016/1352-2310(95)00269-3, 1996.

Güsten, H., Heinrich, G., Schmidt, R. W. H., and Schurath, U.: A novel ozone sensor for direct eddy flux measurements, J. Atmos. Chem., 14, 73–84, https://doi.org/10.1007/BF00115224, 1992.

Hannun, R. A., Swanson, A. K., Bailey, S. A., Hanisco, T. F., Bui, T. P., Bourgeois, I., Peischl, J., and Ryerson, T. B.: A cavity-enhanced ultraviolet absorption instrument for high-precision, fast-time-response ozone measurements, Atmos. Meas. Tech., 13, 6877–6887, https://doi.org/10.5194/amt-13-6877-2020, 2020.

Hardacre, C., Wild, O., and Emberson, L.: An evaluation of ozone dry deposition in global scale chemistry climate models, Atmos. Chem. Phys., 15(11), 6419–6436, https://doi.org/10.5194/acp-15-6419-2015, 2015.

He, C., Clifton, O., Felker-Quinn, E., Fulgham, S. R., Juncosa Calahorrano, J. F., Lombardozzi, D., Purser, G., Riches, M., Schwantes, R., Tang, W., Poulter, B., and Steiner, A. L.: Interactions between Air Pollution and Terrestrial Ecosystems: Perspectives on Challenges and Future Directions, Bull. Am. Meteorol. Soc., 102(3), E525–E538, https://doi.org/10.1175/BAMS-D-20-0066.1, 2021.

Helmig, D., Cohen, L. D., Bocquet, F., Oltmans, S., Grachev, A., and Neff, W.: Spring and summertime diurnal surface ozone fluxes over the polar snow at Summit, Greenland, Geophys. Res. Lett., 36, L08809, https://doi.org/10.1029/2008gl036549, 2009.

Helmig, D., Ganzeveld, L., Butler, T., and Oltmans, S. J.: The role of ozone atmosphere-snow gas exchange on polar, boundary-layer tropospheric ozone – a review and sensitivity analysis, Atmos. Chem. Phys., 7, 15–30, 2007.

Hicks, B. B., Kolb, C. E., and Lenschow, D. H.: New opportunities for flux measurement, in: Global tropospheric chemistry: Chemical fluxes in the global atmosphere, edited by Lenschow, D. H., and Hicks, B. B., National Center for Atmospheric Research, Boulder, CO, 83–85, 1989.

Hogrefe, C., Liu, P., Pouliot, G., Mathur, R., Roselle, S., Flemming, J., Lin, M., and Park, R. J.: Impacts of different characterizations of large-scale background on simulated regional-scale ozone over the continental United States, Atmos. Chem. Phys., 18(5), 3839–3864, https://doi.org/10.5194/acp-18-3839-2018, 2018.

Högström, U.: Non-dimensional wind and temperature profiles in the atmospheric surface layer: A re-evaluation, Boundary Layer Meteorol., 42, 55–78, https://doi.org/10.1007/BF00119875, 1988.

Hong, C., Mueller, N. D., Burney, J. A., Zhang, Y., AghaKouchak, A., Moore, F. C., Qin, Y., Tong, D., and Davis, S. J.: Impacts of ozone and climate change on yields of perennial crops in California, Nat. Food, 1, 166–172, https://doi.org/10.1038/s43016-020-0043-8, 2020.

Horváth, L., Koncz, P., Móring, A., Nagy, Z., Pintér, K., and Weidinger, T.: An attempt to partition stomatal and non-stomatal ozone deposition parts on a short grassland, Boundary-Layer Meteorol., 167(2), 303–326, https://doi.org/10.1007/s10546-017-0310-x, 2018.

Huang, L., McDonald-Buller, E. C., McGaughey, G., Kimura, Y., and Allen, D. T.: The impact of drought on ozone dry deposition over eastern Texas, Atmos. Environ., 127, 176–186, https://doi.org/10.1016/j.atmosenv.2015.12.022, 2016.

Huang, M., Crawford, J. H., Carmichael, G. R., Bowman, K. W., Kumar, S. V., and Sweeney, C.: Satellite soil moisture data assimilation impacts on modeling weather variables and ozone in the southeastern US – Part 2: Sensitivity to dry-deposition parameterizations, Atmos. Chem. Phys., 22(11), 7461–7487, https://doi.org/10.5194/acp-22-7461-2022, 2022.

Hubert, M., and Vandervieren, E.: An Adjusted Boxplot for Skewed Distributions, Comput. Stat. Data Anal., 52(12), 5186–5201, https://doi.org/10.1016/j.csda.2007.11.008, 2008.

Moved down [67]: Baldocchi, D.

Moved up [55]: R.: A

¶

Moved (insertion) [68]

Moved (insertion) [69]

Moved (insertion) [70]

Moved up [69]: Hong, C., Mueller, N. D., Burney, J. A., Zhang, Y., AghaKouchak, A., Moore, F. C., Qin, Y., Tong, D., and Davis, S. J.: Impacts of ozone and climate change on

Moved up [70]: J.: Impacts of ozone and climate change on yields of perennial crops in California,

Moved up [68]: Högström, U.: Non-dimensional wind and temperature profiles in the atmospheric surface layer: A re-evaluation, Boundary Layer Meteorol., 42, 55–78, https://doi.org/10.1007/BF00119875, 1988.¶
¶

Huthwelker, T., Ammann, M., and Peter, T.: The Uptake of Acidic Gases on Ice, Chem. Rev., 106, 1375–1444, https://doi.org/10.1021/cr020506v, 2006.

Ilvesniemi, H., Levula, J., Ojansuu, R., Kolari, P., Kulmala, L., Pumpanen, J., Launiainen, S., Vesala, T., and Nikinmaa, E.: Long-term measurements of the carbon balance of a boreal Scots pine dominated forest ecosystem, Boreal Env. Res., 14, 731–753, 2009.

Iqbal, M., An Introduction to Solar Radiation, Academic Press, 386 pp., ISBN: 9780323151818, 1983.

Jarvis, P. G.: The interpretation of the variations in leaf water potential and stomatal conductance found in canopies in the field, Philos. Trans. R. Soc. Lond. B Biol. Sci., 273, 593–610, https://doi.org/10.1098/rstb.1976.0035, 1976.

Jensen, N. O., and Hummelshøj, P.: Derivation of canopy resistance for water vapour fluxes over a spruce forest, using a new technique for the viscous sublayer resistance, Agric. For. Meteorol., 73, 339–352, https://doi.org/10.1016/0168-1923(94)05083-I, 1995.

Jensen, N. O., and Hummelshøj, P.: Derivation of canopy resistance for water vapor fluxes over a spruce forest, using a new technique for the viscous sublayer resistance (correction to vol. 73, pp. 339, 1995), Agric. For. Meteorol, 85(3-4), 289, https://doi.org/10.1016/S0168-1923(97)00024-5, 1997.

Jones, S. K., Helfter, C., Anderson, M., Coyle, M., Campbell, C., Famulari, D., Di Marco, C., van Dijk, N., Tang, Y. S., Topp, C. F. E., Kiese, R., Kindler, R., Siemens, J., Schrumpf, M., Kaiser, K., Nemitz, E., Levy, P. E., Rees, R. M., Sutton, M. A., and Skiba, U. M.: The nitrogen, carbon and greenhouse gas budget of a grazed, cut and fertilised temperate grassland, Biogeosciences, 14(8), 2069–2088, https://doi.org/10.5194/bg-14-2069-2017, 2017.

Kanamitsu, M., Ebisuzaki, W., Woollen, J., Yang, S.-K., Hnilo, J. J., Fiorino, M., and Potter, G. L.: NCEP-DOE AMIP-II Reanalysis (R-2), Bull. Am. Meteorol. Soc., 83, 1631–1643, https://doi.org/10.1175/BAMS-83-11-1631, 2002.

Kaplan, M.: The soils of Ramat Hanadiv, Society for the Protection of Nature in Israel, Tel-Aviv, 1989.

Karl, T., Harley, T., Emmons, L., Thornton, B., Guenther, A., Basu, C., Turnipseed, A., and Jardine, K.: Efficient Atmospheric Cleansing of Oxidized Organic Trace Gases by Vegetation, Science, 330, 816–819, https://doi.org/10.1126/science.1192534, 2010.

Kattge, J., Knorr, W., Raddatz, T., and Wirth, C.: Quantifying photosynthetic capacity and its relationship to leaf nitrogen content for global-scale terrestrial biosphere models, Glob. Chan. Biol. 15, 976–991, https://doi.org/10.1111/j.1365-2486.2008.01744.x, 2009.

Kavassalis, S. C., and Murphy, J. G.: Understanding ozone-meteorology correlations: A role for dry deposition, Geophys. Res. Lett., 44(6), 2922–2931, https://doi.org/10.1002/2016GL071791, 2017.

Keronen, P., Reissell, A., Rannik, Ü., Pohja, T., Siivola, E., Hiltunen, V., Hari, P., Kulmala, M., and Vesala, T.: Ozone flux measurements over a Scots pine forest using eddy covariance method: performance evaluation and comparison with flux-profile method, Boreal Env. Res., 8, 425–443, 2003.

Knauer, J., El-Madany, T.S., Zaehle, S., and Migliavacca, M.: Bigleaf-An R package for the calculation of physical and physiological ecosystem properties from eddy covariance data, PLoS ONE, 13(8), e0201114, https://doi.org/10.1371/journal.pone.0201114, 2018.

Kolari, P., Pumpanen, J., Kulmala, L., Ilvesniemi, H., Nikinmaa, E., Grönholm, T., and Hari, P.: Forest floor vegetation plays an important role in photosynthetic production of boreal forests, For. Ecol. Manag., 221, 241–248, https://doi.org/10.1016/j.foreco.2005.10.021, 2006.

Koncz, P., Besnyői, V., Csathó, A. I., Nagy, J., Szerdahelyi, T., Tóth, Z. S., Pintér, K., Balogh, J, Nagy, Z, and Bartha, S.: Effect of grazing and mowing on the microcoenological composition of semi-arid grassland in Hungary, Appl. Ecol. Environ. Res., 12(2), 563–575, 2014.

Krupa, S. V.: Effects of atmospheric ammonia (NH_3) on terrestrial vegetation: A review, Environ. Pollut., 124(2), 179–221, https://doi.org/10.1016/s0269-7491(02)00434-7, 2003.

Kurpius, M. R., and Goldstein, A. H.: Gas-phase chemistry dominates O_3 loss to a forest, implying a source of aerosols and hydroxyl radicals to the atmosphere, Geophys. Res. Lett., 30(7), https://doi.org/10.1029/2002GL016785, 2003.

Lam, J. C. Y., Tai, A. P. K., Ducker, J. A., and Holmes, C. D.: Development of an ecophysiology module in the GEOS-Chem chemical transport model version 12.2.0 to represent biosphere–atmosphere fluxes relevant for ozone air quality, Geosci. Model Dev., 16, 2323–2342, https://doi.org/10.5194/gmd-16-2323-2023, 2023.

Launiainen, S., Katul, G. G., Grönholm, T., and Vesala, T.: Partitioning ozone fluxes between canopy and forest floor by measurements and a multi-layer model, Agric. For. Meteorol., 173, 85–99, https://doi.org/10.1016/j.agrformet.2012.12.009, 2013.

Le Morvan-Quéméner, A., Coll, I., Kammer, J., Lamaud, E., Loubet, B., Personne, E., and Stella, P.: Impact of parameterization choices on the restitution of ozone deposition over vegetation, Atmos. Environ., 178, 49–65, https://doi.org/10.1016/j.atmosenv.2018.01.003, 2018.

Leith, F. I., Garnett, M. H., Dinsmore, K. J., Billett, M. F., and Heal, K. V.: Source and age of dissolved and gaseous carbon in a peatland-riparian-stream continuum: A dual isotope (14C and 14C) analysis, Biogeochemistry, 119, 415–433, https://doi.org/10.1007/s10533-014-9977-y, 2014.

Lenschow, D. H., Pearson, R. Jr., and Stankov, B. B.: Estimating the ozone budget in the boundary layer by use of aircraft measurements of ozone eddy flux and mean concentration, J. Geophys. Res., 86(C8), 7291–7297, https://doi.org/10.1029/JC086iC08p07291, 1981.

Letts, M. G., Roulet, N. T., Comer, N. T., Skarupa, M. R., and Verseghy, D. L.: Parametrization of peatland hydraulic properties for the Canadian Land Surface Scheme, Atmos.-Ocean, 38(1), 141–160, https://doi.org/10.1080/07055900.2000.9649643, 2000.

Leuning R.: A critical appraisal of a combined stomatal-photosynthesis model for C3 plants, Plant Cell Environ., 18(4), 339–355, https://doi.org/10.1111/j.1365-3040.1995.tb00370.x, 1995.

Leuning, R., Dunin, F.X., and Wang, Y.-P.: A two-leaf models for canopy conductance, photosynthesis and partitioning of available energy II. Comparison with measurements. Agric. For. Meteorol. 91(1-3), 113–125, https://doi.org/10.1016/S0168-1923(98)00074-4, 1998.

Leuning, R.: Modelling stomatal behaviour and photosynthesis of Eucalyptus grandis, Aust. J. Plant Physiol., 17, 159–175, http://hdl.handle.net/102.100.100/257808?index=1, 1990.

Li, Q., Gabay, M., Rubin, Y., Fredj, E., and Tas, E.: Measurement-based investigation of ozone deposition to vegetation under the effects of coastal and photochemical air pollution in the Eastern Mediterranean, Sci. Tot. Environ., 645, 1579–1597, https://doi.org/10.1016/j.scitotenv.2018.07.037, 2018.

Li, Q., Gabay, M., Rubin, Y., Raveh-Rubin, S., Rohatyn, S., Tatarinov, F., Rotenberg, E., Ramati, E., Dicken, U., Preisler, Y., Fredj, Yakir, D., and Tas, E.: Investigation of ozone deposition to vegetation under warm and dry conditions near the Eastern Mediterranean coast, Sci. Tot. Environ., 658, 1316–1333, https://doi.org/10.1016/j.scitotenv.2018.12.272, 2019.

Li, S. M., Anlauf, K. G., and Wiebe, H. A.: Heterogeneous nighttime production and deposition of particle nitrate at a rural site in North America during summer 1988, J. Geophys. Res., 98, 5139–5157, https://doi.org/10.1029/92JD02523, 1993.

Li, Y., Schichtel, B. A., Walker, J. T., Schwede, D. B., Chen, X., Lehmann, C. M. B., Puchalski, M. A., Gay, D. A., and Collett, J. L.: Increasing importance of deposition of reduced nitrogen in the United States, Proc. Natl. Acad. Sci. U.S.A., 113(21), 5874–5879, https://doi.org/10.1073/pnas.1525736113, 2016.

Lin, M., Horowitz, L. W., Xie, Y., Paulot, F., Malyshev, S., Shevliakova, E., Finco, A., Gerosa, G., Kubistin, D., and Pilegaard, K.: Vegetation feedbacks during drought exacerbate ozone air pollution extremes in Europe, Nat. Clim., 10, 444–451, https://doi.org/10.1038/s41558-020-0743-y, 2020.

Liu, Z., Doherty, R. M., Wild, O., O'Connor, F. M., and Turnock, S. T.: Correcting ozone biases in a global chemistry–climate model: implications for future ozone, Atmos. Chem. Phys., 22(18), 12543–12557, https://doi.org/10.5194/acp-22-12543-2022, 2022.

Lombardozzi, D., Levis, S., Bonan, G., Hess, P. G., and Sparks, J. P.: The influence of chronic ozone exposure on global carbon and water cycles, J. Clim., 28, 292–305, https://doi.org/10.1175/Jcli-D-14-00223.1, 2015.

Lombardozzi, D., Sparks, J. P., and Bonan, G.: Integrating O_3 influences on terrestrial processes: Photosynthetic and stomatal response data available for regional and global modeling, Biogeosciences, 10(11), 6815–6831, https://doi.org/10.5194/bg-10-6815-2013, 2013.

Machon, A., Horváth, L., Weidinger, T., Grosz, B., Móring, A., and Führer, E.: Measurement and modeling of N-balance between atmosphere and biosphere over a grazed grassland (Bugacpuszta) in Hungary, Water Air Soil Pollut., 226(27), https://doi.org/10.1007/s11270-014-2271-8, 2015.

Mahrt, L., Lenschow, D. H., Sun, J., Weil, J. C., MacPherson, J. I., and Desjardins, R. L.: Ozone fluxes over a patchy cultivated surface, J. Geophys. Res., 100(D11), 23125–23131, https://doi.org/10.1029/95JD02599, 1995.

Makar, P. A., Akingunola, A., Aherne, J., Cole, A. S., Aklilu, Y., Zhang, J., Wong, I., Hayden, K., Li, S.-M., Kirk, J., Scott, K., Moran, M. D., Robichaud, A., Cathcart, H., Baratzedah, P., Pabla, B., Cheung, C., Zheng, Q., and Jeffries, D. S.: Estimates of exceedances of critical loads for acidifying deposition in Alberta and Saskatchewan, Atm. Chem. Phys., 18, 9897–9927, https://doi.org/10.5194/acp-18-9897-2018, 2018.

Massad, R.-S., Nemitz, E., and Sutton, M.A.: Review and parameterization of bi-directional ammonia exchange between vegetation and the atmosphere, Atmos. Chem. Phys., 10(21), 10359–10386, https://doi.org/10.5194/acp-10-10359-2010, 2010.

Massman, W. J.: A review of the molecular diffusivities of H_2O, CO_2, CH_4, CO, O_3, SO_2, NH_3, N_2O, NO, and NO_2 in air, O_2 and N_2 near STP, Atmos. Environ., 32(6), 1111–1127, https://doi.org/10.1016/s1352-2310(97)00391-9, 1998.

Massman, W. J.: Toward an ozone standard to protect vegetation based on effective dose: a review of deposition resistances and a possible metric, Atmos. Environ., 38(15), 2323–2337, https://doi.org/10.1016/j.atmosenv.2003.09.079, 2004.

Matichuk, R., Tonnesen, G., Luecken, D., Gilliam, R., Napelenok, S. L., Baker, K. R., Schwede, D., Murphy, B., Helmig, D., Lyman, S. N., and Roselle, S.: Evaluation of the community multiscale air quality model for simulating winter ozone formation in the Uinta Basin, J. Geophys. Res. Atmos, 122(24), 13,545–13,572, https://doi.org/10.1002/2017JD027057, 2017.

Mauder, M., and Foken, T.: Documentation and Instruction Manual of the Eddy-Covariance Software Package TK3 (update). Universität Bayreuth, Abt. Mikrometeorologie, 68 p., ISSN 1614-8924, 2015.

Mauder, M., Foken, T., Clement, R., Elbers, J. A., Eugster, W., Grünwald, T., Heusinkveld, B., and Kolle, O.: Quality control of CarboEurope flux data – Part 2: Inter-comparison of eddy-covariance software, Biogeosciences, 5, 451–462, https://doi.org/10.5194/bg-5-451-2008, 2008.

Mauzerall, D. L., and Wang, X: Protecting agricultural crops from the effects of tropospheric ozone exposure: reconciling science and standard setting in the United States, Europe, and Asia, Ann. Rev. Energy Environ., 26, 237–268, https://doi.org/10.1146/annurev.energy.26.1.237, 2001.

McGrath, J. M., Betzelberger A. M., Wang, S., Shook, E., Zhu, X. G., Long, S. P., and Ainsworth, E. A.: An analysis of ozone damage to historical maize and soybean yields in the United States, Proc. Natl. Acad. Sci. U.S.A., 112, 14390–14395, https://doi.org/10.1073/pnas.1509777112, 2015.

McRae, G. J.: Mathematical Modeling of Photochemical Air Pollution, Ph.D. Thesis, California Institute of Technology, Pasadena, California, https://doi.org/10.7907/n8p7-f149, 1981.

Medlyn, B. E., Duursma, R. A., Eamus, D., Ellsworth, D. S., Prentice, I. C., Barton, C. V. M., Crous, K. Y., de Angelis, P., Freeman, M., and Wingate, L.: Reconciling the optimal and empirical approaches to modelling stomatal conductance, Global Change Biol., 17, 2134–2144, https://doi.org/10.1111/j.1365-2486.2010.02375.x, 2011.

Mészáros, R., Horváth, L., Weidinger, T., Neftel, A., Nemitz, E., Dämmgen, U., Cellier, P., and Loubet, B.: Measurement and modelling ozone fluxes over a cut and fertilized grassland, Biogeosciences, 6(10), 1987–1999, https://doi.org/10.5194/bg-6-1987-2009, 2009.

Meyers, T. P., Finkelstein, P., Clarke, J., Ellestad, T. G., and Sims, P. F.: A multilayer model for inferring dry deposition using standard meteorological measurements, J. Geophys. Res., 103(D7), 22645–22661, https://doi.org/10.1029/98JD01564, 1998.

Meyers, T. P.: The sensitivity of modeled SO_2 fluxes and profiles to stomatal and boundary layer resistances, Water Air Soil Pollut., 35, 261–278, https://doi.org/10.1007/BF00290935, 1987.

Michou, M., Laville, P., Serc, D., Fotiadi, A., Bouchouc, P., and Peuch, V.-H.: Measured and modeled dry deposition velocities over the ESCOMPTE area, Atmos. Res., 74, 89–116, https://doi.org/10.1016/j.atmosres.2004.04.011, 2004.

Milford, C.: Dynamics of atmospheric ammonia exchange with intensively-managed grassland, PhD Thesis, University of Edinburgh, Edinburgh, 2004.

Muller, J. B., Coyle, M., Fowler, D., Gallagher, M. W., Nemitz, E. G., and Percival, C. J.: Comparison of ozone fluxes over grassland by gradient and eddy covariance technique, Atmos. Sci. Lett., 10(3), 164–169, https://doi.org/10.1002/asl.226, 2009.

Muller, J. B., Percival, C. J., Gallagher, M. W., Fowler, D., Coyle, M., and Nemitz, E.: Sources of uncertainty in eddy covariance ozone flux measurements made by dry chemiluminescence fast response analyzers, Atmos. Meas. Tech., 3, 163–176, https://doi.org/10.5194/amt-3-163-2010, 2010.

Munger, J. W., and Wofsy, S.: Canopy-atmosphere exchange of carbon, water and energy at Harvard Forest EMS Tower since 1991, Harvard Forest Data Archive: HF004, https://doi.org/10.6073/pasta/dd9351a3ab5316c844848c3505a8149d, 1999.

Munger, J. W., Wofsy, S. C., Bakwin, P. S., Fan, S.-M., Goulden, M. L., Daube, B. C., Goldstein, A. H., Moore, K. E., and Fitzjarrald, D. R.: Atmospheric deposition of reactive nitrogen oxides and ozone in a temperate deciduous forest and a subarctic woodland 1. Measurements and mechanisms, J. Geophys. Res., 101(D7), 12639–12657, https://doi.org/10.1029/96JD00230, 1996.

Munger, W., and Wofsy, S.: Biomass Inventories at Harvard Forest EMS Tower since 1993 version 34, Environmental Data Initiative. https://doi.org/10.6073/pasta/92143fc1a5a68864dc2ef99152aa4300, 2021.

Nemitz, E., Milford, C., and Sutton, M. A.: A two-layer canopy compensation point model for describing bi-directional biosphere-atmosphere exchange of ammonia, Q. J. Roy. Meteor. Soc., 127, 815–833, https://doi.org/10.1002/qj.49712757306, 2001.

Nguyen, T. B., Crounse, J. D., Teng, A. P., Clair, J. M. S., Paulot, F., Wolfe, G. M., and Wennberg, P. O.: Rapid deposition of oxidized biogenic compounds to a temperate forest, Proc. Natl. Acad. Sci. U.S.A., 112(5), E392–E401, https://doi.org/10.1073/pnas.141870211, 2015.

NOAA Global Monitoring Laboratory: Trends in Atmospheric Carbon Dioxide: https://gml.noaa.gov/ccgg/trends/, last access: 31 August 2022

Norman, J. M.: Biometeorology in Integrated Pest Management, New York: Elsevier, ISBN: 9780323147965, 1982.

Norman, J. M.: Modeling the complete crop canopy, in: Modification of the Aerial Environment of Crops, edited by: Barfield, B. J., and Gerber, J. F., Am. Soc. of Agric. Eng., St. Joseph, Michigan, 249–280, ISBN: 09-161-50151, 1979.

Novak, G. A., Vermeuel, M. P., and Bertram, T. H.: Simultaneous detection of ozone and nitrogen dioxide by oxygen anion chemical ionization mass spectrometry: a fast-time-response sensor suitable for eddy covariance measurements, Atmos. Meas. Tech., 13, 1887–1907, https://doi.org/10.5194/amt-13-1887-2020, 2020.

Oleson, K. W., Lawrence, D. M., Bonan, G. B., Drewniak, B., Huang, M., Koven, C. D., Levis, S., Li, F., Riley, W. J., Subin, Z. M., Swenson, S. C., Thornton, P. E., Bozbiyik, A., Fisher, R., Heald, C. L., Kluzek, E., Lamarque, J.-F., Lawrence, P. J., Leung, L. R., Lipscomb, W., Muszala, S., Ricciuto, D. M., Sacks, W., Sun, Y., Tang, J., and Yang, Z.-L.: Technical description of version 4.5 of the Community Land Model (CLM), NCAR Earth System Laboratory – Climate and Global Dynamics Division, Boulder, Colorado, USA, Tech. Rep. TN-503+STR, http://www.cesm.ucar.edu/models/cesm1.2/clm/ CLM45_Tech_Note.pdf (last access: 03 January 2022), 2013.

Oliver, R. J., Mercado, L. M., Sitch, S., Simpson, D. M., Medlyn, B. E., Lin, Y., and Folberth, G. A.: Large but decreasing effect of ozone on the European carbon sink, Biogeosciences, 4245–4269, https://doi.org/10.5194/bg-15-4245-2018, 2018.

Otu-Larbi, F., Conte, A., Fares, S., Wild, O., and Ashworth, K.: FORCAsT-gs: Importance of Stomatal Conductance Parameterization to Estimated Ozone Deposition Velocity, J. Adv. Model. Earth Syst., 13(9), e2021MS002581, https://doi.org/10.1029/2021MS002581, 2021.

Papp, M., Fóti, S., Nagy, Z., Pintér, K., Posta, K., Fekete, S., Csintalan, Z., and Balogh, J.: Rhizospheric, mycorrhizal and heterotrophic respiration in dry grasslands, Eur. J. Soil Biol., 85, 43–52, https://doi.org/10.1016/J.EJSOBI.2018.01.005, 2018.

Patton, E. G., and Finnigan, J. J.: Canopy turbulence, in Handbook of Environmental Fluid Dynamics, edited by: H. J. S. Fernando, CRC Press/Taylor & Francis Group, Boca Raton, 311–327, 2013.

Paulot, F., Malyshev, S., Nguyen, T., Crounse, J. D., Shevliakova, E., and Horowitz, L. W.: Representing sub-grid scale variations in nitrogen deposition associated with land use in a global Earth system model: implications for present and future nitrogen

deposition fluxes over North America, Atmos. Chem. Phys., 18(24), 17963–17978, https://doi.org/10.5194/acp-18-17963-2018, 2018.

Perry, R. H., and Green, D. W.: Chemical Engineering Handbook, 6th ed., 2240 pp, McGraw-Hill, New York, 1984.

Pleim, J. E., and Xiu, A.: Development and testing of a surface flux and planetary boundary layer model for application in mesoscale models, J. Appl. Meteorol., 34, 16–32, https://doi.org/10.1175/1520-0450-34.1.16, 1995.

Phillips, G. J., Pouvesle, N., Thieser, J., Schuster, G., Axinte, R., Fischer, H., Williams, J., Lelieveld, J., and Crowley, J. N.: Peroxyacetyl nitrate (PAN) and peroxyacetic acid (PAA) measurements by iodide chemical ionisation mass spectrometry: first analysis of results in the boreal forest and implications for the measurement of PAN fluxes, Atmos. Chem. Phys., 13, 1129–1139, https://doi.org/10.5194/acp-13-1129-2013, 2013.

Pleim, J., and Ran, L.: Surface Flux Modeling for Air Quality Applications, Atmosphere, 2(3), 271–302, https://doi.org/10.3390/atmos2030271, 2011.

Potempski, S., and Galmarini, S.: Est modus in rebus: analytical properties of multi-model ensembles, Atmos. Chem. Phys., 9(24), 9471–9489, https://doi.org/10.5194/acp-9-9471-2009, 2009.

Potier, E., Loubet, B., Durand, B., Flura, D., Bourdat-Deschamps, M., Ciuraru, R., and Ogée, J.: Chemical reaction rates of ozone in water infusions of wheat, beech, oak and pine leaves of different ages, Atmos. Environ., 151, 176–187, https://doi.org/10.1016/j.atmosenv.2016.11.069, 2017.

Potier, E., Ogée, J., Jouanguy, J., Lamaud, E., Stella, P., Personne, E., Durand, B., Mascher, N., and Loubet, B: Multilayer modelling of ozone fluxes on winter wheat reveals large deposition on wet senescing leaves, Agric. For. Meteorol., 211-212, 58–71, https://doi.org/10.1016/j.agrformet.2015.05.006, 2015.

Putaud, J. P., Bergamaschi, P., Bressi M., Cavalli, F., Cescatti, A., Daou, D., Dell'Acqua, A., Douglas, K., Duerr, M., Fumagalli, I., Goded, I., Grassi, F., Gruening, C., Hjorth, J., Jensen, N. R., Lagler, F., Manca, G., Martins Dos Santos, S., Matteucci, M., Passarella, R., Pedroni, V., Pokorska, O., and Roux, D.: JRC – Ispra Atmosphere – Biosphere – Climate Integrated monitoring Station 2013 Report, EUR 26995 EN, https://doi.org/10.2788/926761, 73-93, 2014.

Ramsay, R., Di Marco, C. F., Heal, M. R., Twigg, M. M., Cowan, N., Jones, M. R., Leeson, S. R., Bloss, W. J., Kramer, L. J., Crilley, L., Sörgel, M., Andreae, M., and Nemitz, E.: Surface–atmosphere exchange of inorganic water-soluble gases and associated ions in bulk aerosol above agricultural grassland pre- and postfertilisation, Atmos. Chem. Phys., 18, 16953–16978, https://doi.org/10.5194/acp-18-16953-2018, 2018.

Ran, L., Pleim, J., Song, C., Band, L., Walker, J. T., and Binkowski, F. S.: A photosynthesis-based two-leaf canopy stomatal conductance model for meteorology and air quality modeling with WRF/CMAQ PX LSM, J. Geophys. Res. Atmos., 122(3), 1930–1952, https://doi.org/10.1002/2016JD025583, 2017.

Rannik, Ü., Altimir, N., Mammarella, I., Bäck, J., Rinne, J., Ruuskanen, T. M., Hari, P., Vesala, T., and Kulmala, M.: Ozone deposition into a boreal forest over a decade of observations: Evaluating deposition partitioning and driving variables, Atmos. Chem. Phys., 12(24),12165–12182, https://doi.org/10.5194/acp-12-12165-2012, 2012.

Rannik, Ü., Mammarella, I., Keronen, P., and Vesala, T.: Vertical advection and nocturnal deposition of ozone over a boreal pine forest, Atmos. Chem. Phys., 9(6), 2089–2095, https://doi.org/10.5194/acp-9-2089-2009, 2009.

Rao, S. T., Galmarini, S., and Puckett, K.: Air Quality Model Evaluation International Initiative (AQMEII): advancing the state of the science in regional photochemical modeling and its applications, Bull. Am. Meteorol. Soc., 92(1), 23–30, https://doi.org/10.1175/2010BAMS3069.1, 2011.

Raupach, M. R.: Anomalies in flux-gradient relationships over forest, Boundary-Layer Meteorol., 16, 467–486, https://doi.org/10.1007/bf03335385, 1979.

Ren, W., Tian, H., Liu, M., Zhang, C., Chen, G., Pan, S., Felzer, B., and Xu, X.: Effects of tropospheric ozone pollution on net primary productivity and carbon storage in terrestrial ecosystems of China, J. Geophys. Res. Atmos., 112(D22S9), https://doi.org/10.1029/2007JD008521, 2007.

Repola J.: Biomass equations for Scots pine and Norway spruce in Finland, Silva Fennica, 43(4), https://doi.org/10.14214/sf.184, 2009.

Ronda, R., De Bruin, H., and Holtslag, A.: Representation of the canopy conductance in modeling the surface energy budget for low vegetation, J. Appl. Meteorol., 40, 1431–1444, https://doi.org/10.1175/1520-0450(2001)040<1431:ROTCCI>2.0.CO;2, 2001.

Rondón, A., Johansson, C., and Granat, L.: Dry deposition of nitrogen dioxide and ozone to coniferous forests, J. Geophys. Res., 98(D3), 5159–5172, https://doi.org/10.1029/92JD0233, 1993.

Ryan, E. and Wild, O.: Calibrating a global atmospheric chemistry transport model using Gaussian process emulation and ground-level concentrations of ozone and carbon monoxide, Geosci. Model Dev., 14, 5373–5391, https://doi.org/10.5194/gmd-14-5373-2021, 2021.

Sabbatini, S., Mammarella, I., Arriga, N., Fratini, G., Graf, A., Hörtnagl, L., Ibrom, A., Longdoz, B., Mauder, M., Merbold, L., and Metzger, S.: Eddy covariance raw data processing for CO_2 and energy fluxes calculation at ICOS ecosystem stations, Int. Agrophys., 32(4), 495–515, https://doi.org/10.1515/intag-2017-0043, 2018.

Savage, K. E., and Davidson, E. A.: Interannual variation of soil respiration in two New England forests, Global Biogeochem. Cy., 15(2), 337–350, https://doi.org/10.1029/1999gb001248, 2001.

Schaller, C., Hofer, B., and Klemm, O.: Greenhouse gas exchange of a NW German peatland, 18 years after rewetting, J. Geophys. Res., 127(2), e2020JG005960. https://doi.org/10.1029/2020JG005960, 2022.

Schobesberger, S., D'Ambro, E. L., Vettikkat, L., Lee, B. H., Peng, Q., Bell, D. M., Shilling, J. E., Shrivastava, M., Pekour, M., Fast, J., and Thornton, J. A.: Airborne flux measurements of ammonia over the southern Great Plains using chemical ionization mass spectrometry, Atmos. Meas. Tech., 16, 247–271, https://doi.org/10.5194/amt-16-247-2023, 2023.

Schuepp, P. H.: Turbulent transfer at the ground: On verification of a simple predictive model, Boundary-Layer Meteorol., 12, 171–186, https://doi.org/10.1007/BF0012197, 1977.

Schwede, D., Zhang, L., Vet, R., and Lear, G.: An intercomparison of the deposition models used in the CASTNET and CAPMoN networks, Atmos. Environ., 45(6), 1337–1346, https://doi.org/10.1016/j.atmosenv.2010.11.050, 2011.

Sharkey, T. D., Bernacchi, C. J., Farquhar, G. D., and Singsaas, E. L.: Fitting photosynthetic carbon dioxide response curves for C_3 leaves. Plant Cell Environ., 30(9), 1035–1040, 2007.

Sharma, A., Ojha, N., Ansari, T. U., Sharma, S. K., Pozzer, A., and Gunthe, S. S.: Effects of dry deposition on surface ozone over South Asia inferred from a regional chemical transport model, ACS Earth Space Chem., 4(2), 321–327, https://dx.doi.org/10.1021/acsearthspacechem.0c00004, 2020.

Shuttleworth, W. J., and Wallace, J. S.: Evaporation from sparse crops – an energy combination theory, Q. J. Roy. Meteor. Soc., 111, 839–855, https://doi.org/10.1002/qj.49711146510, 1985.

Silva, S. J., and Heald, C. L.: Investigating dry deposition of ozone to vegetation, J. Geophys. Res. Atmos., 123, 559–573, https://doi.org/10.1002/2017JD027278, 2018.

580 Silva, S. J., Heald, C. L., Ravela, S., Mammarella, I., and Munger, J. W.: A deep learning parameterization for ozone dry deposition
581 velocities, Geophys. Res. Lett., 46, 983–989, https://doi.org/10.1029/2018GL081049, 2019.

582

583 Simpson, D., Benedictow, A., Berge, H., Bergström, R., Emberson, L. D., Fagerli, H., Flechard, C. R., Hayman, G. D., Gauss, M.,
584 Jonson, J. E., Jenkin, M. E., Nyíri, A., Richter, C., Semeena, V. S., Tsyro, S., Tuovinen, J.-P., Valdebenito, Á., and Wind, P.: The
585 EMEP MSC-W chemical transport model – technical description, Atmos. Chem. Phys., 12(6), 7825–7865,
586 https://doi.org/10.5194/acp-12-7825-2012, 2012.

587

588 Sitch, S., Cox, P. M., Collins, W. J., and Huntingford, C.: Indirect radiative forcing of climate change through ozone effects on the
589 land-carbon sink, Nature, 448, 791–794, https://doi.org/10.1038/nature06059, 2007.

590

591 Slevin, D., Tett, S. F. B., and Williams, M.: Multi-site evaluation of the JULES land surface model using global and local data,
592 Geosci. Model Dev., 8, 295–316, https://doi.org/10.5194/gmd-8-295-2015, 2015.

593

594 Solazzo, E., and Galmarini, S.: A science-based use of ensembles of opportunities for assessment and scenario studies, Atmos.
595 Chem. Phys., 15(5), 2535–2544, https://doi.org/10.5194/acp-15-2535-2015, 2015.

596

597 Solberg, S., Hov, Ø., Søvdee, A., Isaksen, I. S. A., Coddevillee, P., De Backer, H., Forster, C., Orsolini, Y., and Uhse, K., European
598 surface ozone in the extreme summer 2003, J. Geophys. Res., 113, D07307, https://doi.org/10.1029/2007JD009098, 2008.

599

600 Song, C., Katul, G., Oren, R., Band, L. E., Tague, C. L., Stoy, P. C., and McCarthy, H. R.: Energy, water, and carbon fluxes in a
601 loblolly pinestand: Results from uniform and gappy canopy models with comparisons to eddy flux data, J. Geophys. Res., 114,
602 G04021, https://doi.org/10.1029/2009JG000951, 2009.

603

604 Steiner, A. L., Pressley, S. N., Botros, A., Jones, E., Chung, S. H., and Edburg, S. L.: Analysis of coherent structures and
605 atmosphere-canopy coupling strength during the CABINEX field campaign, Atmos. Chem. Phys., 11(23), 11921–11936, https://
606 doi.org/10.5194/acp-11-11921-2011, 2011.

607

608 Stella, P., Loubet, B., de Berranger, C., Charrier, X., Ceschia, E., Gerosa, G., Lamaud, F. E., Serça, D., George, C., and Ciuraru,
609 R.: Soil ozone deposition: Dependence of soil resistance to soil texture, Atmos. Environ., 119, 202–209,
610 https://doi.org/10.1016/j.atmosenv.2018.11.036, 2019.

611

612 Stella, P., Loubet, B., Lamaud, E., Laville, P., and Cellier, P.: Ozone deposition onto bare soil: A new parameterization, Agric.
613 For. Meteorol., 151(6), 669–681, https://doi.org/10.1016/j.agrformet.2011.01.015, 2011.
614

Sun, S., Moravek, A., Trebs, I., Kesselmeier, J., and Sörgel, M.: Investigation of the influence of liquid surface films on O_3 and PAN deposition to plant leaves coated with organic/inorganic solution, J. Geophys. Res. Atmos., 121(23), 14239–14256, https://doi.org/10.1002/2016JD025519, 2016a.

Sun, S., Moravek, A., von der Heyden, L., Held, A., Sörgel, M., and Kesselmeier, J.: Twin-cuvette measurement technique for investigation of dry deposition of O_3 and PAN to plant leaves under controlled humidity conditions, Atmos. Meas. Tech., 9(2), 599–617, https://doi.org/10.5194/amt-9-599-2016, 2016b.

Sun, S., Tai, A. P. K., Yung, D. H. Y., Wong, A. Y. H., Ducker, J. A., and Holmes, C. D.: Influence of plant ecophysiology on ozone dry deposition: comparing between multiplicative and photosynthesis-based dry deposition schemes and their responses to rising CO_2 level, Biogeosciences, 19(6), 1753–1776, https://doi.org/10.5194/bg-19-1753-2022, 2022.

Tai, A. P. K., Sadiq, M., Pang, J. Y. S., Yung, D. H. Y., and Feng, Z. Z.: Impacts of Surface Ozone Pollution on Global Crop Yields: Comparing Different Ozone Exposure Metrics and Incorporating Co-effects of CO2, Front. Sustain. Food Syst., 5, 534616, https://doi.org/10.3389/fsufs.2021.534616, 2021.

Tan, J., Fu, J. S., Dentener, F., Sun, J., Emmons, L., Tilmes, S., Sudo, K., Flemming, J., Jonson, J. E., Gravel, S., Bian, H., Davila, Y., Henze, D. K., Lund, M. T., Kucsera, T., Takemura, T., and Keating, T.: Multi-model study of HTAP II on sulfur and nitrogen deposition, Atmos. Chem. Phys., 18(9), 6847–6866, https://doi.org/10.5194/acp-18-6847-2018, 2018.

Tang, W., Cohan, D. S., Morris, G. A., Byun, D. W., and Luke, W. T.: Influence of vertical mixing uncertainties on ozone simulation in CMAQ, Atmos. Environ., 45, 2898–2909, https://doi.org/10.1016/j.atmosenv.2011.01.057, 2011.

Tebaldi, C., and Knutti, R.: The use of the multi-model ensemble in probabilistic climate projections, Phil. Trans. R. Soc. A., 365, 2053–2075, https://doi.org/10.1098/rsta.2007.2076, 2007.

Thomas, C., and Foken, T.: Flux contribution of coherent structures and its implications for the exchange of energy and matter in a tall spruce canopy, Boundary-Layer Meteorol., 123, 317–337, https://doi.org/10.1007/s10546-006-9144-7, 2007.

Toyota, K., Dastoor, A. P., and Ryzhkov, A.: Parameterization of gaseous dry deposition in atmospheric chemistry models: Sensitivity to aerodynamic resistance formulations under statically stable conditions, Atmos. Environ., 147, 409–422, http://dx.doi.org/10.1016/j.atmosenv.2016.09.055, 2016.

Moved up [81]: Steiner, A. L., Pressley, S. N., Botros, A., Jones, E., Chung, S. H., and Edburg, S. L.: Analysis of coherent structures and atmosphere-canopy coupling strength during the CABINEX field campaign, Atmos. Chem.

Deleted: Phys., 11, 11921–11936, https://doi.org/10.5194/acp-11-11921-2011, 2011.¶

Deleted: ,

Deleted: ,

Deleted: ¶

Moved up [71]: Tai, A.

Deleted: P., Val Martin, M., and Heald, C. L.: Threat to future global food security from climate change and ozone air pollution, Nat. Clim. Change, 4, 817, https://doi.org/10.1038/nclimate2317, 2014.¶

Deleted: ,

Travis, K. R., and Jacob, D. J.: Systematic bias in evaluating chemical transport models with maximum daily 8 h average (MDA8) surface ozone for air quality applications: A case study with GEOS-Chem v9.02., Geosci. Model Dev., 12(8), 3641–3648, https://doi.org/10.5194/gmd-12-3641-2019, 2019.

U.S. EPA: Integrated Science Assessment for Oxides of Nitrogen, Oxides of Sulfur, and Particulate Matter – Ecological Criteria, Document EPA/600/R-20/278, Center for Public Health and Environmental Assessment, U.S. Environmental Protection Agency, Research Triangle Park, North Carolina, 2020b.

U.S. EPA: Integrated Science Assessment for Ozone and Related Photochemical Oxidants, Document EPA/600/R-20/012, Center for Public Health and Environmental Assessment, U.S. Environmental Protection Agency, Research Triangle Park, North Carolina, 2020a.

Urbanski, S., Barford, C., Wofsy, S., Kucharik, C., Pyle, E., Budney, J., McKain, K., Fitzjarrald, D., Czikowsky, M., and Munger, J. W.: Factors controlling CO_2 exchange on timescales from hourly to decadal at Harvard Forest, J. Geophys. Res., 112, G02020, https://doi.org/10.1029/2006jg000293, 2007.

USDA, Soil Texture Calculator: https://www.nrcs.usda.gov/wps/portal/nrcs/detail/soils/survey/?cid=nrcs142p2_054167, last access: 8 June 2022.

Vautard, R., Honore, C., Beekmann, M., and Rouil, L.: Simulation of ozone during the August 2003 heat wave and emission control scenarios, Atmos. Environ., 39, 2957–2967, https://doi.org/10.1016/j.atmosenv.2005.01.039, 2005.

Vermeuel, M. P., Cleary, P. A., Desai, A. R., and Bertram, T. H.: Simultaneous measurements of O_3 and HCOOH vertical fluxes indicate rapid in-canopy terpene chemistry enhances O_3 removal over mixed temperate forests, Geophys. Res. Lett., 48(3), e2020GL090996, https://doi.org/10.1029/2020GL090996, 2021.

Vermeuel, M. P., Novak, G. A., Kilgour, D. B., Claflin, M. S., Lerner, B. M., Trowbridge, A. M., Thom, J., Cleary, P. A., Desai, A. R., and Bertram, T. H.: Observations of biogenic volatile organic compounds over a mixed temperate forest during the summer to autumn transition, Atmos. Chem. Physics., 23, 4123–4148, https://doi.org/10.5194/acp-23-4123-2023, 2023.

Verry, E. S., Bay, R. R., and Boelter, D. H.: Physical properties of organic soils, in: Peatland biogeochemistry and watershed hydrology at the Marcell Experimental Forest, edited by: Kolka, R. K., Sebestyen, S. D., Verry, E. S., and Brooks, K. N., CRC Press, New York, 1–13, ISBN 9780429130007, 2011.

Vesala, T., Suni, T. Rannik, Ü., Keronen, P., Markkanen, T., Sevanto, S., Grönholm, T., Smolander, S., Kulmala, M., Ilvesniemi, H., Ojansuu, R., Uotila, A., Levula, J., Mäkelä, A., Pumpanen, J., Kolari, P., Kulmala, L., Altimir, N., Berninger, F., Nikinmaa,

718 E., and Hari, P.: Effect of thinning on surface fluxes in a boreal forest, Global Biogeochem. Cy., 19(GB2001),
719 https://doi.org/10.1029/2004GB002316, 2005.

721 Visser, A. J., Ganzeveld, L. N., Goded, I., Krol, M. C., Mammarella, I., Manca, G., and Boersma, F. K.: Ozone deposition impacts
722 assessments for forest canopies require accurate ozone flux partitioning on diurnal timescales, Atmos. Chem. Phys., 12(24), 18393–
723 18411, https://doi.org/10.5194/acp-21-18393-2021, 2021.

725 Vivanco, M. G., Theobald, M. R., García-Gómez, H., Garrido, J. L., Prank, M., Aas, W., Adani, M., Alyuz, U., Andersson, C.,
726 Bellasio, R., Bessagnet, B., Bianconi, R., Bieser, J., Brandt, J., Briganti, G., Cappelletti, A., Curci, G., Christensen, J. H., Colette,
727 A., Couvidat, F., Cuvelier, C., D'Isidoro, M., Flemming, J., Fraser, A., Geels, C., Hansen, K. M., Hogrefe, C., Im, U., Jorba, O.,
728 Kitwiroon, N., Manders, A., Mircea, M., Otero, N., Pay, M.-T., Pozzoli, L., Solazzo, E., Tsyro, S., Unal, A., Wind, P., and
729 Galmarini, S.: Modeled deposition of nitrogen and sulfur in Europe estimated by 14 air quality model systems: evaluation, effects
730 of changes in emissions and implications for habitat protection, Atmos. Chem. Phys., 18, 10199–10218,
731 https://doi.org/10.5194/acp-18-10199-2018, 2018.

733 Voldner, E. C., Barrie, L. A., and Sirois, A.: A literature review of dry deposition of oxides of sulphur and nitrogen with emphasis
734 on long-range transport modelling in North America, Atmos. Environ., 20, 2101–2123, https://doi.org/10.1016/0004-
735 6981(86)90305-7, 1986.

737 von Caemmerer, S., and Farquhar, G. D.: Some relationships between the biochemistry of photosynthesis and the gas exchange of
738 leaves, Planta, 153(4), 376–387, https://doi.org/10.1007/BF00384257, 1981.

740 Walker, T. W.: Applications of adjoint modelling in chemical composition: Studies of tropospheric ozone at middle and high
741 northern latitudes, PhD thesis, Univ. of Toronto, Toronto, Canada, https://hdl.handle.net/1807/65764, 2014.

743 Walmsley, P., and Wesely, M.: Modification of coded parametrizations of surface resistances to gaseous dry deposition, Atmos.
744 Environ., 30(7), 1181–1188, https://doi.org/10.1016/1352-2310(95)00403-3, 1996.

745 Wang, Y., Jacob, D. J., and Logan, J. A.: Global simulation of tropospheric O_3-NO_x-hydrocarbon chemistry: 1. Model
746 formulation, J. Geophys. Res., 103(D9), 10713–10725, https://doi.org/10.1029/98JD00158, 1998.

748 Wesely, M. L., and Hicks, B. B.: A review of the current status of knowledge on dry deposition, Atmos. Environ., 34, 2261–2282,
749 https://doi.org/10.1016/S1352-2310(99)00467-7, 2000.

751 Wesely, M. L., and Hicks, B. B.: Some factors that affect the deposition rates of sulphur dioxide and similar gases on vegetation,
752 J. Air Pollut. Control Assoc., 27(11), 1110–1116, https://doi.org/10.1080/00022470.1977.10470534, 1977.

Wesely, M. L.: Parameterization of surface resistances to gaseous dry deposition in regional-scale numerical models, Atmos. Environ., 23(6), 1293–1304, https://doi.org/10.1016/0004-6981(89)90153-4, 1989.

Wild, O.: Modelling the tropospheric ozone budget: Exploring the variability in current models, Atmos. Chem. Phys., 7, 2643–2660, https://doi.org/10.5194/acp-7-2643-2007, 2007.

Wolfe, G. M., Hanisco, T. F., Arkinson, H. L., Bui, T. P., Crounse, J. D., Dean-Day, J., Goldstein, A., Guenther, A., Hall, S. R., Huey, G., Jacob, D. J., Karl, T., Kim, P. S., Liu, X., Marvin, M. R., Mikoviny, T., Miszta, P. K., Nguyen, T. B., Peischl, J., Pollack, I., Ryerson, T., St. Clair, J. M., Teng, A., Travis, K. R., Ullmann, K., Wennberg, P. O., and Wisthaler, A.: Quantifying sources and sinks of reactive gases in the lower atmosphere using airborne flux observations, Geophys. Res. Lett., 42(19), 8231–8240, https://doi.org/10.1002/2015GL065839, 2015.

Wolfe, G. M., Thornton, J. A., McKay, M., and Goldstein, A. H.: Forest-atmosphere exchange of ozone: sensitivity to very reactive biogenic VOC emissions and implications for in-canopy photochemistry, Atmos. Chem. Phys., 11(15), 7875–7891, https://doi.org/10.5194/acp-11-7875-2011, 2011.

Wong, A. Y. H., Geddes, J. A., Ducker, J. A., Holmes, C. D., Fares, S., Goldstein, A. H., Mammarella, I., and Munger, J. W.: New evidence for the importance of non-stomatal pathways in ozone deposition during extreme heat and dry anomalies, Geophys. Res. Lett., 49(8), e2021GL095717, https://doi.org/10.1029/2021GL095717, 2022.

Wong, A. Y. H., Geddes, J. A., Tai, A. P. K., and Silva, S. J.: Importance of dry deposition parameterization choice in global simulations of surface ozone, Atmos. Chem. Phys., 19, 14365–14385, https://doi.org/10.5194/acp-19-14365-2019, 2019.

Wu Z., Schwede D. B., Vet R., Walker J. T., Shaw M., Staebler R., and Zhang L.: Evaluation and intercomparison of five North American dry deposition algorithms at a mixed forest site, J. Adv. Model. Earth Syst., 10(7), 1571–1586, https://doi.org/10.1029/2017MS001231, 2018.

Wu, Z. Y., Zhang, L., Wang, X. M., and Munger, J. W.: A modified micrometeorological gradient method for estimating O_3 dry depositions over a forest canopy, Atmos. Chem. Phys., 15(13), 7487–7496, https://doi.org/ 10.5194/acp-15-7487-2015, 2015.

Wu, Z., Staebler, R., Vet, R., and Zhang, L.: Dry deposition of O_3 and SO_2 estimated from gradient measurements above a temperate mixed forest, Environ. Pollut., 202–210, https://doi.org/10.1016/j.envpol.2015.11.052, 2016.

836 Xin, Q., Dai, Y., and Liu, X.: A simple time-stepping scheme to simulate leaf area index, phenology, and gross primary production

837 across deciduous broadleaf forests in the eastern United States, Biogeosciences, 16, 467–484, https://doi.org/10.5194/bg-16-467-

838 2019, 2019.

839

840 Xiu, A., and Pleim, J. E.: Development of a land surface model part I: Application in a mesoscale meteorology model, J. Appl.

841 Meteorol., 40(2), 192–209, https://doi.org/10.1175/1520-0450(2001)040<0192:DOALSM>2.0.CO;2, 2001.

842 Ye, Z., Wang, X., and Zhang, L.: Diagnosifng the Model Bias in Simulating Daily Surface Ozone Variability Using a Machine

843 Learning Method: The Effects of Dry Deposition and Cloud Optical Depth, Environ. Sci. Tech.,

844 https://doi.org/10.1021/acs.est.2c05712, 2022.

845

846 Yi, C.: Momentum transfer within canopies, J. Appl. Meteorol. Climatol., 47(1), 262–275,

847 https://doi.org/10.1175/2007JAMC1667.1, 2008.

848

849 Young, A. M., Friedl, M. A., Seyednasrollah, B., Beamesderfer, E., Carrillo, C. M., Li, X., Moon, M., Arain, M. A., Baldocchi, D.

850 D., Blanken, P. D. and Bohrer, G.: Seasonality in aerodynamic resistance across a range of North American ecosystems, Agric.

851 For. Meteorol., 310, 108613, https://doi.org/10.1016/j.agrformet.2021.108613, 2021.

852 Young, P. J., Naik, V., Fiore, A. M., Gaudel, A., Guo, J., Lin, M. Y., Neu, J. L., Parrish, D. D., Rieder, H. E., Schnell, J. L., Tilmes,

853 S., Wild, O., Zhang, L., Ziemke, J. R., Brandt, J., Delcloo, A., Doherty, R. M., Geels, C., Hegglin, M. I., Hu, L., Im, U., Kumar,

854 R., Luhar, A., Murray, L., Plummer, D., Rodriguez, J., Saiz-Lopez, A., Schultz, M. G., Woodhouse, M. T., and Zeng, G.:

855 Tropospheric Ozone Assessment Report: Assessment of global-scale model performance for global and regional ozone

856 distributions, variability, and trends, Elem. Sci. Anth., 6, 10, https://doi.org/10.1525/elementa.265, 2018.

857 Zahn, A., Weppner, J., Widmann, H., Schlote-Holubek, K., Burger, B., Kühner, T., and Franke, H.: A fast and precise

858 chemiluminescence ozone detector for eddy flux and airborne application, Atmos. Meas. Tech., 5, 363–375,

859 https://doi.org/10.5194/amt-5-363-2012, 2012.

860

861 Zeng, X., Shaikh, M., Dai, Y., Dickinson, R. E. and Myneni, R.: Coupling of the Common Land Model to the NCAR Community

862 Climate Model, J. Clim., 15(14), 1832–1854, DOI:10.1175/1520-0442(2002)015<1832:COTCLM>2.0.CO;2, 2002.

863

864 Zhang, L., Moran, M. D., and Brook, J. R.: A comparison of models to estimate in-canopy photosynthetically active radiation and

865 their influence on canopy stomatal resistance, Atmos. Environ., 35(26), 4463–4470, https://doi.org/10.1016/S1352-

866 2310(01)00225-4, 2001.

867

Moved down [90]: the Model Bias in Simulating Daily Surface Ozone Variability Using a Machine Learning Method: The Effects of Dry Deposition and Cloud Optical Depth, Environ. Sci. Tech., https://doi.org/10.1021/acs.est.2c05712, 2022.¶

Moved down [91]: Xiu, A., and Pleim, J. E.: Development of a land surface model part I: Application in a mesoscale meteorology model, J. Appl. Meteorol., 40

Moved down [92]: Meteorol., 40

¶

Moved (insertion) [91]

Moved (insertion) [92]

Moved (insertion) [90]

Moved (insertion) [67]

Moved down [93]: Zhao, Y., Zhang, L., Zhou, M., Chen, D., Lu, X., Tao, W., Liu, J., Tian, H., Ma, Y., and Fu, T.-M.: Influences of planetary boundary layer mixing parameterization on summertime surface ozone concentration and dry deposition over North China, Atmos. Environ., 218, 116950, https://doi.org/10.1016/j.atmosenv.2019.116950, 2018.

¶

Moved (insertion) [94]

Zhang, L., Brook, J. R., and Vet, R.: A revised parameterization for gaseous dry deposition in air-quality models, Atmos. Chem. Phys, 3(6), 2067–2082, https://doi.org/10.5194/acp-3-2067-2003, 2003.

Zhang, L., Brook, J. R., and Vet, R.: On ozone dry deposition—With emphasis on non-stomatal uptake and wet canopies, Atmos. Environ., 36(30), 4787–4799, https://doi.org/10.1016/S1352-2310(02)00567-8, 2002a.

Zhang, L., Moran, M. D., Makar, P. A., Brook, J.R., and Gong, S.: Modelling gaseous dry deposition in AURAMS: a unified regional air-quality modelling system, Atmos. Environ., 36(3), 537–560, https://doi.org/10.1016/S1352-2310(01)00447-2, 2002b.

Zhao, Y., Zhang, L., Zhou, M., Chen, D., Lu, X., Tao, W., Liu, J., Tian, H., Ma, Y., and Fu, T.-M.: Influences of planetary boundary layer mixing parameterization on summertime surface ozone concentration and dry deposition over North China, Atmos. Environ., 218, 116950, https://doi.org/10.1016/j.atmosenv.2019.116950, 2018.

Page 9: [1] Formatted	Clifton, Olivia E.	7/6/23 4:18:00 PM

English (US)

Page 9: [1] Formatted	Clifton, Olivia E.	7/6/23 4:18:00 PM

English (US)

Page 9: [1] Formatted	Clifton, Olivia E.	7/6/23 4:18:00 PM

English (US)

Page 9: [1] Formatted	Clifton, Olivia E.	7/6/23 4:18:00 PM

English (US)

Page 9: [2] Formatted	Clifton, Olivia E.	7/6/23 4:18:00 PM

English (US)

Page 9: [2] Formatted	Clifton, Olivia E.	7/6/23 4:18:00 PM

English (US)

Page 9: [2] Formatted	Clifton, Olivia E.	7/6/23 4:18:00 PM

English (US)

Page 9: [2] Formatted	Clifton, Olivia E.	7/6/23 4:18:00 PM

English (US)

Page 9: [3] Deleted	Clifton, Olivia E.	7/6/23 4:18:00 PM

Page 9: [3] Deleted	Clifton, Olivia E.	7/6/23 4:18:00 PM

Page 9: [4] Deleted	Clifton, Olivia E.	7/6/23 4:18:00 PM

Page 9: [5] Deleted	Clifton, Olivia E.	7/6/23 4:18:00 PM

Page 9: [6] Formatted	Clifton, Olivia E.	7/6/23 4:18:00 PM

English (US), Pattern: Clear (White)

Page 9: [6] Formatted	Clifton, Olivia E.	7/6/23 4:18:00 PM

English (US), Pattern: Clear (White)

Page 17: [7] Deleted	Clifton, Olivia E.	7/6/23 4:18:00 PM

Page 17: [8] Deleted	Clifton, Olivia E.	7/6/23 4:18:00 PM

Page 18: [9] Deleted	Clifton, Olivia E.	7/6/23 4:18:00 PM

Page 18: [10] Deleted	Clifton, Olivia E.	7/6/23 4:18:00 PM

Page 22: [11] Deleted	Clifton, Olivia E.	7/6/23 4:18:00 PM

Page 23: [12] Deleted	**Clifton, Olivia E.**	**7/6/23 4:18:00 PM**

Page 23: [13] Deleted	**Clifton, Olivia E.**	**7/6/23 4:18:00 PM**
Page 42: [14] Deleted	**Clifton, Olivia E.**	**7/6/23 4:18:00 PM**

Page 42: [14] Deleted	**Clifton, Olivia E.**	**7/6/23 4:18:00 PM**

Page 42: [14] Deleted	**Clifton, Olivia E.**	**7/6/23 4:18:00 PM**

Page 94: [15] Deleted	**Clifton, Olivia E.**	**7/6/23 4:18:00 PM**